Max-Planck-Institut für Meteorologie
Max Planck Institute for Meteorology

Examensarbeit Nr. 93

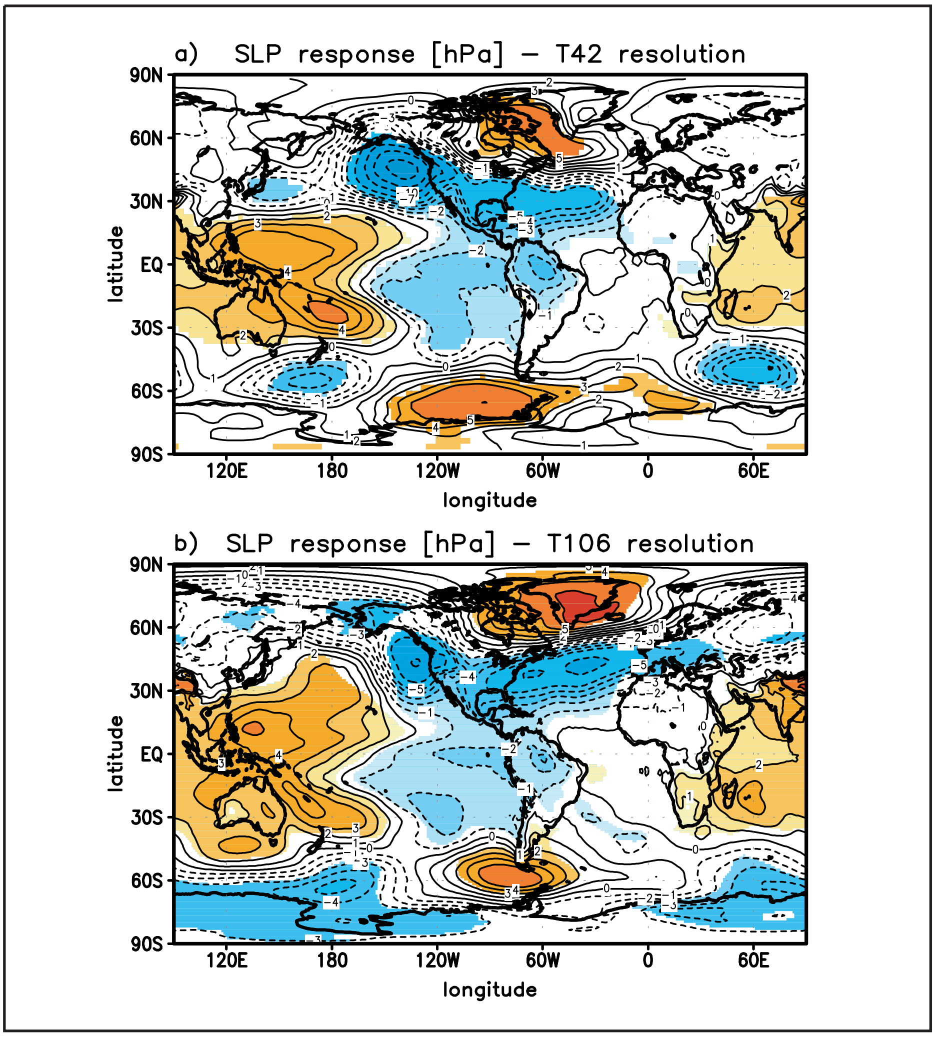

ENSO Teleconnections in High Resolution AGCM Experiments

von

Ute Merkel

Hamburg, Juli 2003

Dissertation zur Erlangung des Doktorgrades

Autorin:

Ute Merkel Max-Planck-Institut für Meteorologie

Max-Planck-Institut für Meteorologie
Bundesstrasse 55
D - 20146 Hamburg
Germany

Tel.: +49-(0)40-4 11 73-0
Fax: +49-(0)40-4 11 73-298
e-mail: <name>@dkrz.de
Web: www.mpimet.mpg.de

ENSO Teleconnections in High Resolution AGCM Experiments

(ENSO-Telekonnektionen in hochauflösenden AGCM-Experimenten)

Dissertation
zur Erlangung des Doktorgrades
der Naturwissenschaften im Fachbereich
Geowissenschaften
der
Universität Hamburg

vorgelegt von
Ute Merkel
aus Hof/Saale

Hamburg
2003

Als Dissertation angenommen vom Fachbereich Geowissenschaften
der Universität Hamburg

auf Grund der Gutachten von Prof. Dr. Mojib Latif
und Prof. Dr. Klaus Fraedrich

Hamburg, den 02.07.2003

Prof. Dr. H. Schleicher
(Dekan des Fachbereichs Geowissenschaften)

Abstract

Seasonal forecasting requires a thorough dynamical understanding of the atmospheric response to boundary forcing such as sea surface temperature anomalies.
This thesis focusses on atmospheric teleconnections related to the El Niño/Southern Oscillation (ENSO) phenomenon and on the dynamics contributing to the signal communication to remote regions. Both of these are investigated by conducting ensemble experiments with an atmospheric general circulation model (ECHAM4).

Some of these experiments have been performed at high horizontal resolution (T106) to examine the role of resolution in simulating the observed atmospheric anomalies during ENSO extremes. A clear resolution dependence of the ENSO response is found over the North Atlantic/European sector.

Furthermore, the atmospheric response is analyzed with respect to its antisymmetry (El Niño and La Niña-type forcing) and is shown to considerably deviate from a simple sign reversal, both in the mean flow and subseasonal fluctuations.

The extratropical transient eddy activity is modified by ENSO through a meridional shift of the midlatitudinal cyclone tracks. In order to gain more insight into the role of transient eddies in determining the atmospheric response to ENSO, the feedback of the transient eddies onto the mean flow is analyzed in terms of the eddy forcing onto the mean streamfunction. Evidence is presented that ENSO related changes in the upper-tropospheric transient eddy vorticity fluxes help to reinforce the mean streamfunction response. However, at lower levels, transient eddy temperature fluxes tend to destroy the mean temperature response and thus to reduce baroclinicity.

Considering anthropogenic climate change, it may be asked whether the atmospheric response to ENSO is changed under future climate conditions. From experiments analogous to those conducted under present climate conditions, it can be concluded that the atmospheric response to the tropical Pacific forcing remains rather robust.

Finally, the influence of ENSO on tropical storms (e.g. hurricanes) is analyzed from a multi-year ECHAM4/T106 integration. In this context, also the large-scale circulation providing the background for tropical storm development is considered. It is shown that the vertical wind shear is clearly affected by ENSO.

Contents

1 Introduction

Climate is what you expect.
Weather is what you get.
(Anonymous)

Since the record warming of the eastern tropical Pacific in 1982/83, then baptized the “El Niño of the century”, has even been surpassed by the 1997/98 El Niño event, the understanding and forecasting of such anomalous events has become one of the most challenging topics in climate research.

In the past, the term “El Niño” was used by Peruvian fishermen to denote the warming of ocean temperatures along the South American west coast around Christmas time, associated with a remarkable disruption of coastal ecosystems, such as fish populations, due to a lack of cold nutrient-rich water. Later on, the basin-wide scale of the oceanic changes was recognized, and a gradual redefinition of “El Niño” took place so that the term now only refers to strong interannual events. The oscillatory nature of El Niño is reflected in the alternation with strong cooling events along the South American west coast, termed La Niña events. Although a unique definition of El Niño and La Niña events does not exist until now, the area average of the sea surface temperature (SST) anomalies within the so-called Niño3 region (150°W-90°W, 5°S-5°N) is commonly used as an index for the SST fluctuations in the tropical Pacific.

For a more thorough understanding of the variability in the tropical Pacific region, the atmospheric dynamics need to be taken into account. In the early 1920’s, Sir Gilbert Walker, while focussing on the Indian summer monsoon, discovered seesaw-like variations of atmospheric sea level pressure across the Pacific basin (Walker, 1923). Nowadays, the so-called Southern Oscillation Index (SOI) is used as a measure for these variations and is based on station data from Darwin (Australia) and Tahiti (French Polynesia). Bjerknes (1969) was one of the first to synthesize the atmospheric and oceanic variations into the interpretation of the El Niño/Southern Oscillation (ENSO) as a coupled ocean-atmosphere phenomenon. Identifying a positive feedback loop, he linked the east-west SST gradient across the tropical Pacific to the atmospheric Walker circulation cell, with its ascending branch above the western Pacific warm pool and descending branch over the eastern tropical Pacific, connected by the easterly trade winds in the lower troposphere. In the

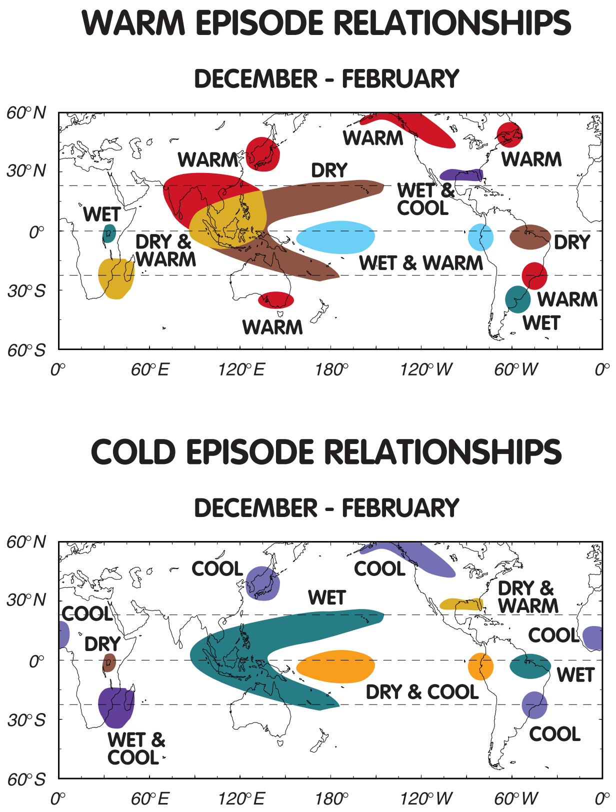

Figure 1.1: *Global observed impacts of El Niño (top) and La Niña (bottom) during the Northern Hemisphere winter (DJF) season (after Halpert and Ropelewski (1992), courtesy N. Noreiks).*

case of an El Niño event, the zonal SST gradient is weakened, accompanied by a slackening of the trade winds and, in the extreme, a reversal of the tropical zonal wind systems.

The timescale of ENSO with a period of 2-7 years is accepted to be partly established by oceanic Rossby and Kelvin wave dynamics. However, the reasons for the irregular occurrence of ENSO extremes and the non-Gaussian distribution of El Niño and La Niña SST anomalies are still subject of ongoing research. Atmospheric noise (stochastic forcing), nonlinear dynamics and long-term changes in the background state of the tropical Pacific are discussed as possible explanations.

The ENSO phenomenon induces major modifications of the Walker and Hadley cells. South America and Indonesia, for example, are among the regions directly affected by such changes. Due to the shift of the major convection zone from the western Pacific warm pool to the east, Indonesia and Northern Australia experience a considerable decrease in precipitation, while precipitation is increased over the western parts of South America.
As noted by Tribbia (1991), however, the oceanic forcing and the related atmospheric response exhibit a clear disparity in scale. Via its atmospheric component, ENSO not only affects regions neighbouring the tropical Pacific, but has also global-scale impacts.

The schematic in Fig. 1.1 illustrates the major changes worldwide accompanying El Niño or La Niña events that have been identified from temperature and precipitation fields for the boreal winter (December to February, DJF). Even parts of Africa and the Asian continent are affected by ENSO extremes. However, ENSO impacts occur not only during DJF. Anomalous subsidence over the Indian subcontinent has been observed in summer of El Niño years, thereby suppressing convection and weakening the summer monsoon circulation (Kumar et al., 1999). Furthermore, observations suggest a considerable decrease (increase) in Atlantic hurricane activity during an El Niño (La Niña) event (Gray, 1984; Landsea, 2000).

The question whether ENSO also affects the North Atlantic/European sector, however, is difficult to assess due to the large internal variability of the atmosphere in midlatitudes. In addition, this region is also influenced by other phenomena such as the North Atlantic Oscillation (NAO). The NAO is a major source of variability on the Northern Hemisphere (Hurrell and van Loon, 1997; Greatbatch, 2000) and might exert a more dominant influence compared to ENSO or could itself be influenced by the tropics. In a composite study of the Northern Hemisphere winter season (DJF), Fraedrich and Müller (1992) investigate the impact of ENSO warm and cold extremes on the atmosphere in the North Atlantic/European sector and find significant changes in the spatial distribution of sea level pressure, air temperature and precipitation. Their results suggest that ENSO warm (cold) events are related to a southward (northward) shift of the North Atlantic storm track, and thus the cyclones with their rainbearing frontal systems follow a modified route. Analyzing 140 years of precipitation data for De Bilt (The Netherlands), van Oldenborgh et al. (2000) find a weak lag relationship between the winter (DJF) Niño3 SST anomaly index and spring (March to May, MAM) precipitation anomalies. This lag correlation ($r \approx 0.3$) shows a tendency for wetter than normal spring seasons over central Europe after an El Niño winter. Such type of studies are based on the assumption of linearity of the atmospheric ENSO response. However, Pozo-Vázquez et al. (2001) note a robust influence on the European sector only during La Niña winters. More recent observational studies have also investigated the ENSO-Europe relationship by focussing on the Mediterranean region (Mariotti et al., 2002) or based on a Red Sea coral record (Rimbu et al., 2003).

The global scale of ENSO impacts is clearly evident from observations, as summarized above. This global-scale relevance of ENSO is responsible for the growing interest, both from the scientific community and the public, in understanding, modelling and predicting ENSO and its impacts.

With regard to the understanding of ENSO itself, much progress has been made during the last two decades from exploiting a whole model hierarchy, ranging from simple, hybrid and intermediate to fully coupled ocean-atmosphere models (Neelin et al., 1998). Together with the improvements in the observing system, ability increased to forecast ENSO-related anomalies in the tropical Pacific region. An extensive review of ENSO predictability is given by Latif et al. (1998).

With regard to understanding ENSO teleconnections globally, much theoretical work has

been published on the atmospheric response to tropical forcing in order to elucidate the dynamics involved in the signal communication to the extratropics. A fundamental work on the tropical atmospheric response to tropical SST forcing has been provided by Gill (1980) with the solution of a simplified atmosphere model forced by an equatorial heat source. His solution successfully reproduced the thermally direct circulation cells (Hadley and Walker circulations) and the pair of upper-tropospheric anticyclones straddling the equator. The Gill-type response is symmetric with respect to the equator when a symmetric forcing is prescribed. According to Gill's results, the response of the tropical atmosphere can be interpreted in terms of eastward propagating Kelvin waves and long planetary westward propagating Rossby waves. Therefore, an east-west asymmetry can be noticed due to the fact that equatorial Kelvin waves are much faster (approx. 3 times) than equatorial Rossby waves.
Although the tropical atmospheric response in Gill's (1980) simple model is in striking correspondence to the observed atmospheric anomalies, this model cannot cover the signal communication to the extratropics. Instead, this signal communication is often explained in terms of Rossby wave dynamics. Rossby's planar approximation has been extended to the sphere by Haurwitz (1940), and Hoskins and Karoly (1981) showed by wave ray tracing the propagation of Rossby wave rays out of a tropical thermal forcing region into midlatitudes. Large parts of the observed extratropical response resemble the Rossby-Haurwitz waves on a sphere. Nevertheless, when simple theory and observations are compared, inconsistencies with pure Rossby wave dynamics remain. Trenberth et al. (1998) present a review of existing theories on ENSO teleconnections.

Since ENSO is now predictable several months ahead, it has become even more challenging to understand the mechanism of a possible signal communication to remote regions, such as the North Atlantic/European sector. In addition to the analysis of observational data, a common approach to address this question is to perform integrations of atmospheric general circulation models (AGCMs), either forced by prescribed SST or coupled to an ocean model (full or mixed layer ocean). Atmosphere-only experiments are commonly performed in the ensemble mode in order to overcome the problem of internal atmospheric variability. Several GCM studies have been performed, either by superimposing idealized SST anomalies (e.g. Ferranti et al., 1994) or by prescribing observed SST anomalies (Bengtsson et al., 1996; Grötzner et al., 2000; Kang et al., 2002). In the study by Ferranti et al. (1994), it has been shown from experiments with the Numerical Weather Prediction model of the European Center for Medium Range Weather Forecast (ECMWF) that tropical Pacific SST anomalies can induce a significant response in the extratropics. However, SST anomalies in the Caribbean region are also found to influence the atmospheric circulation in the European sector.
None of the model experiments mentioned above has been conducted at a higher resolution than T63. I believe, however, that the interaction between the extratropical transient eddies and the mean flow plays a crucial role in establishing the midlatitudinal response to ENSO. The cyclogenesis region off Newfoundland has been assumed, for instance, to act as a link region for the communication of the tropical signal to the North Atlantic/European sector (Fraedrich, 1994).

Hence, I consider it promising to examine the extratropical ENSO response by means of a relatively high resolution AGCM. Within this thesis, the role of resolution is assessed from two types of response experiments. First, the model's ability to reproduce observed anomalies is investigated for the record El Niño event of 1997/98 (case study). This is motivated by the observation of a considerable inter-El-Niño variability (Kumar and Hoerling, 1997). Second, I seek to get some more dynamical insight into the different contributions determining the atmospheric ENSO response. This issue is addressed by several experiments in which the model is forced by typical ("canonical") ENSO SST anomaly patterns, thereby focussing on the synoptic-scale eddies.

In this thesis, the question of the linearity of the ENSO response is also addressed. This is motivated by the observational evidence for nonlinearities and the existing inconsistencies between different AGCM studies with respect to linearity. It should be noted that the degree of nonlinearity might have impacts on the skill of seasonal forecasts (Hoerling et al., 2001b).

From the considerations presented in this chapter, the thesis is organized as follows. The atmospheric circulation model and the experiments performed are described in ch. 2. Major parts of the discussion are based on seasonal ensemble experiments (ch. 3). First, the mean response of the atmosphere to prescribed SST forcing is presented (ch. 3.1). In order to achieve a more thorough understanding of the mean atmospheric response, the impact of ENSO on the stationary and transient eddies is examined in ch. 3.2. Parts of this chapter have already been published in Merkel and Latif (2002). Subsequently, a dynamical picture of the interplay between the mean flow response and the eddy components under ENSO conditions is provided in ch. 3.3. A short excursion into future climate is made by analyzing possible changes of ENSO teleconnections in a simplified greenhouse scenario experiment (ch. 3.4).

On the basis of a multi-year AGCM integration forced by observed SSTs, the response of tropical storms to SST variations in the tropical Pacific is examined as a further aspect of the ENSO impact on transient eddies (ch. 4). A summary and a discussion of the results completes the thesis (ch. 5).

2 The ECHAM4 model and the experiments

Numerous studies on atmosphere-ocean interaction are performed with fully coupled atmosphere-ocean general circulation models. In view of the large computational efforts associated with such experiments, sensitivity experiments with the atmosphere model ECHAM4 forced by prescribed SST are conducted. In this chapter, the ECHAM4 AGCM is described with a special focus on horizontal resolution. Finally, the seasonal ensemble experiments of this thesis are presented. Results of these simulations are discussed in chapter 3.

2.1 The atmospheric general circulation model ECHAM4

The sensitivity studies to be discussed here are all performed with the atmospheric general circulation model ECHAM4. It represents the fourth generation in a model series which has been adapted for climate applications from the spectral weather prediction model of the European Center for Medium Range Weather Forecasts. A comprehensive description of the model characteristics and the changes compared to the previous version (ECHAM3) is given by Roeckner et al. (1996). A brief summary of the main features is given below.

The ECHAM model is based on the primitive equations, using as prognostic variables vorticity, divergence, temperature, the natural logarithm of surface air pressure, specific humidity, and the mixing ratio of total cloud water. With the exception of the water components, the prognostic variables are represented in the *horizontal* by a series of truncated spectral harmonics. Typically, a triangular truncation at wavenumber 42 (T42) is used (see Table 2.1). The role of horizontal resolution will be further discussed in ch. 2.2. In the *vertical*, a discretization into 19 irregularly distributed levels is used. The hybrid sigma-pressure coordinate system used exhibits the highest vertical resolution in the atmospheric boundary layer. The model top reaches the middle stratosphere (10 hPa).
The prognostic equations are integrated according to the semi-implicit method. Linear terms are calculated implicitly using their spectral transform while the nonlinear terms

are treated explicitly on a Gaussian grid and spectrally transformed afterwards. According to the Courant-Friedrich-Levy criterion (James, 1994) on the stability of a numerical scheme, the time step depends on the respective horizontal resolution (Table 2.1).

	mesh size	**grid points**	**grid point distance**	**time step**
T42	2.8° × 2.8°	8192	≈ 300 km	Δt = 24 min
T106	1.1° × 1.1°	51200	≈ 125 km	Δt = 12 min

Table 2.1: *Main characteristics of different horizontal resolutions of ECHAM4.*

While the semi-Lagrangian advection scheme is applied for all variables in the ECMWF model, it is only used for water vapour, cloud water and trace constituents in the ECHAM model.

Interannual fluctuations of sea surface temperature and sea ice are usually suppressed in the uncoupled model runs. The only variations of these quantities are determined by the climatological annual cycle.

Subgrid-scale processes have to be parameterized, and it is the parameterization of several ECHAM3 parts which have undergone changes in the course of the development of ECHAM4, e.g. the radiation code. While ECHAM3 and ECHAM4 reflect approximately the same amount of shortwave radiation to space, the absorption of shortwave radiation is considerably higher in ECHAM4 due to water vapour and clouds.

The model performs well in reproducing both the observed seasonal mean climate and the variability on subseasonal timescales, when compared to ECMWF analyses (see Roeckner et al., 1996). Furthermore, the model performance and quality is further confirmed by the good skill in the representation of stationary waves.

On the other hand, there are several model deficiencies that should be taken into account for the further discussion in this thesis. A large cold bias in the *polar* upper troposphere and lower stratosphere leads to strong upper tropospheric zonal wind errors above the 200 hPa level. In contrast, the *tropical* upper troposphere exhibits too high temperatures compared to observations. This maintains a too strong meridional temperature gradient and results in a tropical westerly wind bias at 200 hPa. Together with too strong trade winds, this leads to an overestimation of the equatorial Walker circulation. With regard to the simulated sea level pressure field, the winter Northern Hemisphere exhibits the largest errors. While the Aleutian and Icelandic lows are weaker than in observations, the Azores high is too strong. A relationship of these deficiencies with the 850 hPa zonal wind error and the lack of precipitation in the Mediterranean can be established.

The model performance in terms of subseasonal variability, however, has generally improved with respect to ECHAM3. Yet, the North Atlantic storm track is too zonally oriented into Central Europe.

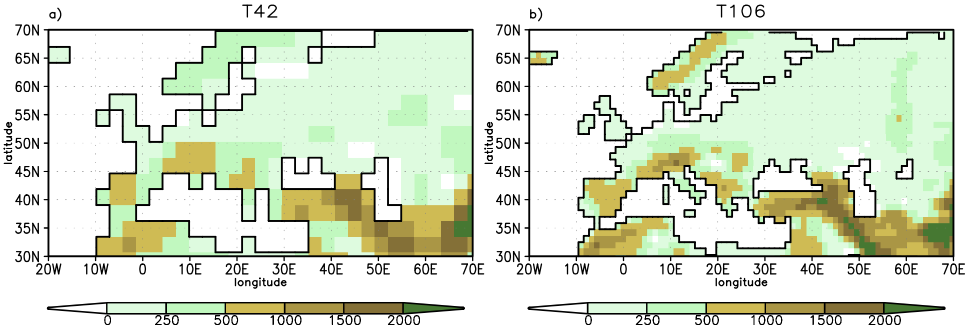

Figure 2.1: *Representation of the European continent orography [m] at different model resolutions: a) T42 and b) T106.*

2.2 Role of horizontal resolution

As a first guess, one would assume that an increase in horizontal resolution reduces the truncation error so that the simulation converges more towards the observations. On the other hand, it has been shown by different authors testing different models (Déqué and Piedelievre, 1995; Branković and Gregory, 2001) that, beside many improvements, increasing the resolution does not necessarily yield more realistic results in every respect. One should also note that it might not be sufficient to only increase the horizontal resolution. A consistent refinement of the vertical resolution may also be required. Furthermore, a step towards higher horizontal resolution also necessitates an adaptation of the model physics, i.e. the parameterizations. In the light of the variety of response studies, the differing results have partly been explained by hypothesizing that the atmospheric response to ocean forcing may look different in experiments performed at higher resolution. This is based on the presumption that, at higher resolution, transient and stationary waves and their interaction with the mean flow would be better captured. Hence, the dynamical components which are considered to decisively contribute to establishing the response could be simulated more realistically.

Since the overall sensitivity of ECHAM4 climate simulations with respect to resolution has been tested extensively by Stendel and Roeckner (1998), only a short overview of their results shall be given below as a basis for the further discussion in this thesis.
At higher horizontal resolution, a more realistic simulation of precipitation and near-surface temperature can be achieved. For example, T106 performs best in the case of the Indian summer monsoon compared to simulations at lower resolution. A systematic improvement of the simulation of present climate with increasing resolution can be found for the zonally asymmetric field (stationary waves). This can be mainly attributed to a more realistic representation of the orography. As an example, the European continent is shown for two different horizontal resolutions in Fig. 2.1.
On the other hand, the zonally symmetric component deteriorates when moving from T42 to T106 resolution. The T106 zonal mean temperature exhibits a low-latitude warm bias

accompanied by a deep-layer warming and a poleward expansion of the warm temperatures of the tropics and subtropics.

Some deficiencies occur at all horizontal resolutions and therefore have to be attributed to the parameterizations. Examples are the overestimation of the intensity of the Azores high and its extent as well as the cold bias in the polar upper troposphere mentioned earlier in section 2.1.

ECHAM4 exhibits the largest resolution dependence in the North Atlantic/European sector. A bias in sea level pressure (SLP) and in geopotential height leads to a zonalisation of the flow over Europe. However, in the North Pacific sector, the flow is simulated reasonably at all horizontal resolutions.

Regarding the intraseasonal variability, both T42 and T106 are comparable with respect to ECMWF Reanalysis (ERA) data (Gibson et al., 1999). Typically, the variability reaches higher amplitudes at T106 resolution than at T42 resolution. Additionally, while T106 is mainly characterized by an overestimation of the amplitude compared to ERA, the opposite is the case for T42.

A common measure for midlatitude storm track activity is the root-mean-square of the bandpass-filtered (2.5-6 days) geopotential height. Fig. 2.2 displays a comparison between the storm track activity at the 500 hPa level during winter (DJF) as simulated by two ECHAM4 control simulations which are both forced by climatological SST and only differ in the horizontal resolution (CTRLWI, CTRLWI42 in Table 2.2). In addition, the storm track activity as represented in the ERA data is shown in Fig. 2.2d. At both resolutions the major midlatitudinal storm tracks are evident over the North Pacific and North Atlantic oceans. It is emphasized by the difference plot (Fig. 2.2c) that resolution matters most in the North Atlantic region. The main storm track activity is more extended towards the north eastern part of the North Atlantic basin in the T106 realization compared to T42. Furthermore, the maximum of variability is shifted to the east in the T106 realization, compared to both the T42 simulation and ERA data.

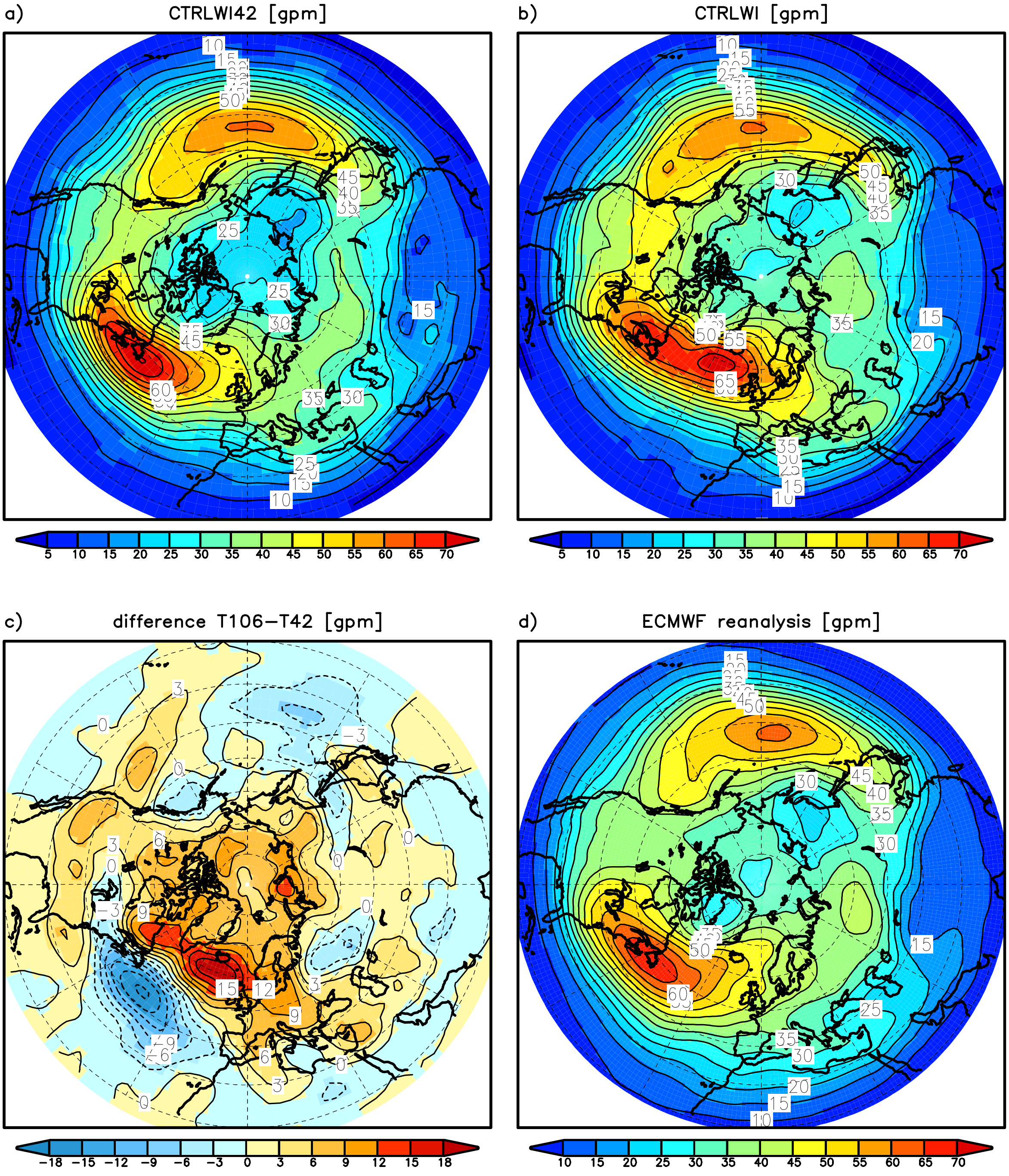

a) CTRLWI42 [gpm]

b) CTRLWI [gpm]

c) difference T106−T42 [gpm]

d) ECMWF reanalysis [gpm]

Figure 2.2: *Seasonal ensemble mean (DJF) storm track activity [gpm] as given by the root-mean-square of the bandpass-filtered (2.5-6 days) geopotential height at the 500 hPa level as simulated by ECHAM4 at a) T42 and b) T106 horizontal resolution. The difference between T106 and T42 is shown in c). d) As b) but for ECMWF reanalysis data.*

2.3 Description of the ensemble experiments

In the light of the discussion of the previous sections, this thesis seeks to further investigate response experiments performed with the same model at different resolutions. Thus, the approach of simply increasing the horizontal resolution is followed without correspondingly tuning the parameterizations. Therefore, changes between the experiments performed at different resolution can truly be related to the resolution. Another approach, which would require much more computational effort, would be to also tune the free parameters in the model physics.
All experiments are performed with the ECHAM4 model described in the previous sections. They are summarized in Table 2.2.

Seasonal ensemble experiments with ECHAM4			
	WINTER		**forced by**
resolution	**T42**	**T106**	
reference exper.	CTRLWI42	CTRLWI	climatol. SST
case studies	CAWI42 (*Grötzner et al., 2000*)	CAWI	observed DJF 1997/98
regression studies	GRWI42	GRWI	regression pattern
	-	TRWI	
	-	NTRWI	

Table 2.2: *Seasonal ensemble experiments with ECHAM4. The experiment names indicate whether the experiment is a control (CTRL), case (CA), global regression (GR), or tropical Pacific regression (TR) experiment and the season (WI=winter). See text for further details.*

All the seasonal experiments listed in Table 2.2 are run in the ensemble mode (5 ensemble members per experiment) in order to overcome the problem of internal atmospheric variability in midlatitudes. As stated by Straus and Shukla (1997), ensemble averaging allows the extraction of the SST-related signal from the internally generated noise in midlatitudes.
Each ensemble member is integrated over 120 days but the first 30 days are discarded due to likely spin-up effects. Only the last 90 days (i.e. December - February, DJF hereafter) are retained for further analysis. The ensemble members just differ in their respective initial conditions which have been determined by starting each member from different restart files of a former multi-year ECHAM4 run. The model output is saved twice-daily.

As *reference experiments*, two winter seasonal control ensemble simulations (CTRLWI42, CTRLWI) are performed at T42 and T106 resolutions with climatological SST prescribed. With respect to these control simulations, several *response experiments* are discussed. The anomalous SST forcing for all the response experiments is determined from the Optimum Interpolation Sea Surface Temperature (OISST) analyses dataset ("Reynolds SST"; Reynolds and Smith, 1994) provided by the Climate Prediction Center (CPC). For this

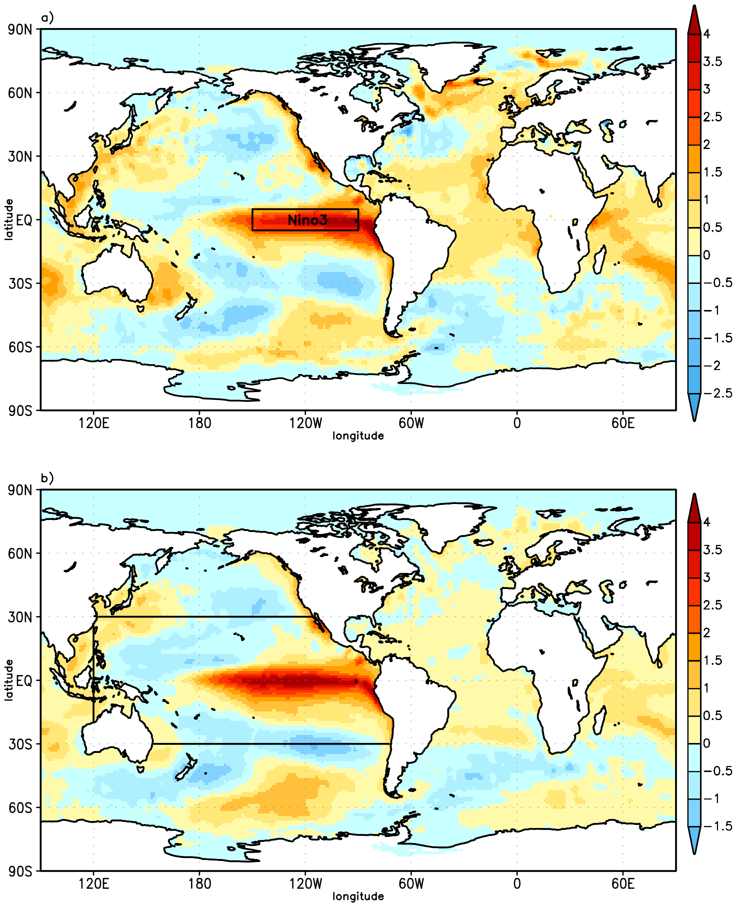

Figure 2.3: *Anomalous SST patterns superimposed onto climatology in the response experiments. a) Observed seasonal mean SST anomalies for DJF 1997/98 [K], b) regression of the global observed DJF seasonal mean SST anomalies onto the Niño3 DJF SST anomaly index, scaled by a factor of 3 [K/K]. The box in the lower panel marks the anomalous forcing area for the tropical regression experiments.*

study, the years 1981-1998 are used since this period contains the two strong El Niño events of 1982/83 and 1997/98. Two types of experiments are conducted.

- <u>case studies</u>:
  The atmospheric response to the strong 1997/98 El Niño event is studied. Therefore, the observed monthly SST anomalies for the winter of 1997/98 (CAWI experiment) are determined from the Reynolds dataset and added onto climatology. For DJF 1997/98, the observed anomalies are depicted in Fig. 2.3a, with positive anomalies of more than 4K in the eastern tropical Pacific. Smaller positive anomalies can be found in the tropical Atlantic and the Indian Ocean. In the central north Pacific and parts of the Southern Hemisphere, negative anomalies prevail. It should be noted that the case study has only been performed at T106 resolution. For an analogous ECHAM4/T42 simulation of the 1997/98 El Niño the reader is referred to Grötzner

et al. (2000) (included into Table 2.2 as CAWI42). The results of these case studies can be directly compared to the observed atmospheric anomalies of 1997/98.

- regression studies:
  For the winter regression studies, the area average of the seasonal mean DJF SST anomaly for the Niño3 region (5°N-5°S, 150°W-90°W) is taken as a characteristic ENSO index. The observed global seasonal mean DJF SST anomalies are then regressed onto the DJF Niño3 SST anomaly index. According to my assumption that only during very strong ENSO events a signal can be communicated to remote regions such as Europe, the resulting regression pattern is multiplied by a factor of 3 and added as an anomalous forcing onto climatology. This scaled pattern is shown in Fig. 2.3b and resembles a "canonical" El Niño SST anomaly, i.e. a typical strong El Niño anomaly, as is evident from the similarity between both panels in Fig. 2.3. The DJF regression experiments are performed at T42 and T106 resolutions (GRWI, GRWI42). Furthermore, two additional T106 experiments are conducted (TRWI, NTRWI) which are similar to GRWI, except for the fact that the enhanced regression pattern is only prescribed in the tropical Pacific (30°S-30°N, indicated by the box in Fig. 2.3b) and climatological SST elsewhere. While the positive regression pattern is imposed in TRWI, the negative of the regression pattern is used in the NTRWI experiment, giving simulations for both ENSO extremes, i.e. El Niño and La Niña.

This set of experiments provides a useful framework to address several aspects. First of all, the role of resolution for the simulated mean response to anomalous oceanic forcing can be evaluated from response experiments with the same model. Furthermore, from the two El Niño-type experiments at T106 resolution (GRWI, TRWI), it is possible to identify the role of anomalous SST forcing in the tropical Pacific. In particular, differences in the simulated El Niño response in remote regions, such as the North Atlantic/European sector, can be determined. In addition, the two experiments with anomalous SST forcing of the same spatial structure but with opposite sign (TRWI, NTRWI) allow to study the symmetry of the atmospheric response.

3 Seasonal ENSO teleconnections

In the present chapter, results from the seasonal ensemble experiments described in the previous chapter are discussed. In a first step, the time mean ENSO response is investigated with respect to the role of resolution, the role of tropical Pacific SST anomalies, and with respect to the linearity of the atmospheric response. Secondly, the purpose is to get more insight into the contributions of stationary and transient eddies to the response of the mean flow, thereby focussing on the feedback of synoptic-scale eddies onto the mean flow. In a final section, ENSO teleconnections under future climate conditions are addressed.

3.1 Seasonal mean ENSO response

First, the time-averaged response is analyzed, which, for the experiments listed in Table 2.2, is identical to the 90-day average (seasonal mean) of each ensemble member. Each diagnostic is then averaged over the ensemble. If not stated otherwise, the ENSO response is determined from the difference between the seasonal ensemble mean of the sensitivity experiment and the respective control experiment. In the remainder of this thesis, this difference is referred to as atmospheric response. The significance of the seasonal mean response is assessed by applying a standard two-tailed Student's t-test.

3.1.1 Seasonal mean ENSO response at different resolutions

3.1.1.1 Canonical ENSO response

The resolution dependence of the seasonal ensemble mean response to ENSO-related SST forcing is analyzed from the global regression winter experiments, GRWI42 and GRWI, and their respective control integrations, CTRLWI42 and CTRLWI (see Table 2.2). These regression experiments are designed to assess the response with respect to a typical or, following Rasmusson and Carpenter's (1982) terminology, a so-called "canonical" El Niño

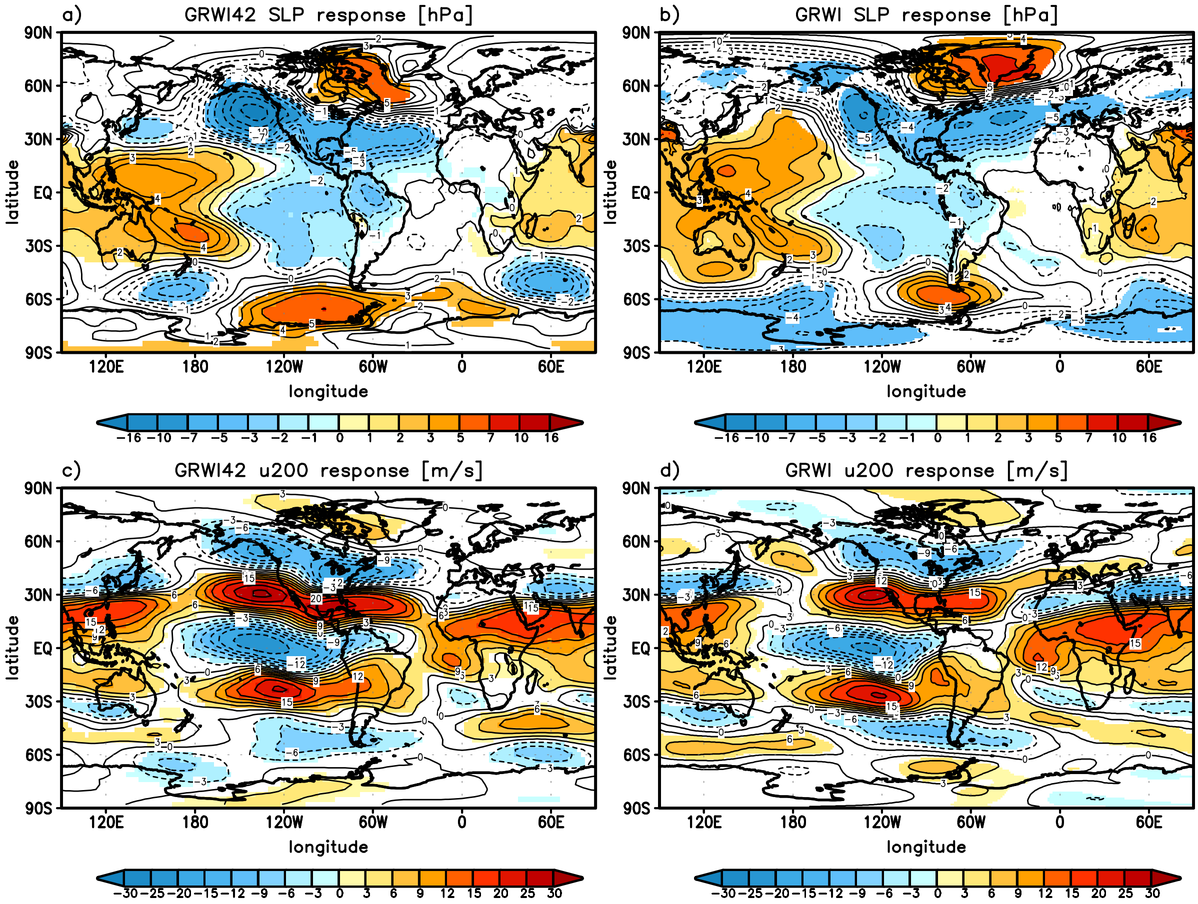

Figure 3.1: *Seasonal ensemble mean response in the DJF global regression experiments at T42 (left panels) and T106 (right panels) resolution for SLP [hPa] (a,b) and the 200 hPa zonal wind [m/s] (c,d). Color denotes significance at the 95% level according to a t-test. The colorbar indicates the irregular contour interval.*

SST forcing. The response of sea level pressure (SLP) is shown in the upper panels of Fig. 3.1. At both resolutions, the Southern Oscillation signature dominates, with SLP anomalies of opposite sign over the western and eastern tropical Pacific. In the Pacific sector, the only major discrepancy between both resolutions is simulated over the north western Pacific with a dipole-like (monopolar) SLP anomaly near Japan in the T42 (T106) version. Significant negative anomalies are present over the north eastern Pacific and over parts of North America. A considerable weakening of the meridional pressure gradient is simulated over the North Atlantic sector, implying a change in the North Atlantic Oscillation (NAO). However, only in the T106 experiment, the two centers of action over the North Atlantic extend eastward into Europe, and a statistically significant response over most parts of central Europe is simulated only at T106 resolution (Fig. 3.1b). The extension of a significant response into Europe at T106 is also present in upper-tropospheric quantities such as the 200 hPa zonal wind field (Fig. 3.1 c,d). Again, the resolution dependence of the response is less marked over the north Pacific sector. At both reso-

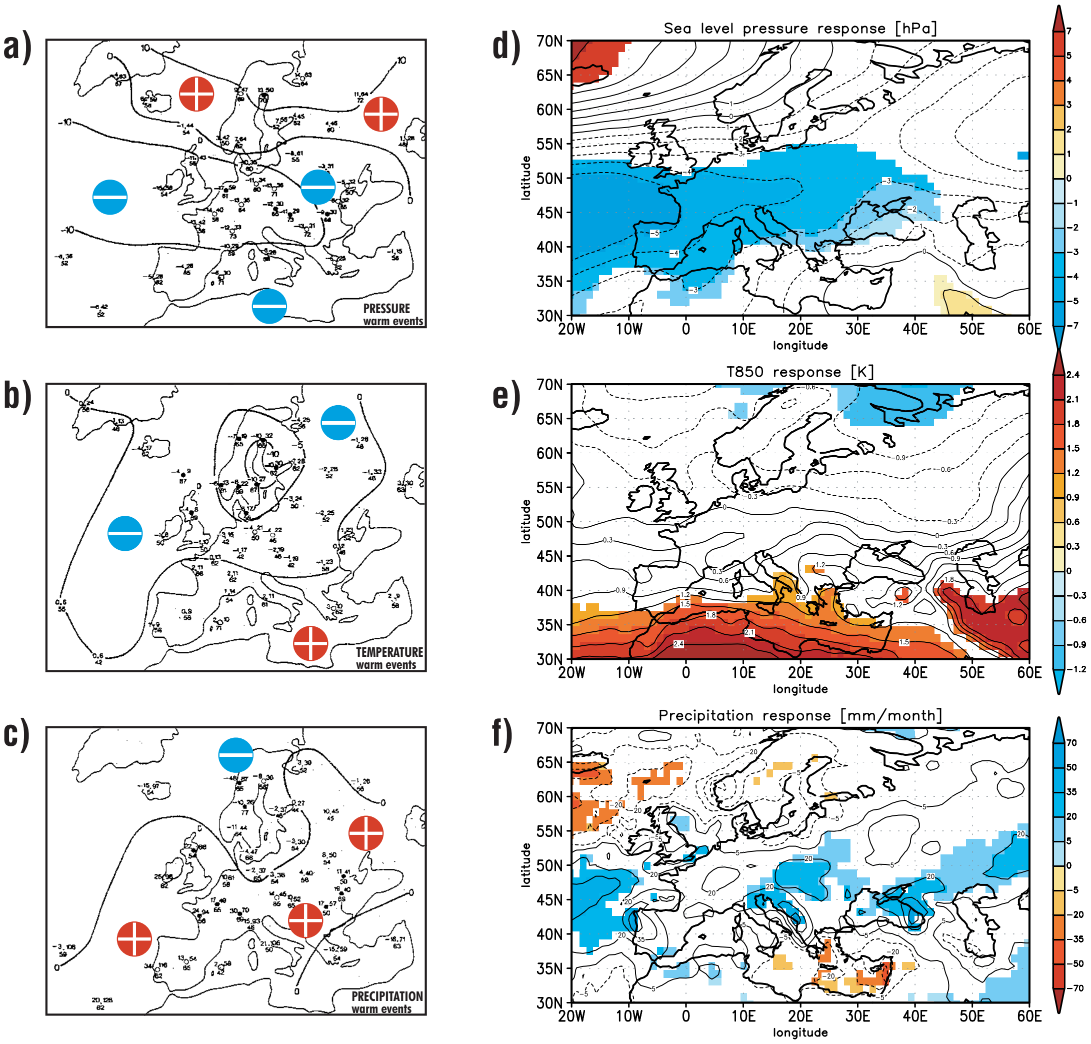

Figure 3.2: *Right panels: Seasonal (DJF) ensemble mean response in GRWI for SLP [hPa] (top), air temperature at 850 hPa [K] (middle), precipitation [mm/month] (bottom). Color indicates significance at the 95% level according to a t-test. For comparison, the results of the El Niño composite study by Fraedrich and Müller (1992) are redrawn on the left (units: [0.1 hPa], [0.1 K], [mm/month], respectively; contour intervals: 1 hPa, 0.5 K, zero line only, respectively).*

lutions, a weakening of the upper-tropospheric westerlies in the tropical eastern Pacific is simulated, with a meridional wavelike structure straddling the equator. According to geostrophic considerations, these wind anomalies in extratropical latitudes correspond to the largest gradients in the geopotential height response (not shown).

As described in the introduction, there have been several attempts to identify an ENSO-related signal not only in the North Atlantic region, but also over Europe. The anomalies of selected atmospheric variables over Europe as simulated by GRWI are shown in Fig. 3.2. Comparing the response to the observational DJF El Niño composites of Fraedrich and Müller (1992) reveals a qualitatively similar and partly significant anomaly structure in the T106 simulation (Fig. 3.2 d-f). The overall meridional dipole-like anomaly structure found by Fraedrich and Müller (1992) is well captured by GRWI. The T42 results (not shown), however, bear no resemblance to the Fraedrich and Müller (1992) El Niño composites over Europe. It has been mentioned in the previous chapter discussing the control simulations that the resolution dependence is less marked in the Pacific/North American (PNA) region and most pronounced in the North Atlantic/European sector. This is also seen in the response patterns which also exhibit a distinct resolution dependence in the North Atlantic/European sector. A quantitative correspondence of the anomalies displayed in Fig. 3.2 cannot be expected due to the different strength of the forcing (the El Niño SST composite for the Fraedrich and Müller (1992) years is clearly weaker than the SST forcing for the model).

At both resolutions, a baroclinic response is simulated over the eastern and western Pacific due to the anomalous lower boundary forcing. The sign of the geopotential height anomalies at the 500 hPa level (z500) and 200 hPa level (z200, not shown) is reversed compared to the sea level pressure anomalies. At both resolutions, an equivalent-barotropic wavelike structure into both hemispheres prevails at all levels (see Fig. 3.3 for T106, left panels). The major discrepancies between the response patterns of GRWI42 and GRWI can be found in the same "critical" regions at all levels: the north-west Pacific around Japan and the European area.

Over Europe, the atmosphere responds with a non-barotropic structure. At higher levels, the zero line in the geopotential height response is located at a more northerly position compared to sea level, and a sign reversal of the anomalies can be found at upper-tropospheric levels (not shown). However, these structures are only partially significant.

3.1.1.2 The El Niño of 1997/98

So far, the atmospheric response has been discussed only with respect to a canonical El Niño SST forcing. Likewise, the seasonal anomalies may only be interpreted as a "canonical" response to El Niño. Several studies, however, have demonstrated the extent to which single El Niño (or La Niña) events may differ from each other and so may the response (Hamilton, 1988; Kumar and Hoerling, 1997). Additionally, it has been pointed out by Grötzner et al. (2000) that higher horizontal resolution than normally used (e.g. Kang et al., 2002) might be necessary for a better simulation of the ENSO response in certain domains. In order to test the T106 model's performance for a particular ENSO event, a case study for the record 1997/98 El Niño is performed (CAWI in Table 2.2) by forcing the model with the observed SST anomalies of DJF 1997/98. This allows a direct comparison to observations or to reanalysis data.

To a large extent, the CAWI ensemble mean response (e.g. SLP, or z500) exhibits a striking similarity to the large-scale GRWI response and is therefore not shown. This similarity could be interpreted as the 1997/98 event fitting into the canonical picture provided by GRWI. On the other hand, this similarity is not so surprising since the SST

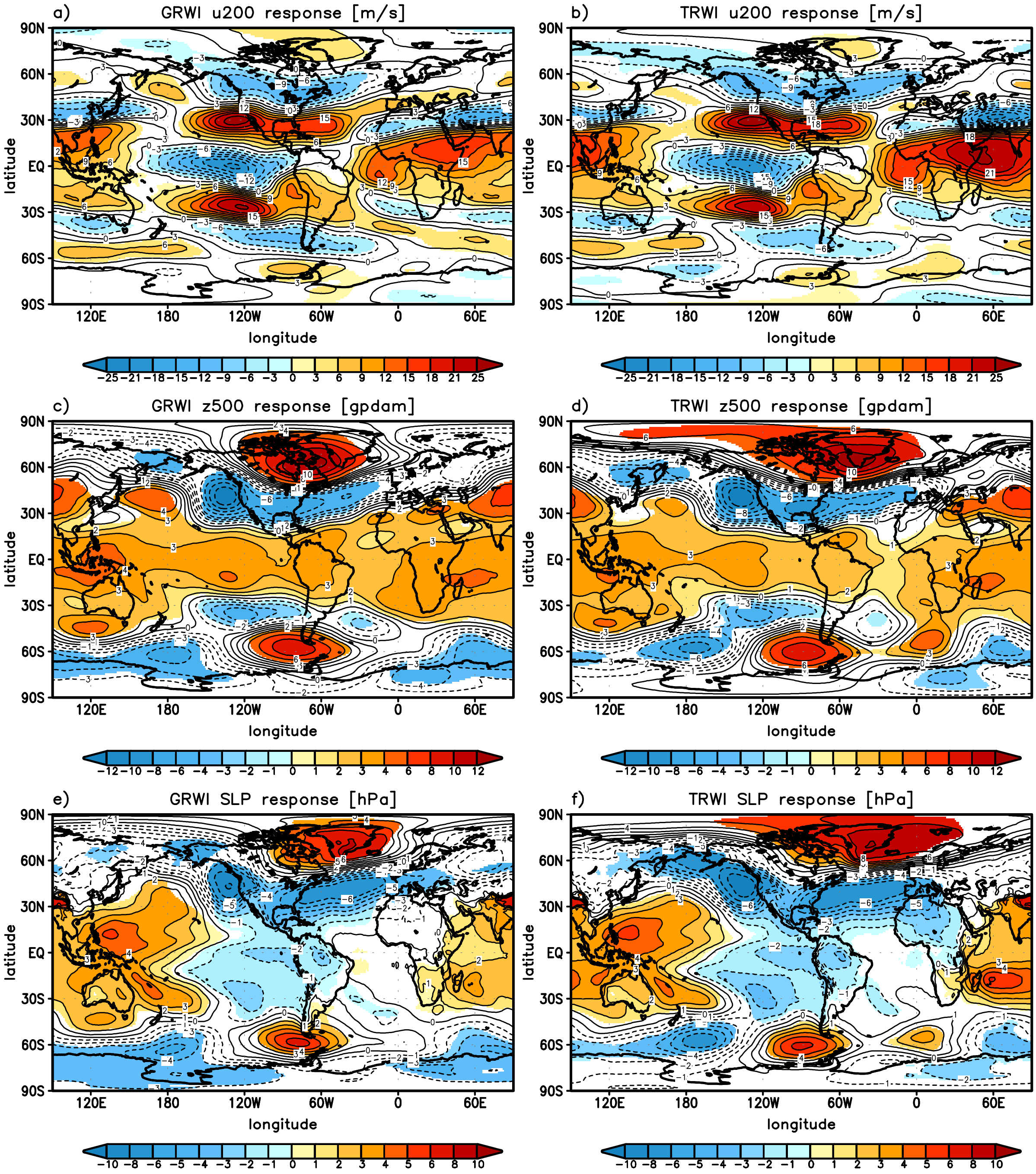

Figure 3.3: *Seasonal (DJF) ensemble mean response in GRWI (left panels) and TRWI (right panels) for the 200 hPa zonal wind [m/s] (top), z500 [gpdam] (middle) and SLP [hPa] (bottom). Color denotes significance at the 95% level according to a t-test. The colorbar indicates the irregular contour interval.*

regression forcing of the GRWI experiment closely resembles the observed 1997/98 DJF SST anomalies prescribed in CAWI (Fig. 2.3). Therefore, instead of further comparing GRWI and CAWI, the correspondence of the simulated CAWI anomalies with observational data is analyzed. Furthermore, the T106 case study (CAWI) is compared to the T42 case study (CAWI42, Table 2.2) by Grötzner et al. (2000).
The overall performance of the T106 model is investigated by comparing the model results (SLP and 850 hPa temperature) simulated by CAWI to the anomalies for winter 1997/98 as determined from the reanalysis data produced by the National Center for Environmental Prediction (NCEP) (Kalnay et al., 1996). Here, the reanalysis data are referred to as observations although they themselves result from a modelling project and therefore may, at times and in regions, disagree with observations. For an evaluation of precipitation, the response simulated by CAWI and CAWI42 is compared to the CMAP precipitation dataset (see Xie and Arkin (1997) for details on the Climate Prediction Center Merged Analysis of Precipitation). However, the comparison of high resolution model output to a precipitation dataset of adequate resolution is difficult, since available high resolution precipitation datasets have often been interpolated from lower resolution observations (Hagemann, 2002).

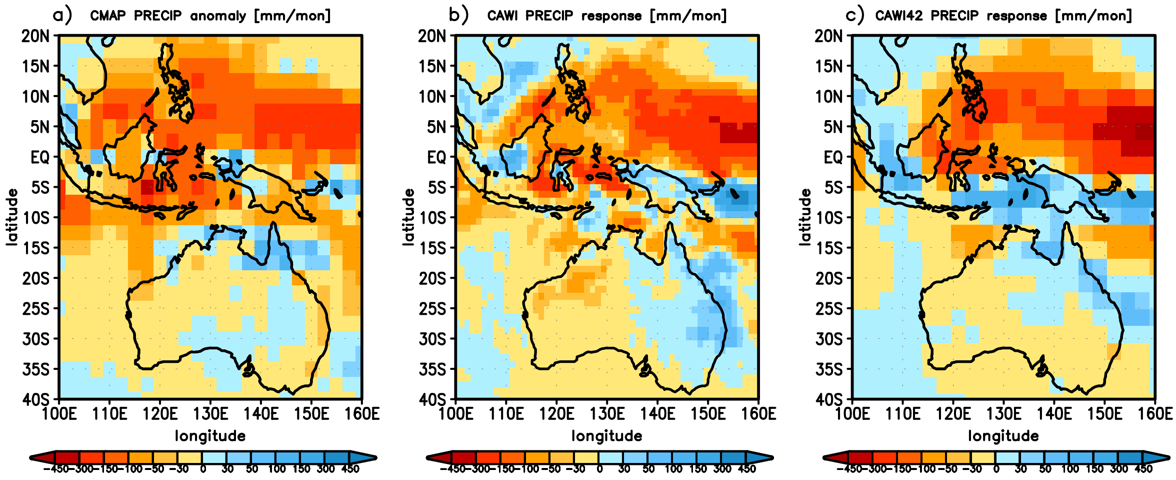

Figure 3.4: *Seasonal mean precipitation anomalies [mm/month] over the Maritime continent for DJF 1997/98 taken from the CMAP dataset (a), and the seasonal (DJF) ensemble mean response simulated by the b) CAWI, and c) CAWI42 ensemble. The colorbar indicates the irregular contour interval.*

The comparison between model results and observations is presented for different regions. The precipitation response in the Indonesian region is shown in Fig. 3.4. The figure clearly illustrates that in such a region of rather complex land-sea distribution, high horizontal resolution is essential for a correct representation of the land-sea distribution and thus for a more realistic simulation of precipitation. A more detailed structure in the simulated response can be noticed (Fig. 3.4 b,c) over the Indonesian islands at higher resolution. The strong decrease in precipitation south of Borneo, for instance, evident in CMAP is better captured by the T106 experiment. Discrepancies with the observed anomalies can also be detected. However, some improvement is found in the New Guinea region in the T106 simulation with less strong positive anomalies than in the T42 simulation. This underlines the difficulty of correctly simulating precipitation. This result is further confirmed by the model intercomparison study of the 1997/98 El Niño by Kang et al. (2002). They conclude that large inter-model differences occur especially over the Indonesian region.

In the previous section, a significant El Niño response has been simulated over the European continent in the T106 global regression experiment (GRWI). It is now analyzed whether this result also holds in the 1997/98 El Niño case (CAWI, CAWI42). As can be seen from Fig. 3.5, the quality of the correspondence between the T106 results and NCEP depends strongly on the considered quantity. Whereas no significant SLP response is simulated in the CAWI ensemble over the European continent, the significant response of the air temperature at 850 hPa (T850) is rather close to the observations. The large positive T850 anomalies seen over Europe and the North Atlantic in the NCEP data are better represented in the T106 experiment than in the T42 experiment. However, the strength of the large positive anomaly is not well captured by either simulation. Regarding precipitation, the correspondence with the CMAP anomalies over Europe is clearly worse. However, a good performance of the model can be found over parts of western Europe, where the response is even found to be significant.

In order to quantify the correspondence between simulated and observed anomalies, pattern correlations are calculated between the "observed" NCEP DJF 1997/98 anomaly (rel. to 1981-98) and the CAWI ensemble mean response for sea level pressure and T850. These correlations are listed in Table 3.1 for selected regions. The precipitation response is assessed using CMAP. In order to illustrate the sensitivity to the NCEP reference period, the pattern correlations of the simulated 1997/98 SLP and T850 anomalies with

		SLP	**T850**	**PRECIP**
Global	all	0.63 (0.63)	0.55 (0.50)	0.72
Tropics	30°N-30°S	0.80 (0.75)	0.55 (0.47)	0.73
extratrop. N.-Hemi.	30°N-70°N	0.64 (0.58)	0.50 (0.44)	0.59
extratrop. S.-Hemi.	30°S-70°S	0.48 (0.52)	0.49 (0.46)	0.26
PNA	180°W-60°W 30°N-70°N	0.81 (0.78)	0.51 (0.44)	0.70
South America	100°W-30°W 60°S-20°N	0.65 (0.68)	0.69 (0.67)	0.73
Europe	30°W-70°E 30°N-70°N	0.57 (0.31)	0.75 (0.67)	0.36

Table 3.1: *Pattern correlations between CAWI anomalies and NCEP reanalysis anomalies for DJF 1997/98 and different regions. NCEP anomalies are calculated with respect to the 1981-98 base period. Numbers in brackets refer to the base period 1958-98. CMAP anomalies are only available for the 1979-99 period. For pattern correlations between the CAWI42 response and observations see Grötzner et al. (2000).*

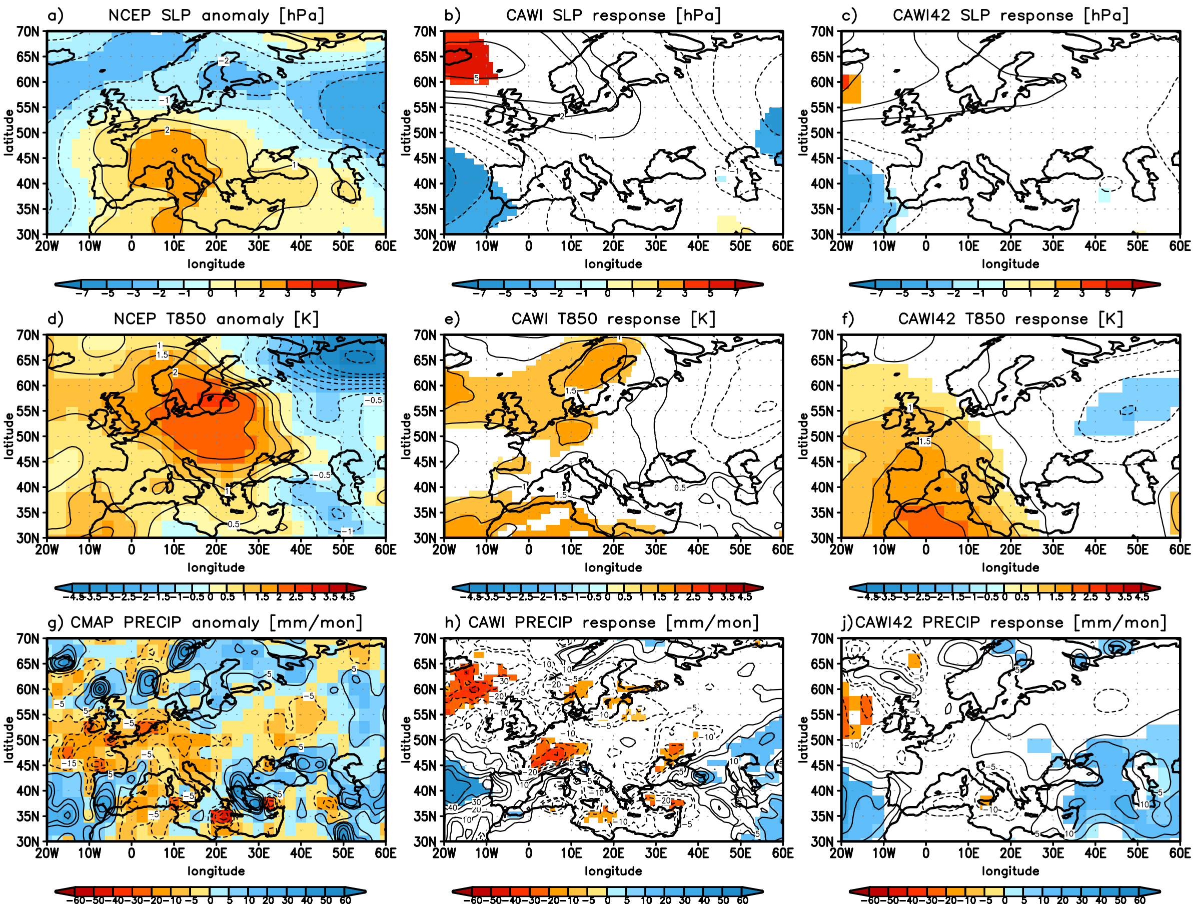

Figure 3.5: *Seasonal mean anomalies over Europe for DJF 1997/98 for SLP [hPa] (a-c), T850 [K] (d-f), and precipitation [mm/month] (g-j) from observations (left), CAWI (middle), CAWI42 (right). Observational data have been taken from the NCEP reanalysis (SLP, T850) and the CMAP project (precip.). Color in the CAWI and CAWI42 plots denotes significance at the 95% level according to a t-test. The colorbars denote the irregular contour intervals.*

the observed anomalies relative to the period 1958-98 are given in brackets. It becomes evident from Table 3.1 that some regions exhibit rather high pattern correlations with the observed anomalies, like the tropics or the PNA region. In other regions, however, the correspondence is less pronounced, as can be seen, for instance, from the low correlation for precipitation over Europe.

Yet, when assessing the simulation in terms of pattern correlations, it should be noted that the observations represent only one realization, while the ensemble technique averages over several realizations and has a smoothing effect. Some information about the ensemble spread, however, is contained in the significance of the simulated response. Thus, in addition to the ensemble mean response, the response of each CAWI ensemble member is evaluated. Table 3.2 illustrates that in the tropics, all ensemble members exhibit strong similarities to the observed patterns both in SLP and precipitation. Over Europe, however, a large spread of the pattern correlations is found within the ensemble. The

		SLP					**PRECIP**				
		m1	*m2*	*m3*	*m4*	*m5*	*m1*	*m2*	*m3*	*m4*	*m5*
Tropics	30°N-30°S	0.78	0.72	0.82	0.67	0.66	0.68	0.71	0.69	0.67	0.69
Europe	30°W-70°E 30°N-70°N	0.15	0.64	0.63	0.20	-0.18	0.38	0.35	0.27	0.30	0.28

Table 3.2: *Pattern correlations between each CAWI ensemble member response* m_i *(i=1,...,5) and NCEP reanalysis SLP anomalies and CMAP precipitation anomalies for DJF 1997/98. NCEP anomalies are calculated with respect to the 1958-98 base period. CMAP anomalies as in Table 3.1.*

numbers given in Table 3.2 suggest that at least two ensemble members (m_2, m_3) produce partly realistic SLP response structures.

From this section it can be concluded that, in some areas, the T106 ensemble response reasonably captures the observed anomalies for DJF 1997/98. Especially in regions where a correct representation of the land-sea distribution or the topography is indispensable, the T106 resolution allows a better simulation, e.g. over parts of South America (not shown) and parts of the Indonesian region. However, one has to note that the T106 resolution might not be enough, since, as has been shown in the case of Indonesia, differences still exist between the simulated response and the CMAP analysis. Furthermore, one has to take into account that a direct comparison between model and observations is hard to evaluate, since the observational (single) realization contains both the anomalous forcing from the ocean and atmospheric noise, as stated by Grötzner et al. (2000).

3.1.2 Role of tropical versus extratropical SST

In the previous section, one main issue was the ENSO impact on Europe. Since this is a relatively remote region with respect to the tropical Pacific, it is often claimed that the influence from other ocean basins, especially the neighbouring North Atlantic, also needs to be considered. The DJF regression of global SST anomalies onto the Niño3 SST anomaly timeseries exhibits considerable anomalies also outside the tropical Pacific, e.g. in the Indian Ocean (Fig. 2.3b). Therefore, the relative role of the SST anomalies in the tropical Pacific in inducing the global seasonal mean response is addressed. It is beyond the scope of this thesis to systematically repeat the type of experiments performed in earlier studies (Lau and Nath, 1994; Graham et al., 1994) by prescribing the temporal SST evolution either globally or restricted to certain ocean domains. Instead, only a comparison of the two El Niño ensemble experiments GRWI and TRWI (see Table 2.2) is discussed. The TRWI (= tropical regression winter) experiment differs from GRWI only in that the tropical Pacific part of the global regression pattern shown in Fig. 2.3b is superimposed onto climatology, with climatological SST prescribed elsewhere. Again, the changes in GRWI and TRWI are computed with respect to the CTRLWI control ensemble.

The overall similarity of GRWI and TRWI in the seasonal (DJF) ensemble mean response patterns of SLP, z500, and u200 is striking (Fig. 3.3). Although the map projection chosen in Fig. 3.3 overemphasizes the high latitudes and polar regions, the significant northern lobes in the North Atlantic SLP and z500 responses clearly extend even further eastward in the TRWI experiment compared to their GRWI counterparts. The pattern correlations between the respective GRWI and TRWI responses are provided for selected variables and regions in Table 3.3.

		SLP	**T850**	**PRECIP**	**z500**	**u200**
Global	all	0.85	0.86	0.95	0.84	0.94
Tropics	30°N-30°S	0.97	0.94	0.95	0.96	0.96
extratrop. N.-Hemi.	30°N-70°N	0.84	0.79	0.88	0.87	0.94
extratrop. S.-Hemi.	30°S-70°S	0.86	0.91	0.80	0.89	0.88
PNA	180°W-60°W 30°N-70°N	0.91	0.90	0.91	0.96	0.98
South America	100°W-30°W 60°S-20°N	0.98	0.97	0.96	0.98	0.97
Europe	30°W-70°E 30°N-70°N	0.75	0.84	0.81	0.66	0.95

Table 3.3: *Pattern correlations between the seasonal (DJF) ensemble mean GRWI and TRWI responses for selected regions and quantities.*

High correlations are found both for upper-tropospheric fields (e.g. u200) and at lower levels (e.g. precipitation). This result emphasizes the importance of the tropical Pacific. This is not surprising for the tropics. However, the overall similarity, even in remote regions such as Europe, shows the negligible role of the extratropical SST anomalies in my experiments. Obviously, this contradicts other studies that suggest an important influence of extratropical SST on the atmosphere, both in the North Pacific (Lau and Nath, 1990) and the North Atlantic (Palmer and Sun, 1985). On the other hand, it supports the findings by Lau and Nath (1994) and Graham et al. (1994) who attribute midlatitudinal variability in the atmosphere to remote forcing from the tropics. The experimental setup of this thesis and the considered timescales are different from the study by Hoerling et al. (2001a). However, the results of my ensemble simulations are consistent with those of Hoerling et al. (2001a) concerning the North Atlantic/European sector. Hoerling et al. (2001a) attribute their successful simulation of the recent observed NAO trend mainly to the influence from the tropics. The contradicting results from the different studies referenced above may be reconciled taking into account the extraordinary strength of the anomalous GRWI and TRWI forcing in the tropical Pacific. It is my conjecture that the SST anomalies in the other ocean basins play a subordinate role compared to those in the tropical Pacific basin.

Furthermore, the T106 regression experiments confirm the conclusion of the T42 study by

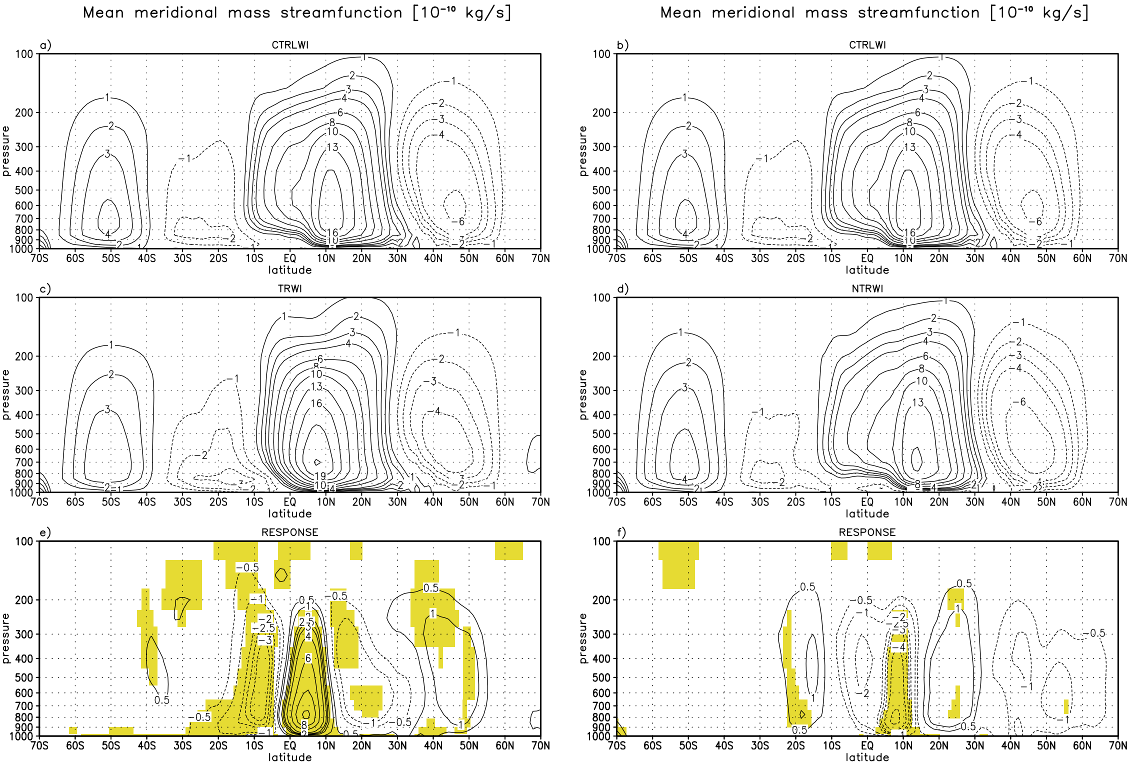

Figure 3.6: *Seasonal (DJF) ensemble mean meridional mass streamfunction [10^{-10} kg/s] in a latitude-height section for (a=b) CTRLWI, c) TRWI, and d) NTRWI. The bottom panels show the response for e) TRWI, and f) NTRWI with respect to CTRLWI. Color denotes significance at the 95% level according to a t-test. Note the irregular contour interval.*

Grötzner et al. (2000) that almost the entire 1997/98 El Niño response is reproduced by their Pacific-only experiment. Thus, the characteristic dipole response structure (e.g. of SLP) in the North Atlantic region is simulated in both the CAWI42 (Grötzner et al., 2000) and the T106 experiments (CAWI, GRWI, TRWI), but it extends further eastward at T106 resolution.

3.1.3 On the linearity of the mean response

The experiments described in the previous sections were all designed to investigate the atmospheric response to ENSO warm phases (El Niños). Next, the response to ENSO cold phases (La Niñas) is tackled and contrasted to the warm phase response. In the context of comparing the El Niño and La Niña responses, the term “linearity” is often used, but it should be applied with caution. Linearity can be interpreted as the relationship of the response to the *amplitude* of the forcing. On the other hand, linearity also refers to the response with respect to the *sign* of the forcing. Here, the spatial structure of the response is investigated only with respect to the sign of the forcing, i.e. the symmetry of the atmospheric ENSO response. For this purpose, another high resolution ensemble experiment (NTRWI = negative TRWI) has been performed in complete analogy to the TRWI experiment (Table 2.2), but with opposite sign of the anomalous SST forcing in the tropical Pacific.

First, the symmetry of the response is tested in the seasonally and zonally averaged meridional circulation. Climatologically, the tropical troposphere exhibits thermally direct circulation systems, such as the meridional Hadley cells which are characterized by (near-) equatorial heating (inducing convection) and subtropical subsidence. The Hadley cell is clearly seen in the mean meridional mass streamfunction χ (Fig. 3.6), which can be calculated from

$$\{v\} = g \, \frac{\partial \chi}{2\pi R \cos\varphi \, \partial p} \tag{3.1}$$

with $\{v\}$ denoting the zonally averaged meridional wind, g the acceleration due to gravity, R the Earth's radius, φ the geographical latitude and p the air pressure.
A comparison between the zonally averaged meridional circulation for the DJF control ensemble (CTRLWI) and the El Niño and La Niña ensembles (TRWI, NTRWI) is shown in Fig. 3.6. In the Northern Hemisphere, enhanced tropical heating during El Niño events leads to a significant intensification and a narrowing of the thermally direct cell with enhanced convection at the equator and the most intense part of the descending branch shifted equatorward (Fig. 3.6e). Consequently, the descending branch of the Hadley cell exhibits a weakened subsidence between 15°N and 30°N. The response pattern during the ENSO cold phase (Fig. 3.6f) reveals a roughly antisymmetric structure compared to the ENSO warm phase response, although only the equatorial weakening of the northern Hadley circulation is significant. It should be noted that the innertropical circulation changes found in NTRWI (Fig. 3.6f) do not reach the magnitudes of the changes in its TRWI counterpart.

Additionally, the global geopotential height responses of the 200 hPa level (z200) for the El Niño and La Niña situations (TRWI, NTRWI) are investigated. Over the tropical Pacific, a Gill-type (Gill, 1980) response is apparent in both ENSO phases, with two anticyclones (cyclones) straddling the equator in the El Niño (La Niña) experiment (Fig. 3.7 a,b). In midlatitudes, however, the TRWI z200 response exhibits a rather zonal structure, in contrast to the wavelike response structure seen in the NTRWI experiment. Furthermore, there is an eastward shift of the Aleutian anomaly in the El Niño experiment compared to the La Niña simulation of about 15°. This shift is in close correspondence with the observational results by DeWeaver and Nigam (2002). Further downstream, no structural similarity between the TRWI and NTRWI responses can be detected over the North Atlantic/European sector.
It is worthwhile to further compare the amplitudes of the response in the El Niño and La Niña cases with each other. With the exception of the Aleutian anomaly, both in the tropics and midlatitudes, the cold ENSO phase induces a weaker, but still appreciable, response in the Pacific region. Thus, these results are in some agreement with those of

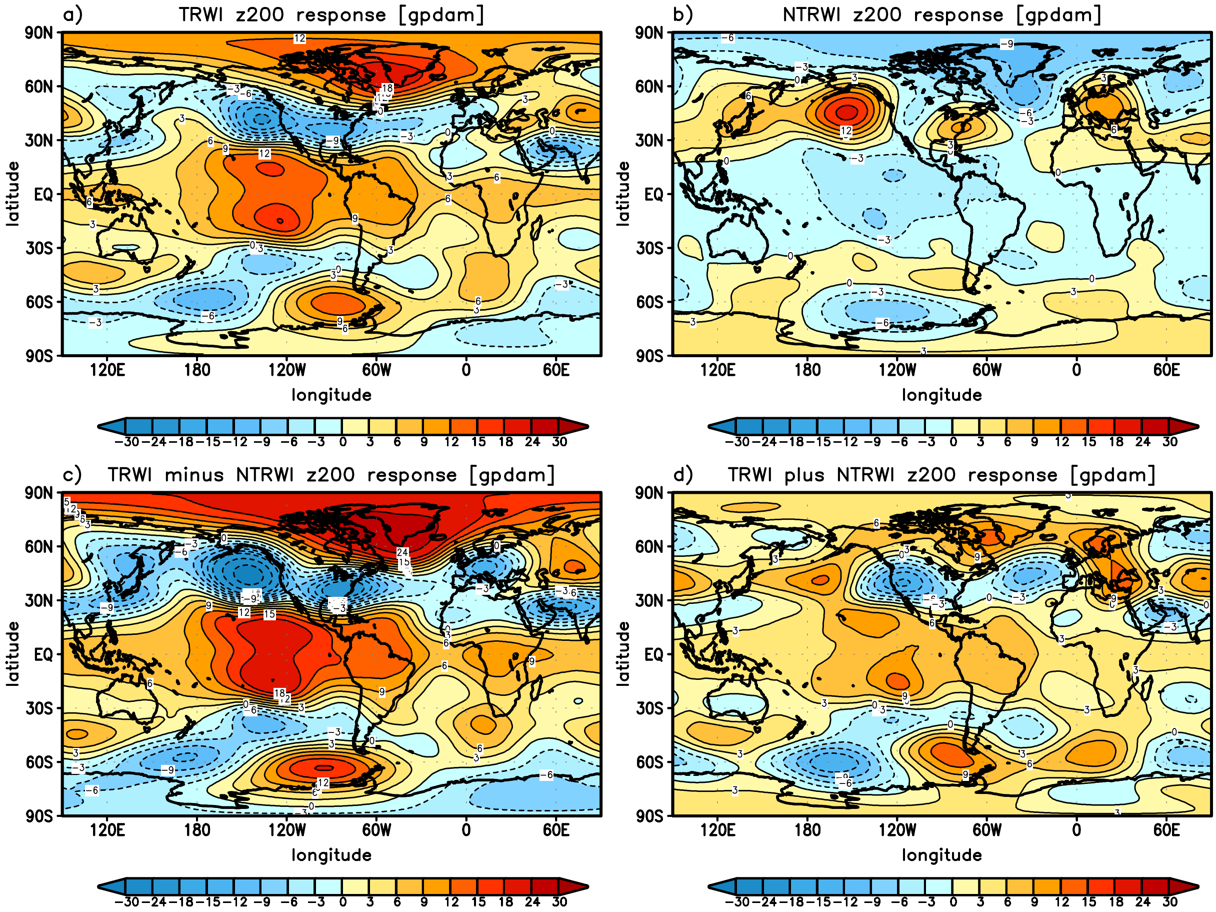

Figure 3.7: *Seasonal (DJF) ensemble mean z200 response [gpdam] in the tropical regression experiments a) TRWI, and b) NTRWI. Furthermore, the difference (c) and the sum (d) of the TRWI and the NTRWI responses are displayed. The significance is not shown. The colorbar indicates the irregular contour interval.*

Hoerling et al. (2001b), who find the cold event response in midlatitudes to be comparable to the warm event counterpart.

In order to quantitatively compare the El Niño and La Niña experiments, both the difference and the sum of the TRWI and the NTRWI z200 responses are also displayed in Fig. 3.7. These panels demonstrate the extent of symmetry in the atmospheric response to the two ENSO extremes. The difference plot (Fig. 3.7c) largely reproduces the El Niño response of Fig. 3.7a. The large non-zero values in the Pacific/American sector can be interpreted as large discrepancies between the responses to the two ENSO extremes. But large differences cannot be solely used as a measure for antisymmetry (equal pattern, opposite sign). In addition, such regions should exhibit near-zero values in the sum plot (Fig. 3.7d). The sum being exactly zero would highlight that the TRWI and the NTRWI responses are exactly antisymmetric. Therefore, it can be concluded from Fig. 3.7 c,d that although c suggests a degree of linearity in the system, d shows that the TRWI and the NTRWI responses do not cancel out and therefore exhibit a clear departure from antisymmetry. This holds especially in midlatitudes (North America, North Atlantic, Europe), but also in the tropical Pacific. The lowest values in the sum plot can be found in the tropics, in agreement with the early results by Gill (1980) on the applicability of linear theory in the tropics. In contrast, large deviations from antisymmetry, i.e. from a simple sign reversal in the response, are found over North America and the North Atlantic/European sector (Fig. 3.7d). Sum and difference are of comparable amplitude over Europe. Here, the La Niña composites by Fraedrich and Müller (1992) are largely reproduced (not shown) which do not exhibit a simple sign reversal compared to the El Niño response.

The experimental setup of this thesis does not allow to study completely the linearity of the response. However, it is worthwhile to consider the results with respect to the findings of Hoerling et al. (2001b). They performed idealized experiments with prescribed positive and negative SST anomalies of the same strength and tested the sensitivity with respect to weak and strong tropical Pacific forcing. In the weak ENSO forcing regime (i.e. below one standard deviation), they find a near-linear dependence of the response. In the strong ENSO forcing regime, however, amplitude nonlinearity occurs, in the sense that stronger warm events force a stronger atmospheric response, while for stronger cold events the atmospheric response saturates. This underlines a larger sensitivity of the atmosphere to strong warm events compared to cold events of the same strength. In the light of these results, the departures from pure antisymmetry found in the TRWI and NTRWI experiments could, at least partly, be due to the fact that the prescribed SST forcing lies well beyond the range of Hoerling et al.'s (2001b) weak ENSO forcing regime. Thus, the substantial departures from antisymmetry shown in Fig. 3.7 support the results of Hoerling et al. (2001b). However, it should be emphasized that the SSTA amplitudes prescribed in the NTRWI experiment have to be considered as rather idealized, since the observed distribution is skewed towards positive SST anomalies. The issue of the symmetry of the response is raised again in the context of the stationary and transient eddy response to be discussed next (ch. 3.2).

3.2 ENSO impact on the eddies

In order to shed more light on the dynamics contributing to the seasonal mean response, the focus of this chapter is on the stationary waves and transient eddy activity and how they are modified under ENSO extreme conditions. Each atmospheric quantity X is split into a mean part and deviations from the mean. The mean can represent either a zonal average $\{X\}$ or a time average $\overline{X}$ of the respective quantity X.

$$X(\lambda,\varphi,t) = \{X\}(\varphi,t) + X^*(\lambda,\varphi,t) \tag{3.2}$$

$$X(\lambda,\varphi,t) = \overline{X}(\lambda,\varphi) + X'(\lambda,\varphi,t) \tag{3.3}$$

with λ, φ, and t denoting longitude, latitude and time. According to this notation, longitudinal fluctuations ("stationary eddies" hereafter) are denoted by asterisks, and temporal fluctuations ("transient eddies" hereafter) by primes.

In the following, dynamical contributions to the seasonal mean ENSO response (as discussed in ch. 3.1) are analyzed, thereby focussing on the canonical ENSO experiments. As in the discussion of the mean response, the eddy response is presented on an ensemble mean basis.

3.2.1 Stationary eddies

The seasonal mean flow exhibits clear zonal asymmetries. In the remainder of this thesis, these asymmetries in the mean flow are synonymously referred to as stationary waves or stationary eddies. The role of stationary eddies is particularly important with respect to the meridional transport of heat and momentum between low and high latitudes.

First, this role and its change under ENSO conditions is analyzed from the zonal mean stationary eddy heat and momentum fluxes, $\{\overline{v}^*\overline{T}^*\}$ and $\{\overline{u}^*\overline{v}^*\}$, respectively.

Climatologically, stationary eddy transports are most important in the Northern Hemispheric upper troposphere. In the case of stationary eddy meridional heat transport, important contributions also come from the lower and middle troposphere, in accordance with the findings by van Loon and Rogers (1981). This is evident from both T42 and T106 control simulations (Fig. 3.8 and 3.9 a,b) with a high degree of similarity between the two resolutions.

The calculation of the ensemble mean response of $\{\overline{v}^*\overline{T}^*\}$ in the global El Niño experiments GRWI (w.r.t. CTRLWI) and GRWI42 (w.r.t. CTRLWI42) (Fig. 3.8 e,f) reveals that the largest amplitudes are reached in the lowest and highest analyzed levels. In the upper troposphere north of 60°N the poleward heat transport is increased at both resolutions, while it is weakened at about 60°N in the lower troposphere. The comparison of the $\{\overline{v}^*\overline{T}^*\}$ response for the global and the tropical Pacific forcing (GRWI, TRWI) reveals a different structure, especially in the lower half of the Northern Hemisphere troposphere.

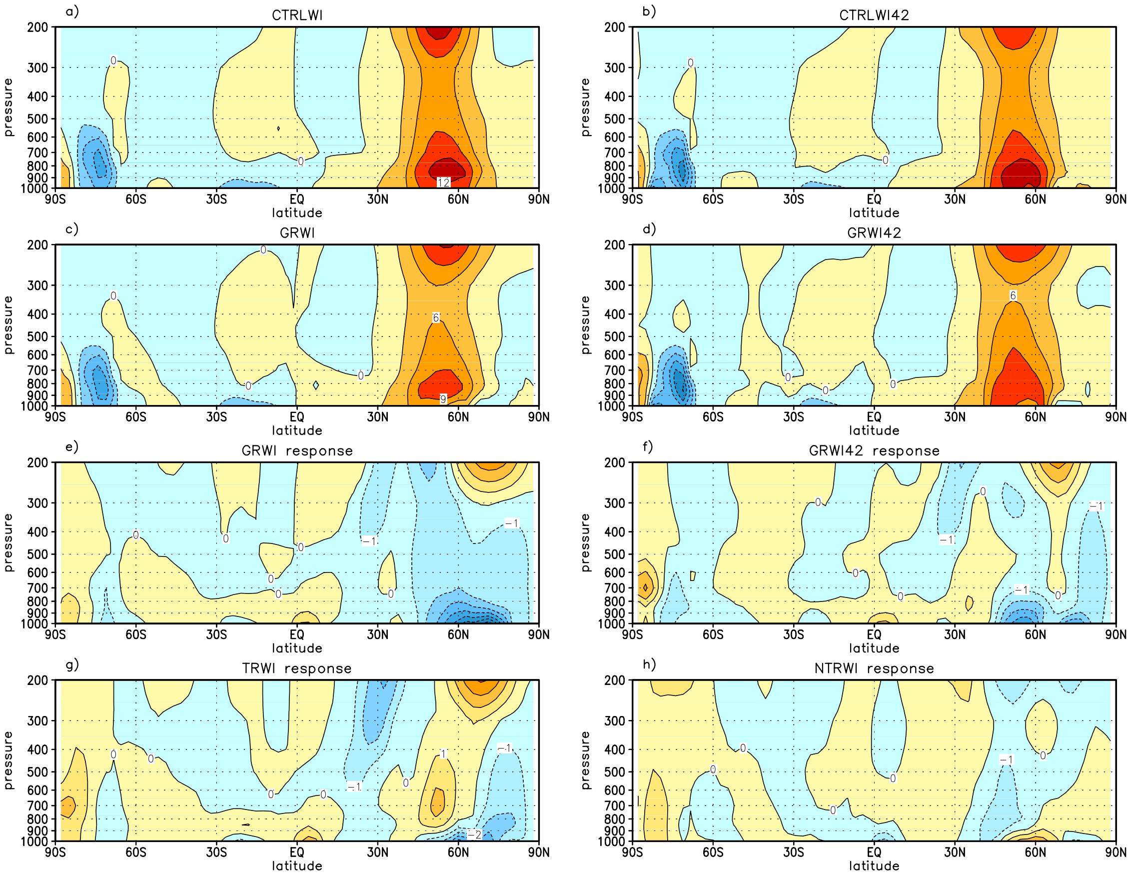

Figure 3.8: *Latitude-height section of the zonally averaged seasonal (DJF) ensemble mean stationary eddy meridional heat flux* $\{\overline{v}^*\overline{T}^*\}$ *in the a) CTRLWI, b) CTRLWI42, c) GRWI, and d) GRWI42 ensemble (contour interval: 3 K·m/s). The ensemble mean response of* $\{\overline{v}^*\overline{T}^*\}$ *is shown for the e) GRWI, f) GRWI42, g) TRWI and h) NTRWI ensemble (contour interval: 1 K·m/s).*

No major changes are simulated in the NTRWI experiment (Fig. 3.8h).
In the $\{\overline{u}^*\overline{v}^*\}$ response in GRWI and GRWI42 (Fig. 3.9 e,f), a southward shift of the upper-tropospheric dipole pattern in midlatitudes is evident. This is emphasized by the strong negative response (in some regions by 50% and more) of $\{\overline{u}^*\overline{v}^*\}$ between 30°N and 60°N. The response at T42 resolution (Fig. 3.9f) is even stronger than its T106 counterpart (Fig. 3.9e). When the canonical El Niño SST anomaly pattern is only prescribed in the tropical Pacific (TRWI experiment), the $\{\overline{u}^*\overline{v}^*\}$ response (Fig. 3.9g) largely resembles the responses simulated by GRWI and GRWI42, but it reaches even higher amplitudes, covers a larger latitudinal region, and extends further downward. When the sign of the forcing is reversed (NTRWI, Fig. 3.9h), the sign of the response is reversed in midlatitudes, and the response is clearly weaker than in the El Niño experiments.

So far, it can be concluded that the zonal mean response of the stationary waves is not much sensitive to changes in horizontal resolution. While the $\{\overline{v}^*\overline{T}^*\}$ response changes

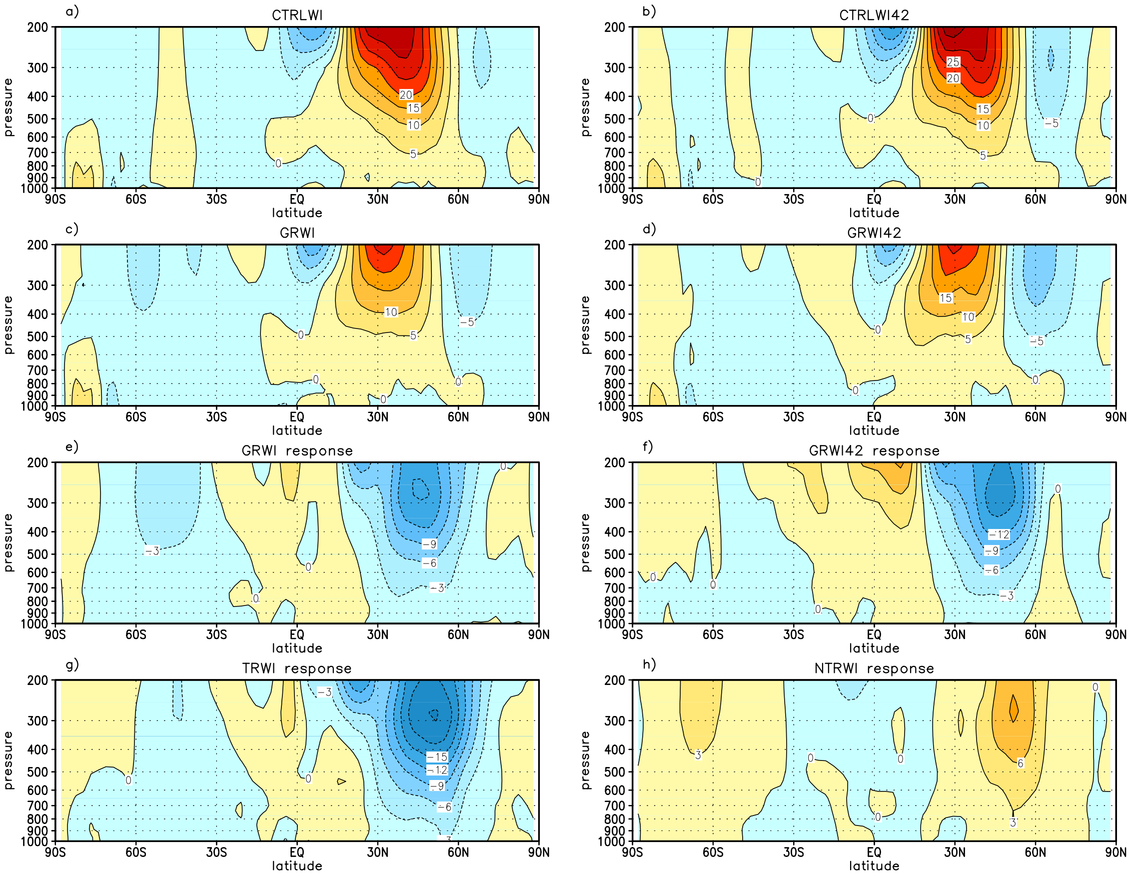

Figure 3.9: *Latitude-height section of the zonally averaged seasonal (DJF) ensemble mean stationary eddy meridional flux of zonal momentum* $\{\overline{u}^*\overline{v}^*\}$ *in the a) CTRLWI, b) CTRLWI42, c) GRWI, and d) GRWI42 ensemble (contour interval:* $5\,m^2/s^2$*). The ensemble mean response of* $\{\overline{u}^*\overline{v}^*\}$ *is shown for the e) GRWI, f) GRWI42, g) TRWI, and h) NTRWI ensemble (contour interval:* $3\,m^2/s^2$*).*

sign in the troposphere, an equivalent-barotropic structure is apparent in the $\{\overline{u}^*\overline{v}^*\}$ response. With regard to the particular role of tropical Pacific SST, the picture is only slightly changed in TRWI vs. GRWI for $\{\overline{u}^*\overline{v}^*\}$, while $\{\overline{v}^*\overline{T}^*\}$ clearly exhibits different response structures in TRWI compared to GRWI.

In the following, hemispheric distributions of the stationary eddies are discussed. Both control ensembles (Fig. 3.10 a,b) exhibit roughly the same structure of the hemispheric stationary eddy heat flux, $\overline{v}^*\overline{T}^*$, and are in reasonable correspondence with early observational results (e.g. van Loon and Williams, 1980). Differences are visible in the simulated $\overline{v}^*\overline{T}^*$ amplitudes. While at T106 resolution, the simulated meridional heat transport is stronger than at T42 resolution over the eastern Asian continent, the reverse holds over the North Atlantic region.
The ensemble mean $\overline{v}^*\overline{T}^*$ response is included in Fig. 3.10. As in the control simulations, the role of resolution becomes now evident in the structure and strength of the response.

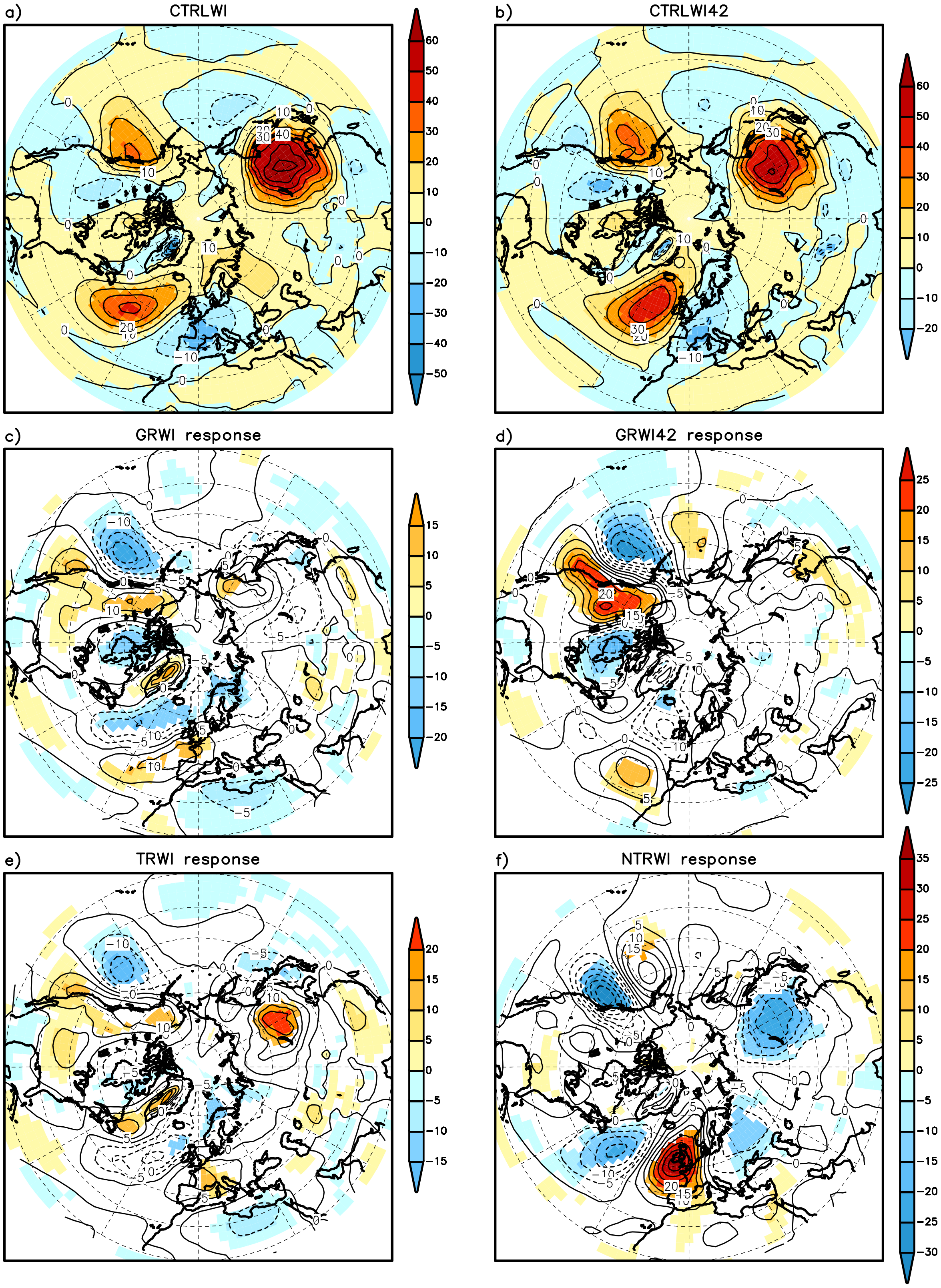

Figure 3.10: *Seasonal (DJF) ensemble mean stationary eddy meridional heat flux, $\overline{v}^*\overline{T}^*$, at 700 hPa [K·m/s] in the a) CTRLWI, and b) CTRLWI42 ensemble. The ensemble mean response of $\overline{v}^*\overline{T}^*$ is shown for the c) GRWI, d) GRWI42, e) TRWI and f) NTRWI ensemble. Color in panels c-f denotes significance at the 95% level according to a t-test.*

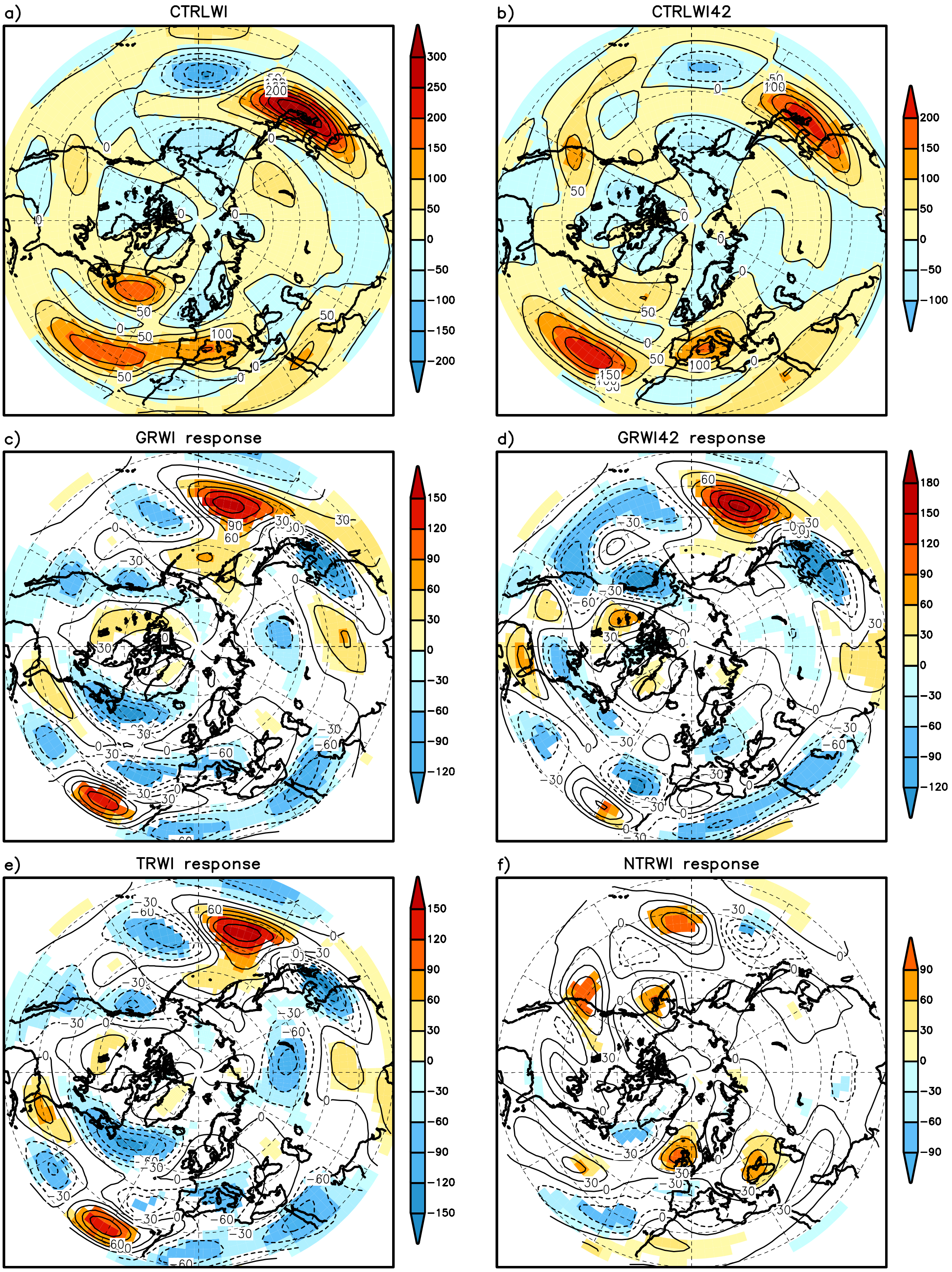

Figure 3.11: *Seasonal (DJF) ensemble mean stationary eddy meridional flux of zonal momentum,* $\overline{u}^*\overline{v}^*$*, at 200 hPa [*$m^2/s^2$*] in the a) CTRLWI, and b) CTRLWI42 ensemble. The ensemble mean response of* $\overline{u}^*\overline{v}^*$ *is shown for the c) GRWI, d) GRWI42, e) TRWI, and f) NTRWI ensemble. Color in panels c-f denotes significance at the 95% level according to a t-test.*

In the T42 experiment, a stronger response is simulated over the North Eastern Pacific and the North American continent, compared to T106. Furthermore, the wavelike response structure (Fig. 3.10 c,d) is striking at both resolutions, but only at T106 resolution the wavelike response follows a great circle path extending into the North Atlantic. At T42 resolution, the downstream response forms a purely meridionally oriented dipole over the North Atlantic. This may have an impact over Europe. A comparison between the global and the tropical Pacific regression experiments (GRWI, TRWI) reveals a striking similarity in the simulated response, as found for the mean response (ch. 3.1).

Similar arguments as for $\overline{v}^*\overline{T}^*$ hold for the stationary eddy meridional flux of zonal momentum, $\overline{u}^*\overline{v}^*$, under climatological conditions (Fig. 3.11). Again, the El Niño response is different at different resolutions (Fig. 3.11 c,d), both in structure and amplitude. GRWI42 simulates a much stronger response than GRWI over the north eastern Pacific. In contrast, the T106 response over the north western North Atlantic is much stronger than in the T42 experiment. The overall wavelike response, however, is reminiscent of a pure longitudinal shift of the climatological stationary wave pattern. In the GRWI experiment, the regions with the largest $\overline{u}^*\overline{v}^*$ response are almost 180° in longitude apart. This indicates the global impact of the ENSO-related forcing. Again, the GRWI and TRWI responses are nearly identical, even in far downstream regions. Comparing the two tropical Pacific-only experiments (TRWI, NTRWI), no clear symmetry can be identified.

In order to further study the behaviour of the stationary waves and their modification under ENSO conditions, the Plumb vector (see Appendix, Eq. A.1) is computed. Since the Plumb vector, $\vec{F_s}$, is directed parallel to the group velocity in the limit of nearly-plane stationary waves, it can be interpreted as a measure for energy propagation due to stationary waves (Plumb, 1985). Here, the horizontal components of the Plumb vector are derived for each ensemble from the seasonal (DJF) mean streamfunction ψ^* at the 300 hPa level with the zonal average subtracted. In order to determine the vertical component, the corresponding ψ^* data from the 850 hPa level are also used.

The stationary wave activity flux simulated by the two control ensembles (CTRLWI, CTRLWI42) and the four regression-based experiments is shown in Fig. 3.12. All ensembles show largely positive values for the vertical component, i.e. stationary wave activity propagates upward. Almost no downward propagation is found. The vertical component can be interpreted as the divergence of the Plumb vector. By plotting the vertical component, the major source regions of stationary wave activity become evident.

The basic climatological patterns and amplitudes found by Plumb (1985) (his Fig. 4) are well simulated in the two control ensembles (Fig. 3.12 a,b). Both control ensembles exhibit two major wave trains directed eastward and equatorward: from east Asia across the north western Pacific and across the North Atlantic. A remarkable bifurcation of the Plumb vector field is simulated over the north western Pacific, while no such splitting into a zonally oriented branch and an equatorward directed branch of stationary wave propagation is evident over the North Atlantic.

As is shown in Fig. 3.12 c-f, the stationary wave activity flux undergoes considerable changes under ENSO conditions. Over the north eastern Pacific, $\vec{F_s}$ changes from a nearly zonal orientation in the CTRLWI (Fig. 3.12a) experiment to a north-eastward direction

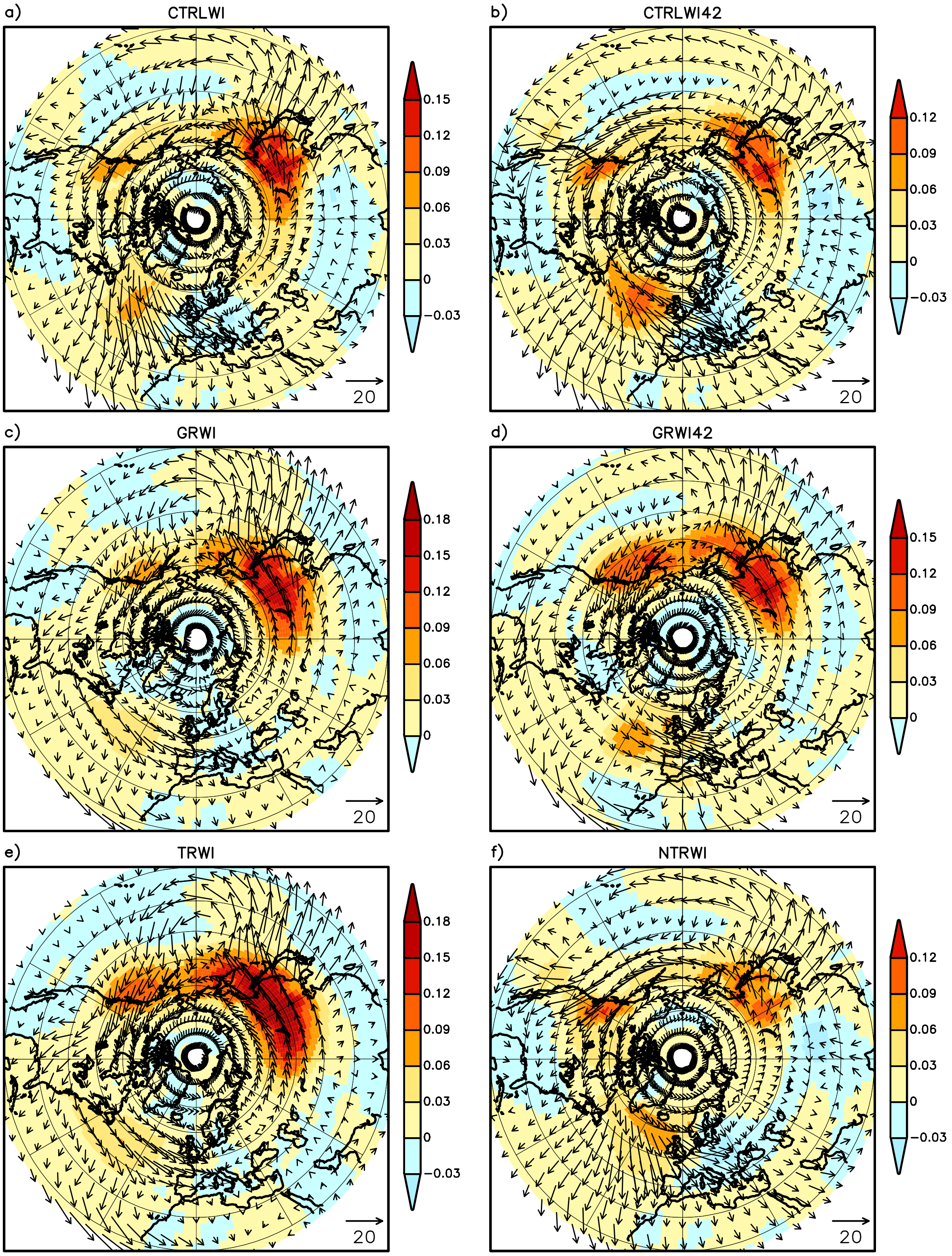

Figure 3.12: *Stationary wave activity flux (DJF) at 300 hPa [m^2/s^2] as simulated in the a) CTRLWI, b) CTRLWI42, c) GRWI, d) GRWI42, e) TRWI, and f) NTRWI ensemble. The horizontal components of the 3D-Plumb vector are indicated by the vector field (see lower right corners for scaling vector). Color denotes the vertical component of the Plumb vector.*

in the GRWI experiment (Fig. 3.12c), implying poleward energy propagation there. This clear change in direction is also evident at T42 resolution, accompanied by an increase in the vertical energy propagation (see shading). Also obvious are the changes over the North American continent and the North Atlantic sector. More wave activity is simulated over the continent in the GRWI and TRWI experiments, and the picture changes completely over the North Atlantic from southeastward to almost zonal and clearly weakened propagation into Europe. The results for global and tropical-Pacific-only SSTA forcings are very similar.

Stationary wave energy propagates poleward in the central north Pacific, especially in the high resolution experiments CTRLWI, GRWI and TRWI (Fig. 3.12 a,c,e), and generally no stationary wave propagation out of the tropics into midlatitudes is simulated.

The Plumb vector field simulated by the La Niña ensemble (NTRWI) points to some nonlinearity in the stationary wave activity changes. Fig. 3.12f exhibits a large similarity to the CTRLWI simulation, and not many changes occur in the La Niña experiment, with the only exceptions of the central North Pacific and western North America.

Regarding the vertical component, the most coherent changes with respect to the control experiment are simulated by the TRWI experiment over the North Pacific, where more energy propagates upward and poleward in the El Niño case. This may in part be related to the mean response intensification of the Aleutian low. This intensification results in cold air outflow from the American continent over the ocean, thereby increasing the baroclinicity in that region, which in turn could induce a feedback leading to the excitation of stationary wave trains.

3.2.2 Transient eddies

The atmospheric circulation is not only characterized by deviations from the zonal mean (see ch. 3.2.1) but also exhibits important fluctuations with respect to the time mean circulation (transient eddies). Under climatological conditions, transient eddies, particularly at synoptic timescales, have been studied extensively (Blackmon et al., 1977; Chang et al., 2002), since they are associated, for instance, with rain-bearing frontal systems and therefore with regional and local weather phenomena. Furthermore, transient eddies play an important role for the meridional fluxes of heat and momentum. The details of their relationship to the mean flow, their interaction with the stationary waves and their feedback onto the mean flow are still a matter of intense scientific discussion.

In order to analyze transient fluctuations with respect to their subseasonal behaviour, Blackmon's (1976) classical filtering algorithm is applied to the 12-hourly model output of the ECHAM4 experiments. As in this early study, fluctuations are classified into the following frequency bands:

- the *bandpass (bp)* regime, i.e. periods of 2.5-6 days
- the *lowpass (lp)* regime, i.e. periods of 10-90 days

In some other studies, a modified bandpass filter is used in order to retain fluctuations with periods of 2-8 days (e.g. Trenberth, 1991). However, Blackmon's (1976) approach is adopted here for a clear distinction between low-frequency phenomena like blocking and the synoptic disturbances.

The eddy variances and covariances (eddy fluxes hereafter) are calculated for each frequency band and for each ensemble member of the control and sensitivity experiments and ensemble-averaged afterwards. The transient eddy behaviour is also analyzed from an energetic point of view.

The changes described for the seasonal mean flow and the stationary eddies are often regarded as a background for changes in the transient eddies. Branstator (1995) has shown that storm tracks are organized by the large-scale mean flow. Here, the eddy feedback on the mean flow is also discussed.

3.2.2.1 Storm tracks and transient eddy fluxes

The existence and location of climatological storm tracks were described in numerous studies (see Chang et al. (2002) for a review). Their simulation in the ECHAM4 model has been shown in Fig. 2.2. Cyclogenesis is confined to regions of strong land-sea temperature contrasts and therefore of strong baroclinicity. As a measure of baroclinicity, the Eady growth rate or baroclinicity index

$$\sigma_{BI} = 0.31\, f \left|\frac{\partial \vec{v}}{\partial z}\right| / \mathcal{N} \tag{3.4}$$

is computed according to Hoskins and Valdes (1990) (see Appendix).

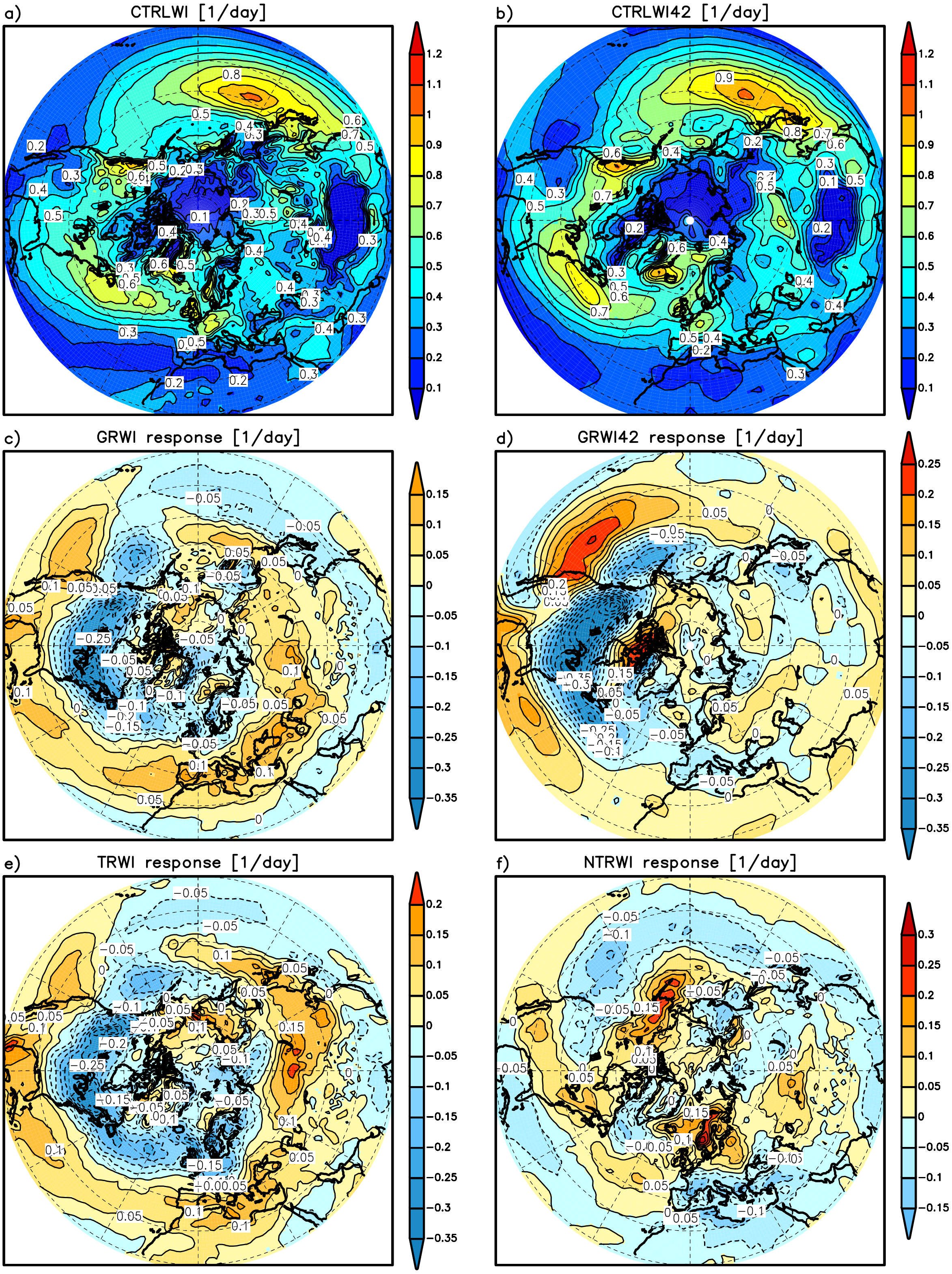

Figure 3.13: *Seasonal (DJF) ensemble mean Eady growth rate, σ_{BI}, [day^{-1}] as simulated in the a) CTRLWI and b) CTRLWI42 ensemble. The ensemble mean response of σ_{BI} is shown for the c) GRWI, d) GRWI42, e) TRWI and f) NTRWI ensemble.*

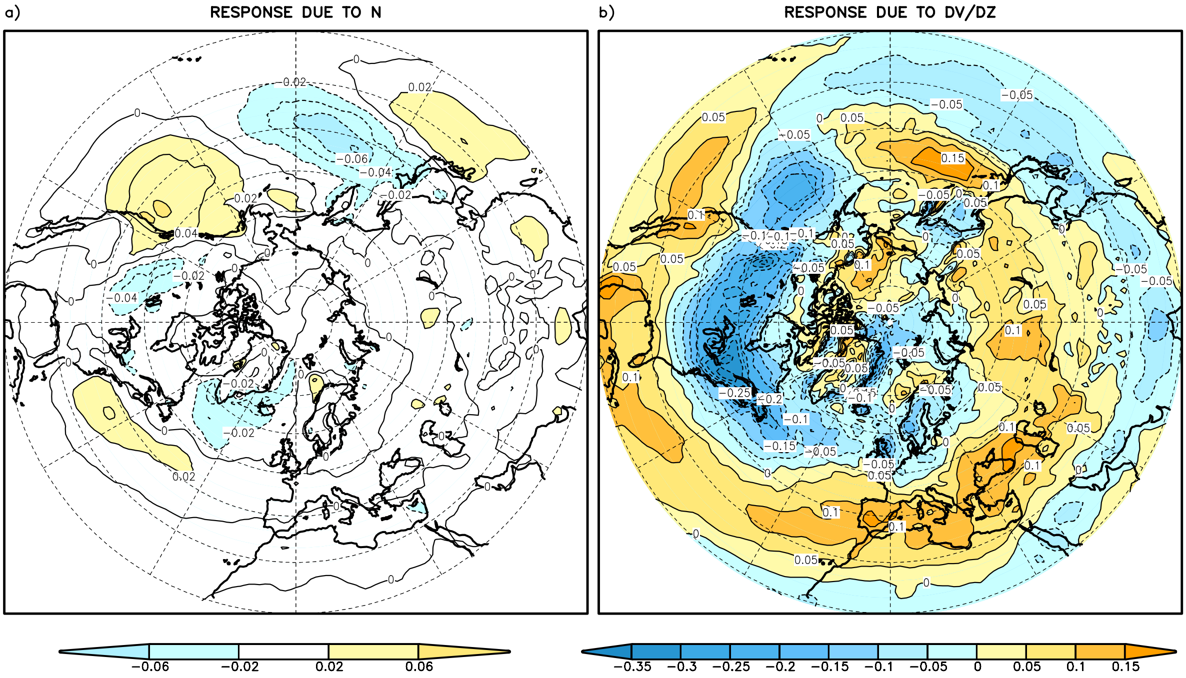

Figure 3.14: *Seasonal (DJF) GRWI ensemble mean response of the Eady growth rate, σ_{BI}, [day^{-1}] at 850 hPa a) due to changes in static stability, $\mathcal{N}$, and b) due to changes in the vertical wind shear, $|d\vec{v}/dz|$.*

The Coriolis parameter is denoted by f, $\vec{v}$ is the horizontal wind vector, z the vertical coordinate and $\mathcal{N}$ the Brunt Väisälä frequency. The vertical gradients are calculated using differences between the 1000 hPa and 700 hPa levels. The resulting climatology of σ_{BI} is presented at the 850 hPa level for both T106 and T42 resolutions (Fig. 3.13 a,b). Similar calculations for the middle and upper troposphere based on the 700 hPa, 500 hPa and 300 hPa levels lead to slightly higher amplitudes but similar results, and are therefore not shown. Due to the relatively low level, the patterns over high mountains should be interpreted with caution. Regions of high σ_{BI} are simulated over the north western Pacific, with slightly higher amplitudes in the T42 simulation (Fig. 3.13b). Over the north western Atlantic, the T42 experiment exhibits a more zonally oriented lobe concentrated in the western part of the Atlantic. In contrast, a southwest-northeast orientation dominates in the T106 experiment with higher growth rates over the central North Atlantic. Areas of high σ_{BI} indicate the potential for extratropical cyclones to develop (Hoskins and Valdes, 1990). A closer comparison, however, with the storm track activity given by the root-mean-square of the bandpass-filtered 500 hPa geopotential height, $\sqrt{\overline{z'^2_{bp}}}$ (shown in Fig. 2.2), reveals that the patterns of σ_{BI} do not exactly correspond to the storm track regions. The regions of maximum eddy activity are rather located downstream of the regions of major diabatic heating. This is in good agreement with Chang and Orlanski (1993) who demonstrate a downstream extension of the storm track over less baroclinic regions.

Next, the σ_{BI} changes during El Niño/La Niña events (Fig. 3.13 c-f) are investigated. Considerable changes are simulated by the global regression experiments (GRWI, GRWI42) over the Pacific/North American region, with a stronger response in the T42 experiment (Fig. 3.13 c,d). The decrease in baroclinicity simulated by GRWI (Fig. 3.13c) extends further eastward into northern Europe. The comparison of the two T106 El Niño experiments (Fig. 3.13 c,e) reveals strikingly similar changes in σ_{BI}. In the tropical Pacific La Niña experiment (NTRWI), only a very weak response is simulated (Fig. 3.13f), exhibiting in some areas the same sign as the response simulated by TRWI.
According to the definition of σ_{BI}, changes in baroclinicity can be caused either by changes in the vertical wind shear or by changes in the static stability. A Taylor series expansion of the σ_{BI} changes (see Appendix) reveals that, in all the response experiments, major changes in baroclinicity can be attributed to changes in the vertical wind shear. This is shown for the global regression El Niño experiment (GRWI) in Fig. 3.14. It illustrates that the changes in static stability are typically an order of magnitude smaller than those in the vertical wind shear.

The root-mean-square of the bandpass-filtered 500 hPa geopotential height is commonly used as an indicator for baroclinic activity on the synoptic timescale. The $\sqrt{\overline{z'^{2}_{bp}}}$ response for the different sensitivity experiments with respect to the control experiments (Fig. 2.2) is presented in Fig. 3.15. The significant decrease in storm track activity at northern latitudes and the significant increase to the south of it can be interpreted as North Atlantic cyclones following a more southerly route into Europe. In spite of the weaker response at T106 resolution compared to T42, the T106 response again extends further eastward across the North Atlantic into Europe. This is also valid for the tropical Pacific-only (TRWI) experiment (c) which exhibits a spatially more coherent structure, with significant anomalies extending from the Pacific across the North American continent into the North Atlantic sector. For the La Niña case (NTRWI), the picture is much less clear. The main response is simulated over the central North Pacific, where the baroclinicity is enhanced. It is a common feature of all panels in Fig. 3.15 that the magnitude of the response over the North Atlantic high latitudes exceeds the response at lower latitudes. It can be speculated that at least at the transient eddy scale, the signal is communicated from the North Pacific into the North Atlantic and not via a tropical bridge.

Motivated by the significant changes in the $\sqrt{\overline{z'^{2}_{bp}}}$ patterns, the changes in individual cyclone tracks under ENSO conditions are additionally investigated. For this purpose, a cyclone tracking analysis is performed based on the tracking algorithm developed by Blender et al. (1997) to study extratropical cyclone activity (see Appendix for details). Fig. 3.16 illustrates the relative change in cyclone origins within 10° latitude intervals in the North Atlantic sector (60°W-10°W). The number of cyclone origins is considerably increased (up to 75%) between 30°N and 50°N and decreased further to the north in the T106 El Niño experiments (GRWI, TRWI), while at T42 resolution, no clear signal can be identified. The reverse can be found in the La Niña case (Fig. 3.16d) with an indication for a more northward shifted cyclogenesis. When these results are compared to the changes in storm track activity (Fig. 3.15), it should be kept in mind that geopotential

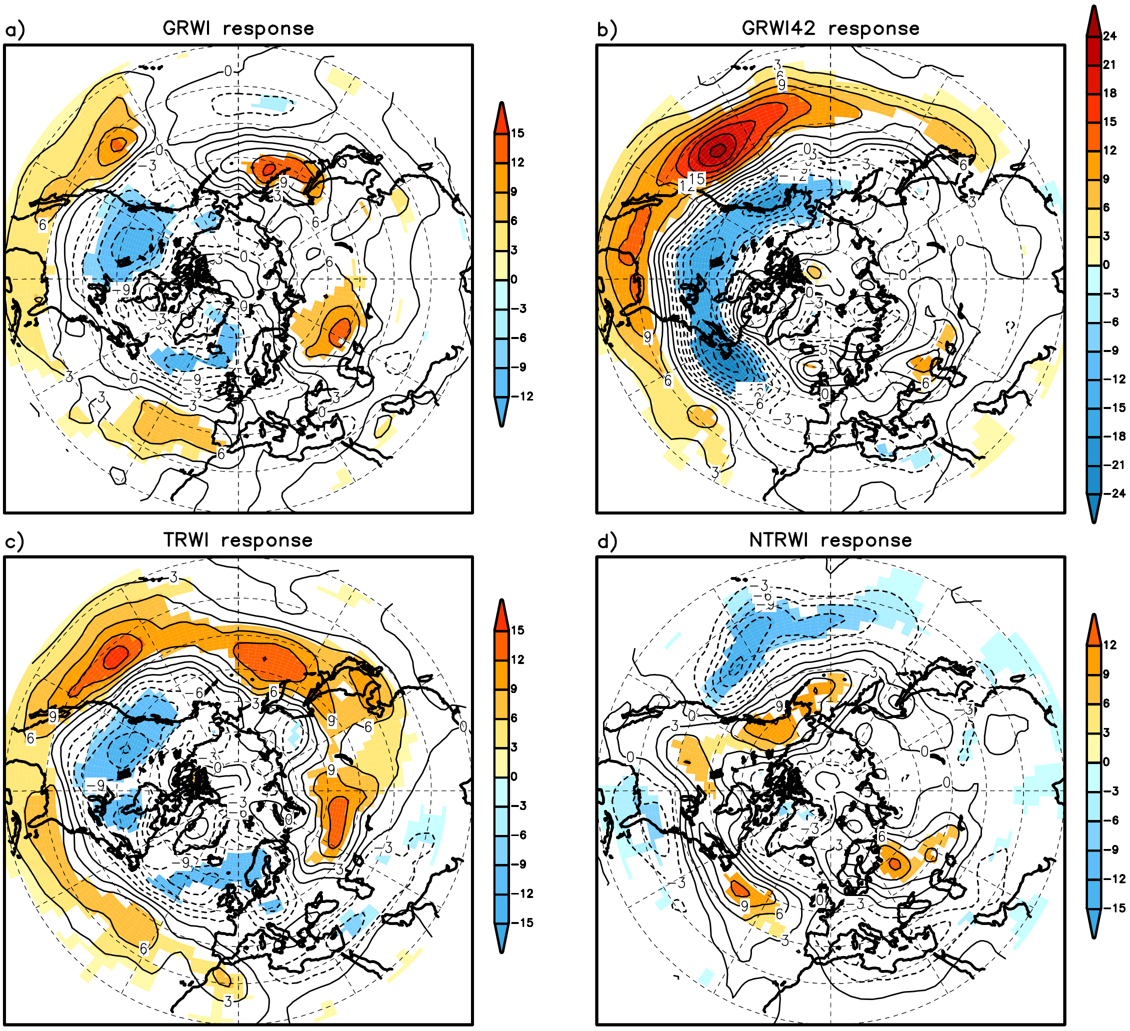

Figure 3.15: *Seasonal (DJF) ensemble mean response of the root-mean-square of the bandpass-filtered (2.5-6 d) geopotential height [gpm] at 500 hPa in the a) GRWI, b) GRWI42, c) TRWI, d) NTRWI ensemble. Color denotes significance at the 95% level according to a t-test.*

height variance is not only influenced by the formation of cyclones but also by travelling high and low pressure systems. Further analysis of the cyclone tracks (not shown) reveals a higher (lower) density of cyclone tracks in the central North Atlantic (60°W-30°W, south of 50°N) during El Niño (La Niña) situations at all resolutions. Comparison between the T106 and T42 El Niño experiments (GRWI, GRWI42), however, reveals that the general southward shift of the tracks into Europe is more pronounced at T106 resolution (not shown).

The life-cycles of individual cyclones are associated with meridional transports of eddy temperature, $\overline{v'T'}$, and eddy zonal momentum, $\overline{u'v'}$. As the stationary eddies, transient eddies are responsible for considerable latitudinal heat transports. In contrast to the cyclone scale, the *lowpass (10-90 d)* eddy fluxes do not exhibit a significant response. The

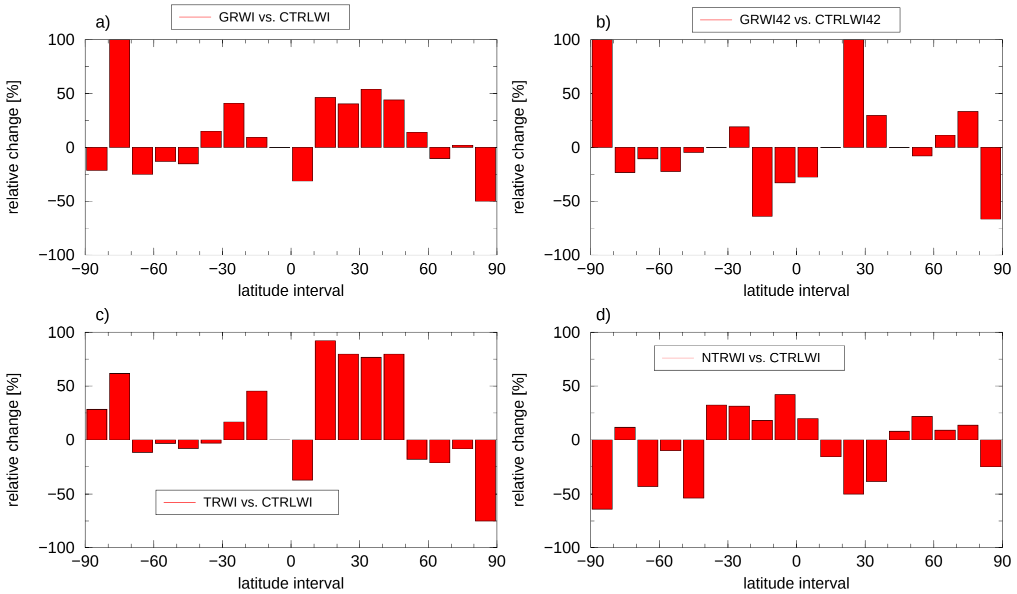

Figure 3.16: *Relative change [%] in number of cyclone origins per 10° latitude interval in the Atlantic region (60° W-10° W) as simulated by the a) GRWI, b) GRWI42, c) TRWI, and d) NTRWI ensemble.*

discussion is therefore restricted to the *bandpass (2.5-6 d)* range.

The ensemble mean response of the meridional eddy heat flux, $\overline{(v'T')}_{bp}$, at the 700 hPa level (not shown) largely corresponds to the changes in the storm tracks as indicated by $\sqrt{\overline{z'^2_{bp}}}$, with reduced poleward eddy heat fluxes. This can be related to the time mean temperature response over North America: reduced baroclinicity induces less meridional heat exchange.

The importance of the upper-tropospheric meridional eddy flux of zonal momentum, $\overline{(u'v')}_{bp}$, at the 200 hPa level for the mean flow has been shown by Hoskins et al. (1983). The $\overline{(u'v')}_{bp}$ fields simulated in the control integrations (CTRLWI, CTRLWI42) are displayed in Fig. 3.17 (a,b) with positive values indicating a poleward flux of eddy zonal momentum. The simulated patterns are consistent with observations (Blackmon et al., 1977; James, 1994), which reveal a strong convergence of $\overline{(u'v')}_{bp}$ particularly downstream of the major jet stream regions over the central North Pacific and the North Atlantic. Slightly higher amplitudes are reached at T106 resolution compared to T42 over the North American and the European continent, while stronger negative values are simulated over the eastern North Atlantic at T42 resolution.

The response patterns simulated in the El Niño experiments (GRWI, GRWI42, TRWI) can all be characterized by a strong weakening or even a reversal of the meridional eddy zonal momentum flux over North America and the North Atlantic (Fig. 3.17 c-e). Over the eastern North Atlantic, the climatological meridional gradient is considerably weakened in the GRWI and TRWI experiments, thereby leading to reduced eddy momentum flux convergence, and thus probably to a reduced eddy forcing onto the mean flow. The clear reduction of the poleward $\overline{(u'v')}_{bp}$ flux over the North American continent leads to a weakened convergence over the North American continent. Over the southern North

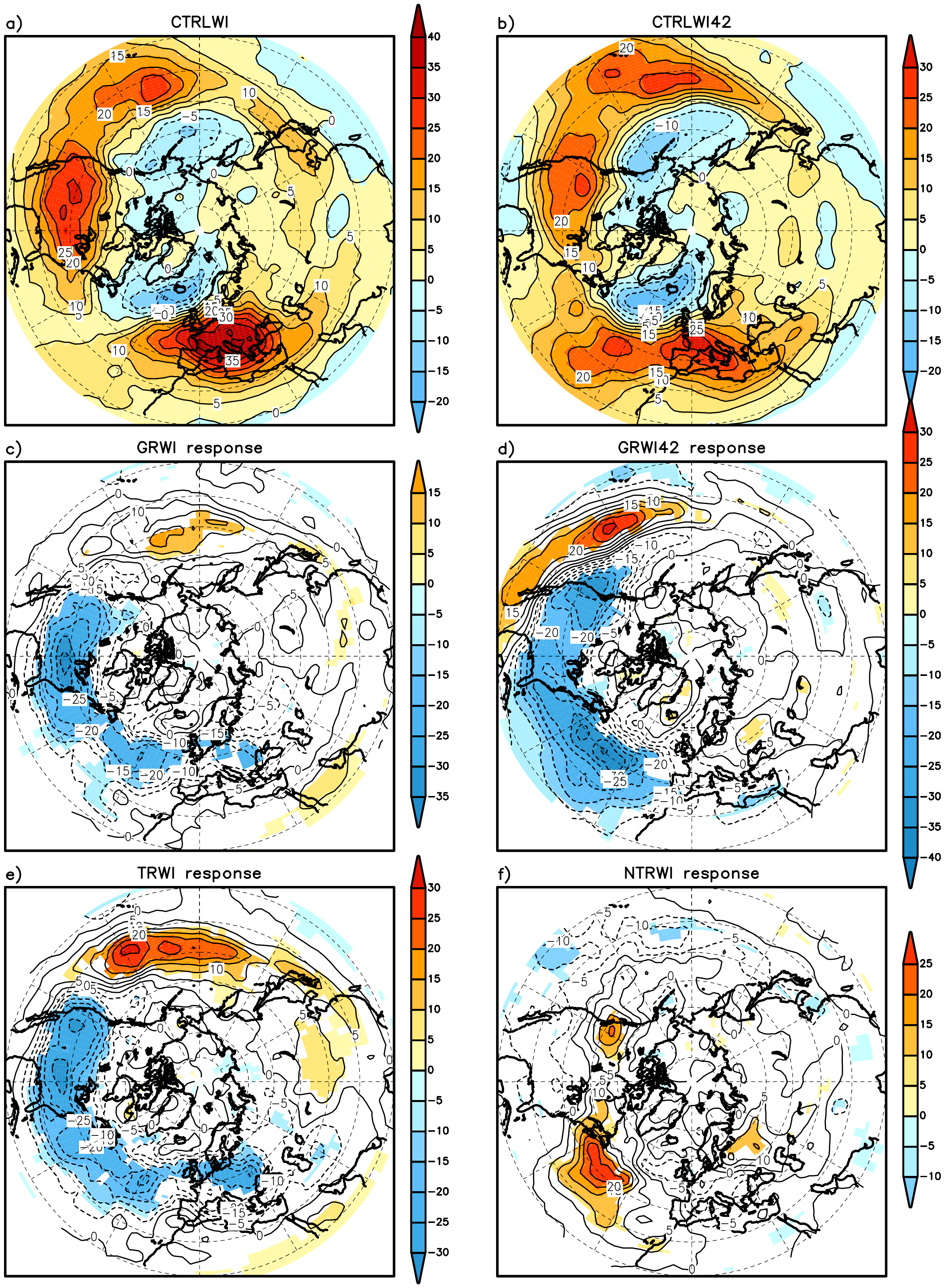

Figure 3.17: *Seasonal (DJF) ensemble mean response of the bandpass-filtered (2.5-6 d) eddy meridional flux of zonal momentum at 200 hPa* [m^2/s^2] *in the a) CTRLWI, and b) CTRLWI42 ensemble. The ensemble mean response of* $\overline{u'v'}$ *is shown for the c) GRWI, d) GRWI42, e) TRWI and f) NTRWI ensemble. Color denotes significance at the 95% level according to a t-test.*

American continent, however, the poleward fluxes are even reversed in the GRWI simulation which might be conducive to a strengthening of the subtropical jet in the Caribbean. In the La Niña experiment (Fig. 3.17f), the most important changes are simulated over the central North Atlantic. Here, the poleward flux of eddy zonal momentum is significantly enhanced which is consistent with the changes in storm track activity (Fig. 3.15d). The role of the eddies in feeding back onto the time mean flow is further discussed in the following section from an energetic point of view.

3.2.2.2 Energetic considerations

As has been illustrated in the previous part, transient eddies are characterized by strong longitudinal variations regarding their structure and amplitude. This section seeks to elucidate the atmospheric ENSO response from an energetic point of view.
With the definitions for the mean flow kinetic energy, K_m, and transient eddy kinetic energy, K_e,

$$\begin{aligned} K_m &= 0.5\,(\overline{u}^2 + \overline{v}^2) && (3.5) \\ K_e &= 0.5\,(u'^2 + v'^2) && (3.6) \end{aligned}$$

budgets of the mean flow kinetic energy and eddy kinetic energy can be derived from the standard momentum and hydrostatic equations. Here, only the equation for the transient eddy kinetic energy is considered. A formulation for the prognostic K_e equation is given by Chang and Orlanski (1993) (their eq. 6.3).

$$\frac{\partial K_e}{\partial t} + \vec{v}_3' \cdot \nabla K_e = -(\nabla \cdot \vec{v}_3'\varphi) + g\theta_0^{-1} w\theta' - \vec{v}' \cdot (\vec{v}_3' \cdot \nabla \overline{\vec{v}}) + \vec{v}' \cdot \overline{(\vec{v}_3' \cdot \nabla \vec{v}')} + dissip. \quad (3.7)$$

with the subscript 3 denoting three-dimensional vectors, φ denoting geopotential height, w the vertical wind component, and θ_0 and θ' the reference state potential temperature and potential temperature variation, respectively.
In the present context, the (diagnostic) time-averaged equation for eddy kinetic energy is discussed on a seasonal mean basis. It can be shown that in the time mean, the K_e equation can be approximated as follows (see Appendix for details)

$$\begin{aligned} \nabla \cdot \overline{\vec{v}}\,\overline{K_e} + \nabla \cdot \overline{\vec{v}' K_e'} &= -\nabla \cdot \overline{\vec{v}_a{}'\varphi'} - \frac{\partial \overline{\omega'\varphi'}}{\partial p} - \overline{\omega'\alpha'} + \vec{E} \cdot \nabla \overline{u} + dissip. && (3.8) \\ &= \underbrace{f(\overline{u'v_a'} - \overline{v'u_a'})}_{baroclinic\ production} + \underbrace{\vec{E} \cdot \nabla \overline{u}}_{barotropic\ production} + dissip. && (3.9) \end{aligned}$$

with the subscript a denoting the ageostrophic wind components, $\alpha = \partial\varphi/\partial p$ denoting the inverse of density, and $\vec{E} = (\overline{v'^2 - u'^2}, -\overline{u'v'})$ represents the $\vec{E}$-vector as defined by Hoskins et al. (1983) based on the transient eddy wind components, (u', v').
The r.h.s. of Eq. (3.9) contains source and sink terms for K_e which are balanced by the mean flow and eddy advection terms on the left. In the remainder of this section, I focus on these source and sink terms on the right which contribute to the generation or destruction of eddy kinetic energy.

The analysis is performed at the 300 hPa level. This level is chosen since eddy kinetic energy reaches its highest amplitude in the upper troposphere (not shown). In contrast to other studies, no vertical average of the transient eddy kinetic energy equation is calculated. Thus, the terms calculated at one level do not necessarily represent the net contribution to the total budget since the terms may change in sign between different tropospheric levels. Typically, the terms do not change their sign (except for dissipation and the Ekman-pumping term) but increase in amplitude (Frisius, personal communication). Hence, the approach used here is justified, since the dominant contributions are provided by the upper troposphere.

a) Baroclinic production

Baroclinic production (BCP hereafter) represents a combination of different contributions. The first term on the right of Eq. (3.8) is the divergence of the ageostrophic geopotential flux and has been shown to be very important locally (Orlanski and Katzfey, 1991). Ageostrophic fluxes act to generate eddy kinetic energy at the jet stream level over the western parts of the oceans (Blackmon et al., 1977; Lau, 1979). Positive covariances of $-\overline{\omega' T'}$ (not shown), i.e. rising (sinking) motion of positive (negative) temperature perturbations, indicate a thermally direct circulation. For continuity reasons, this is associated with cross-isobaric flow. The $\overline{\omega' \alpha'}$ term in Eq. (3.8) indicates the energy conversion between eddy available potential energy and eddy kinetic energy. This conversion is related to vertical eddy temperature fluxes. Hence, a BCP maximum may be interpreted as a gain of K_e from either pure energy conversion or due to the divergence of geopotential fluxes or both.

The total BCP is analyzed according to Eq. (3.9). The spatial patterns and amplitudes of BCP as simulated by the control experiments (CTRLWI, CTRLWI42) are comparable at both resolutions. The largest positive amplitudes can be found over the open oceans (not shown) and indicate a gain of K_e due to baroclinic processes.

The assessment of the BCP changes due to ENSO is difficult since the responses exhibit a rather small-scale structure in all sensitivity experiments even when the data are interpolated to T42 resolution for smoothing purposes. Furthermore, the changes in BCP are found to be hardly significant (not shown).

b) Barotropic production

In contrast to BCP, the barotropic production (Eq. (3.8), fourth term) is a pure conversion term (BTP hereafter). It can provide some insight into the conversion between transient eddy and mean flow kinetic energy ($K_e \Leftrightarrow K_m$). The dot product of the $\vec{E}$-vector and the gradient of the mean zonal wind is a good approximation to the barotropic production of K_e (Wallace and Lau, 1985). The production or destruction of K_e by barotropic conversion depends on the position of the $\vec{E}$-vector relative to the gradient of the zonal wind. In other words, barotropic conversion of K_m (K_e) into K_e (K_m) is at a maximum if $\vec{E}$ is directed up (down) the gradient of $\overline{u}$.

$$\vec{E} \cdot \nabla \overline{u} > 0 \quad \Leftrightarrow \quad \text{gain of } K_e \tag{3.10}$$

$$\vec{E} \cdot \nabla \overline{u} < 0 \quad \Leftrightarrow \quad \text{loss of } K_e \tag{3.11}$$

First, the model's capability to capture the observed climatological barotropic conversion between mean flow and eddies is analyzed on an ensemble and seasonal mean basis. Compared to observations (Wallace and Lau, 1985, their Fig. 4), a rather similar picture results for both the *unfiltered* and the *bandpass-filtered* transient eddies in the CTRLWI and CTRLWI42 experiments. In the bandpass range (Fig. 3.18 a,b), amplitudes are reduced with respect to the unfiltered data. The bandpass-filtered transient eddies ex-

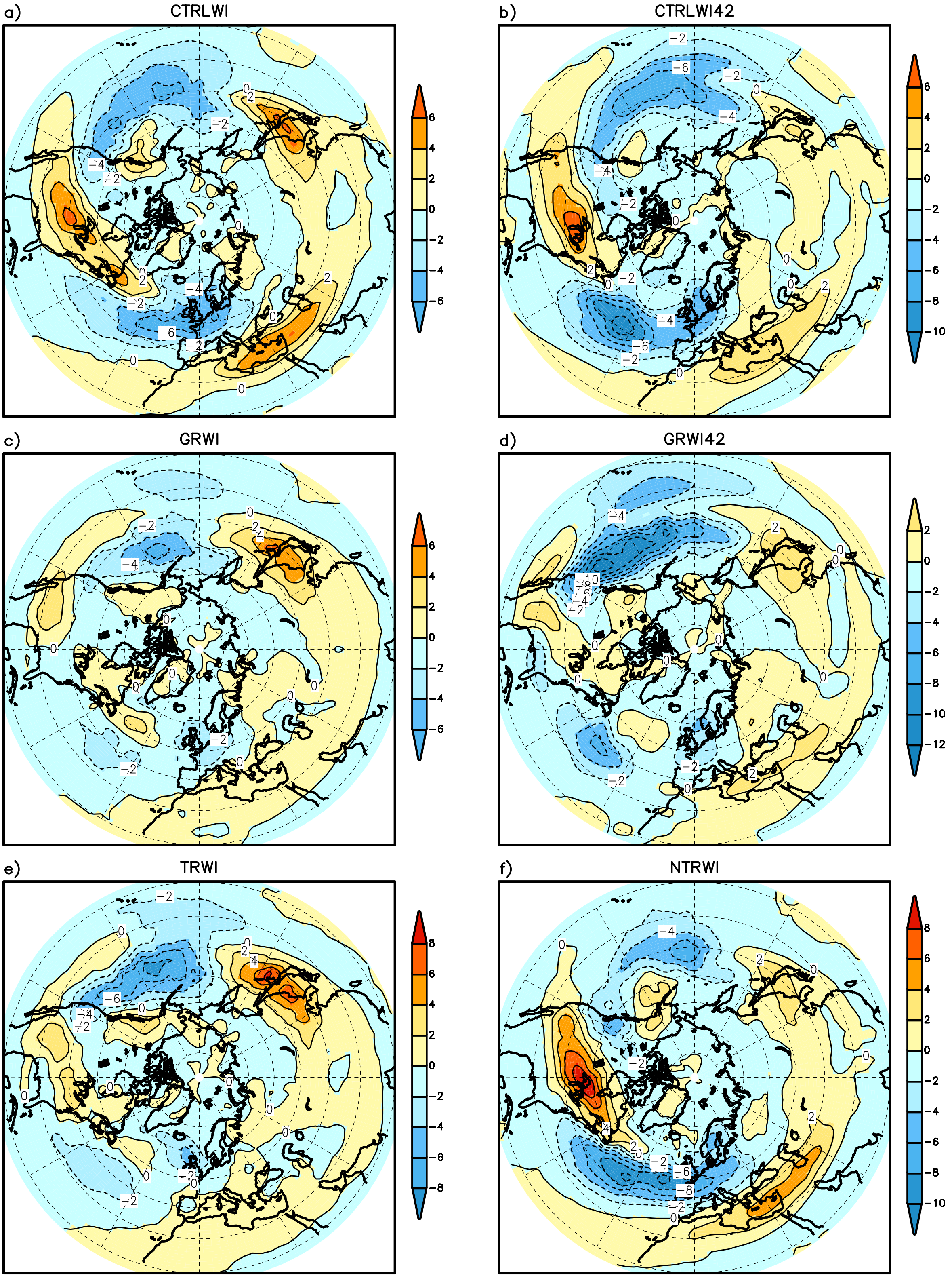

Figure 3.18: *Seasonal (DJF) ensemble mean barotropic production* $[10^{-4}m^2/s^3]$ *at 300 hPa in the bandpass range (2.5-6 d) as simulated by the a) CTRLWI, b) CTRLWI42, c) GRWI, d) GRWI42, e) TRWI, and f) NTRWI ensemble.*

tract energy from the mean flow over large parts of North America. Over most parts of the North Pacific and the North Atlantic, $\vec{E}$-vectors are directed down the gradient of $\overline{u}$, i.e. the eddies are feeding the mean flow (Fig. 3.18 a,b). In the *lowpass* range (not shown), however, the overall tendency of the transient eddies is to extract energy from the mean flow. This takes place mainly in the jet-exit regions. Thus, the ECHAM4 model reproduces the observed BTP (Wallace and Lau, 1985) well, both quantitatively and qualitatively. The only resolution dependence can be seen in the negative BTP amplitudes over the North Atlantic (Fig. 3.18 a,b) where the loss of K_e to the mean flow is larger at T42 resolution than at T106 resolution.

The BTP response with respect to ENSO is now discussed based on the regression experiments. Instead of differences, the seasonal ensemble means of BTP are shown (Fig. 3.18 c-f) to emphasize the sign of the energy transfer ($K_e \Rightarrow K_m$ or vice versa). As can be seen from Fig. 3.18c, an overall weakening of BTP is simulated by GRWI. Especially over the North American continent and the North Atlantic, conversion rates are reduced by more than 50% under El Niño conditions. The BTP simulated by the GRWI42 experiment (Fig. 3.18d) emphasizes the role of resolution. Amplitudes are found to be higher than in the T106 experiment. At T42 resolution, the loss of K_e to the mean flow is clearly stronger over the eastern North Pacific than in the T106 simulation. When the anomalous SST forcing is restricted to the tropical Pacific (TRWI experiment, Fig. 3.18e), strong similarities with the BTP simulated by GRWI are found. The barotropic conversion simulated by NTRWI (Fig. 3.18f) shows much similarity to the CTRLWI ensemble. However, the NTRWI conversion rates indicate a stronger gain of K_e over the North American continent and more loss of K_e to the mean flow over the North Atlantic.

From a purely barotropic point of view, such gains and losses of eddy kinetic energy have to be interpreted as an eddy forcing on the mean flow. The changes in the mean zonal wind at the jet stream level (u200) can be partly attributed to these changes in $\vec{E} \cdot \nabla \overline{u}$. For example, an intensification of the jet over the southern parts of North America is noted in the GRWI experiment (Fig. 3.1d). Here, the eddies extract clearly less kinetic energy from the mean flow which may partly contribute to an intensification of the mean flow there.

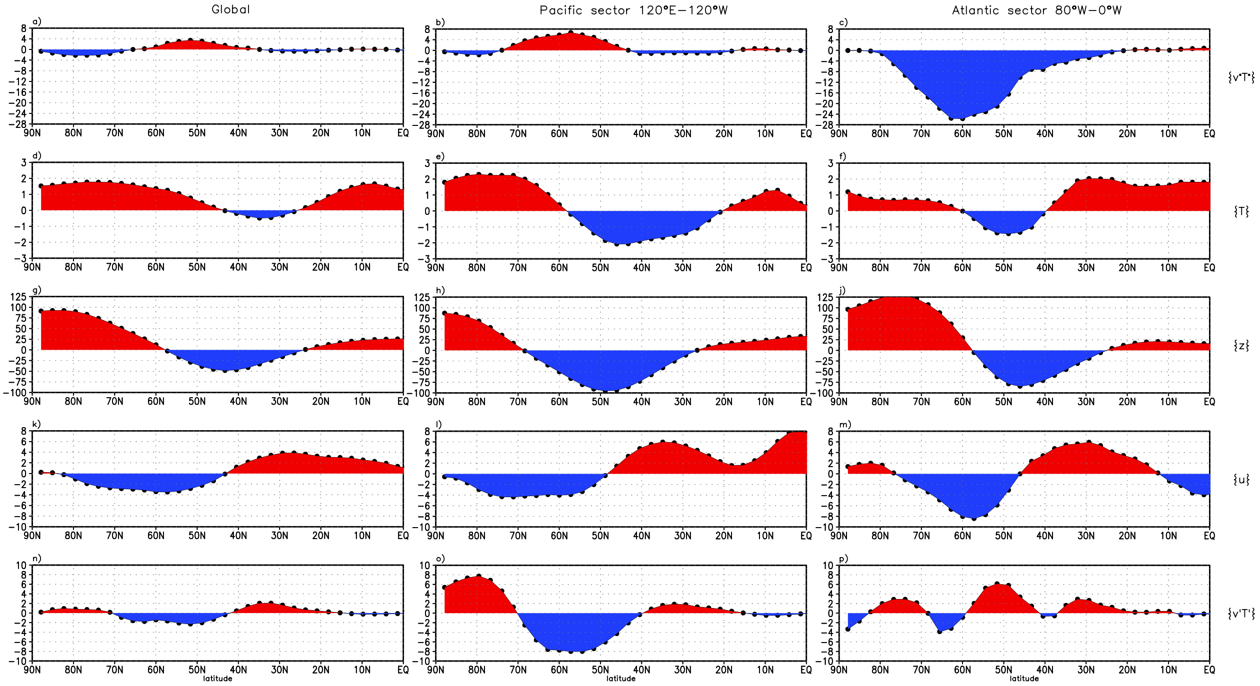

Figure 3.19: *Difference between the seasonal (DJF) ensemble mean responses of TRWI and NTRWI in the zonal average at the 700 hPa level: (a-c) stationary eddy heat flux* $\{\overline{v}^*\overline{T}^*\}$ *[K·m/s], (d-f) temperature* $\{\overline{T}\}$ *[K], (g-j) geopotential height* $\{\overline{z}\}$ *[gpm], (k-m) zonal wind* $\{\overline{u}\}$ *[m/s], (n-p) transient eddy meridional heat flux* $\{\overline{v'T'}\}$ *[K·m/s]. The zonal average has been calculated over all longitudes (left column), over the Pacific sector (middle) and the Atlantic sector (right). Note that northern latitudes increase from right to left.*

3.2.3 On the linearity of the eddy response

In section 3.1.3, the symmetry of the seasonal mean atmospheric ENSO response with respect to the sign of the forcing has been discussed. This aspect is now further pursued with special focus on the eddy quantities. Again, El Niño and La Niña situations are contrasted from the two tropical Pacific regression experiments (TRWI, NTRWI).

First, changes in the lower troposphere are analyzed at the 700 hPa level for both selected mean flow and eddy variables. Here, the difference of the seasonal (DJF) ensemble mean responses between the TRWI and NTRWI ensembles is calculated. This TRWI-NTRWI difference is zonally averaged globally (Fig. 3.19, left column) and over the Pacific (defined as 120°E-120°W) and the Atlantic (80°W-0°W) sectors, as illustrated in Fig. 3.19. The definition of the sectors is motivated by the main response areas in the hemispheric eddy flux response patterns (e.g. Fig. 3.17). Zonal averages of the transient and stationary meridional eddy heat fluxes, $\{\overline{v}^*\overline{T}^*\}$ and $\{\overline{v'T'}\}$, are compared to the zonally averaged mean temperature, zonal wind and geopotential height. The left panels of Fig. 3.19 can be directly compared to the observational results shown in van Loon and

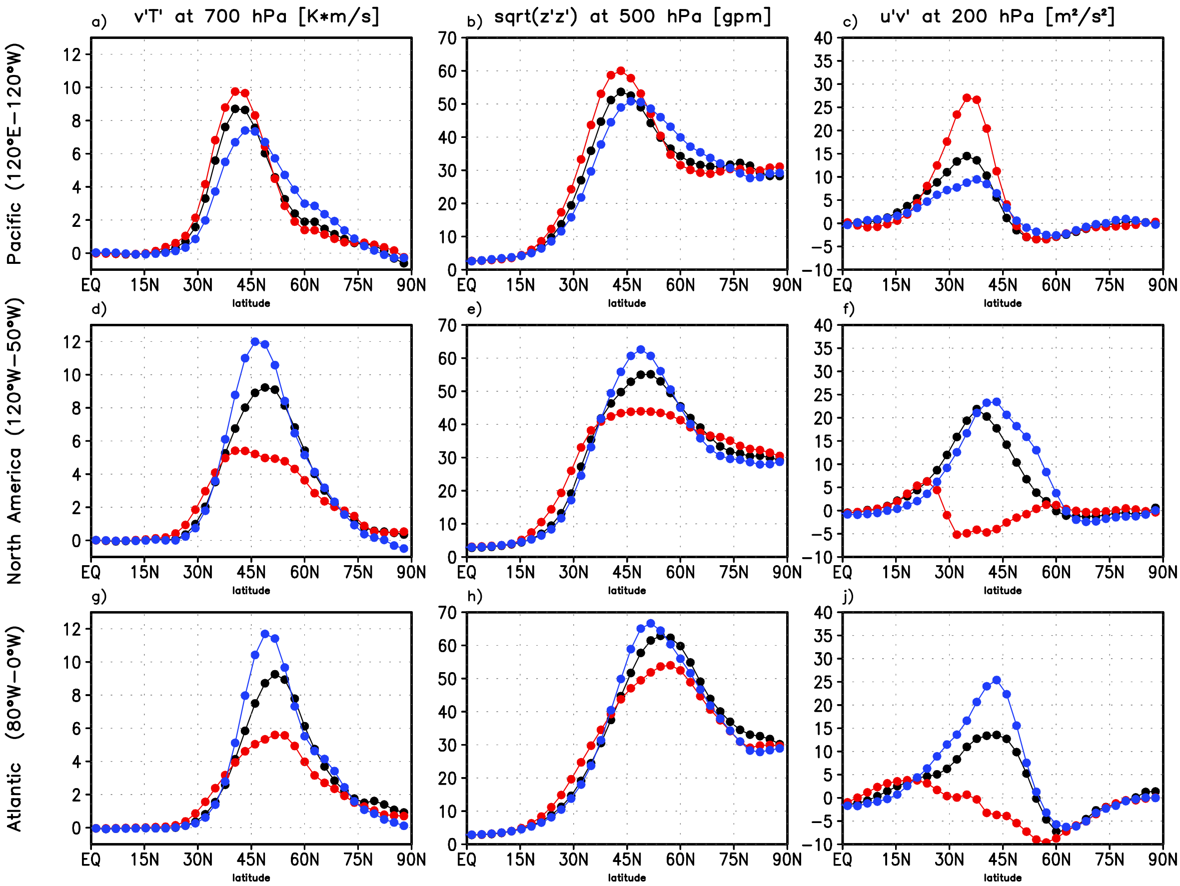

Figure 3.20: *Seasonal (DJF) ensemble mean of the zonally averaged bandpass-filtered eddy meridional heat flux at 700 hPa [K·m/s] (left panels), the root-mean-square of geopotential height at 500 hPa [gpm] (middle), and meridional eddy flux of zonal momentum at 200 hPa [m^2/s^2] (right) in the CTRLWI (black), TRWI (red), NTRWI (blue) ensembles for different longitudinal sections, as indicated on the left of each row.*

Rogers (1981) (their Fig. 1, VLR hereafter).

If the El Niño-La Niña differences are averaged *globally* (left panels), a rather close correspondence between the ECHAM4 experiments and the VLR results can be noticed. The zonally averaged geopotential height, $\{\overline{z}\}$, exhibits a strong meridional gradient with increased (reduced) $\{\overline{z}\}$ at lower (middle) latitudes. For geostrophic reasons, these $\{\overline{z}\}$ changes are consistent with the changes in the zonal wind which is intensified (weakened) south (north) of about 45°N. It can also be seen that the meridional temperature gradient and the eddy transports, $\{\overline{v}^*\overline{T}^*\}$ and $\{\overline{v'T'}\}$, are closely related. Especially the transient eddy heat fluxes are increased in regions where the meridional temperature gradient is increased. Compared to VLR, similar changes are also found for the stationary eddy heat flux, with the strongest increase between 45°N and 60°N.

If the zonal average is restricted to the *Pacific sector* (Fig. 3.19, middle panels), the basic structure of the TRWI-NTRWI fields is mainly conserved compared to the global averages. The amplitudes, however, are larger, particularly those of the eddy fluxes. Fur-

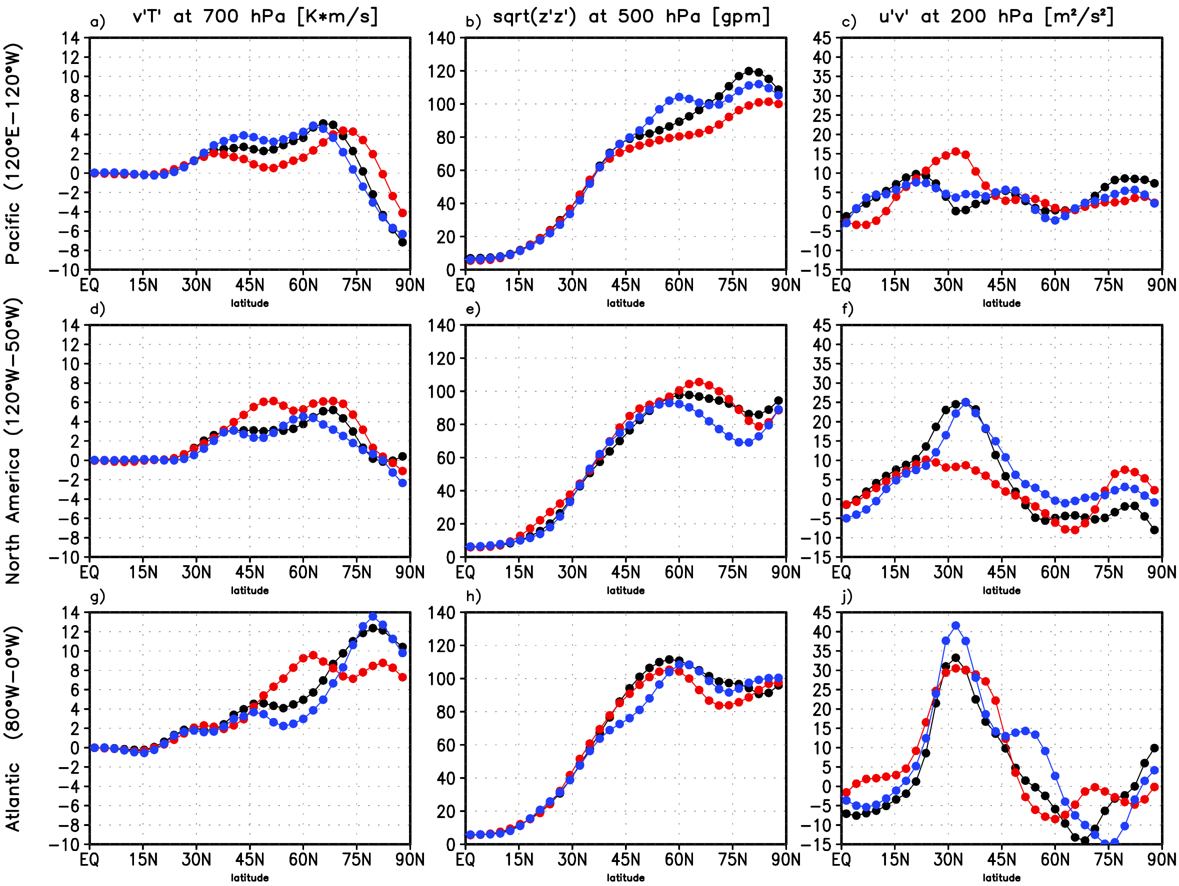

Figure 3.21: *As Fig. 3.20 for lowpass-filtered transient eddies.*

thermore, the decreases of $\{\overline{T}\}$ and $\{\overline{z}\}$ in subtropical and middle latitudes cover a larger latitudinal area than in the global average.

For the *Atlantic sector* (Fig. 3.19, right panels), the $\{\overline{v}^*\overline{T}^*\}$ TRWI-NTRWI difference changes considerably compared to the global average. The strong decrease north of 30°N is also evident from the hemispheric distribution of $\overline{v}^*\overline{T}^*$ in Fig. 3.10. Changes in $\{\overline{v'T'}\}$ exhibit a rather complex latitudinal structure. The differences in $\{\overline{T}\}$ and $\{\overline{z}\}$ cover latitudinal areas which are different from the global zonal averages. The zonal wind, $\{\overline{u}\}$, exhibits a much stronger and southward shifted decrease relative to the decrease in the Pacific sector and the global mean.

So far, the discussion has been restricted to the 700 hPa level. Next, the symmetry of the ENSO response is analyzed at different tropospheric levels. Attention is given to the zonally averaged *transient eddy fluxes in the bandpass (bp) range.* Again, the behaviour in different longitudinal sectors is investigated.

In order to cover the troposphere in its full vertical extent, seasonal (DJF) ensemble means for $\{\overline{v'T'}\}$ at the 700 hPa level, $\{\sqrt{\overline{z'^2}}\}$ at the 500 hPa level, and $\{\overline{u'v'}\}$ at the 200 hPa level are shown for the CTRLWI, TRWI and NTRWI experiments in Fig. 3.20. Generally, El Niño and La Niña events induce responses of opposite signs in the latitudes

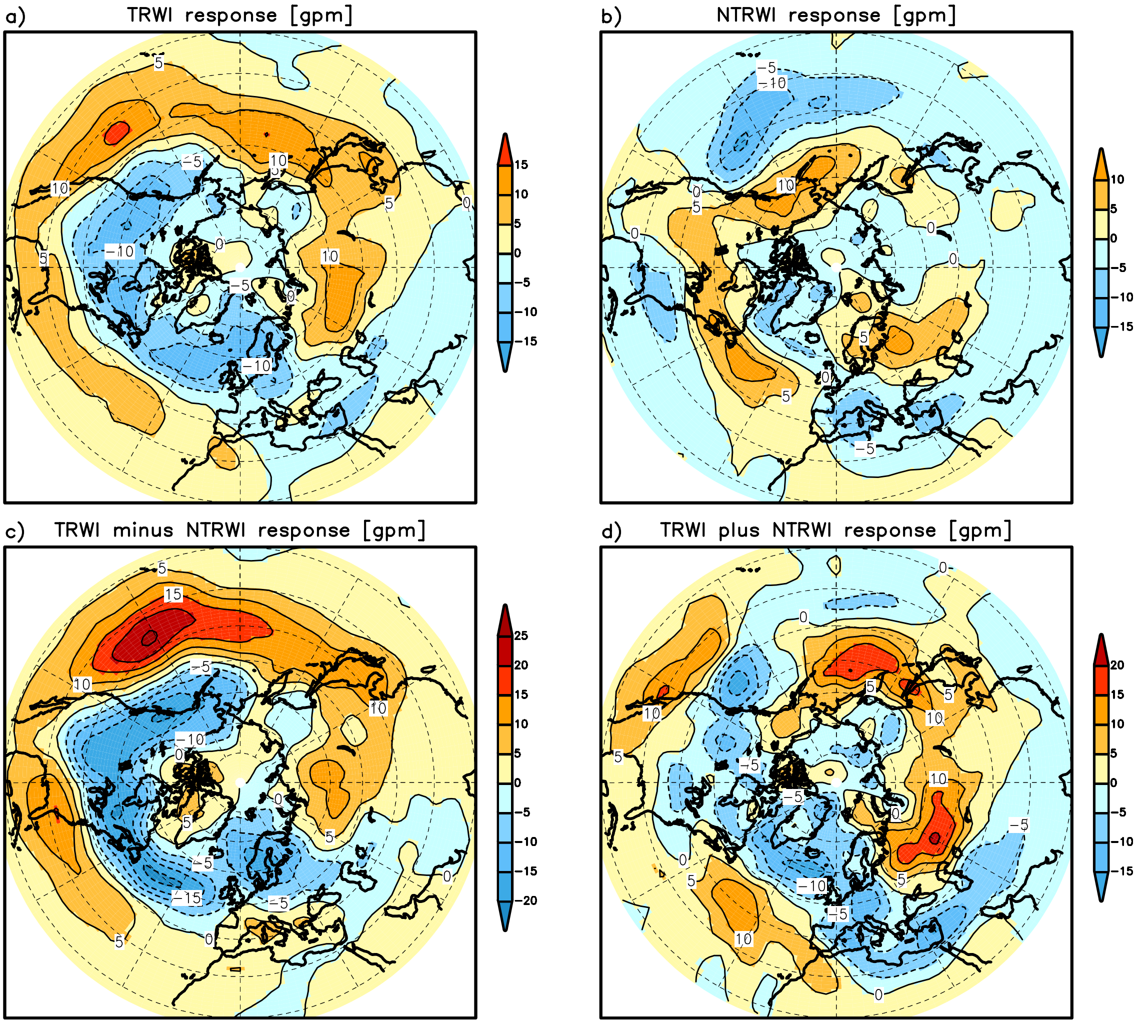

Figure 3.22: *Seasonal (DJF) ensemble mean response of the root-mean-square of the bandpass-filtered (2.5-6 d) geopotential height [gpm] at 500 hPa in the a) TRWI, and b) NTRWI ensembles. Furthermore, the difference (c) and the sum (d) of the TRWI and the NTRWI responses are displayed. No significance is indicated here in order to illustrate the mere structure.*

of major eddy activity (30°N-70°N). However, the El Niño response appears to be generally stronger. It is also evident from all panels that ENSO-related changes do not only consist of changes of the amplitude, but also of latitudinal shifts. Over the North Atlantic (lower panels), there is a weak increase in storm track activity in the El Niño ensemble south of 45° and a clear decrease to the north (Fig. 3.20h). The major response for the NTRWI ensemble consists of an increase and a slight southward shift of the maximum of $\{\sqrt{\overline{z'^2}}\}$. Only over the North American and Atlantic sectors, the $\{\overline{v'T'}\}$ responses are approximately antisymmetric.

In general, these results are in good agreement with the results on the symmetry of the mean response (ch. 3.1.3). The El Niño experiment, however, exhibits a stronger transient eddy response relative to the La Niña experiment.

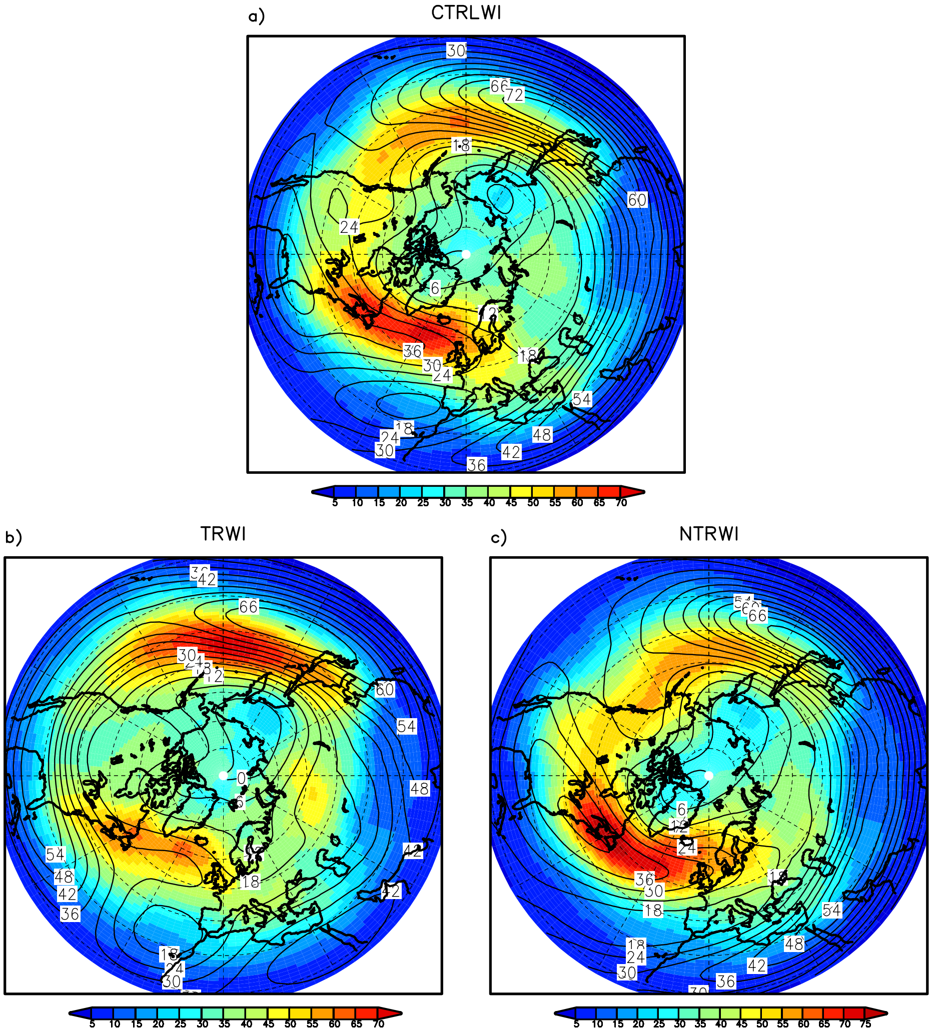

Figure 3.23: *Seasonal (DJF) ensemble mean of the zonal wind at 200 hPa [m/s] (contour lines) and the root-mean-square of the bandpass-filtered (2.5-6 d) 500 hPa geopotential height [gpm] (shaded) as simulated by the a) CTRLWI, b) TRWI, and c) NTRWI ensemble.*

In contrast to the findings for the bandpass range, there is not much evidence for symmetry in the *low-frequency* band, and no systematic response is found (Fig. 3.21).

The hemispheric $\sqrt{z_{bp}'^2}$ response is investigated next. As in Fig. 3.7 for z200, both the difference and the sum of the storm track responses as simulated in TRWI and NTRWI are shown in Fig. 3.22. The difference pattern enhances the El Niño signal indicating some antisymmetry (Fig. 3.22c). Deviations from a pure sign reversal in the response are seen especially over the North Atlantic, which emphasizes the zonal mean result from Fig. 3.20h. The dipole-like structure over the North Atlantic (Fig. 3.22d) illustrates that the main response in the La Niña experiment is located to the north of the major storm track activity increase of the El Niño experiment.
Normally, the major storm tracks on the Northern Hemisphere are located downstream

and on the poleward side of the upper-tropospheric jet streams. Fig. 3.23 illustrates the changes in this relative position under El Niño and La Niña conditions.
In the TRWI ensemble, the jet and the major storm track diverge in the latitudinal position of their maxima over the North Atlantic. The jet core is shifted towards lower latitudes where the increase in $\sqrt{\overline{z_{bp}'^2}}$ takes place. In accordance to the energetic considerations (previous section), this can be partially explained by the reduction in poleward eddy flux of zonal momentum (Fig. 3.17e) that leads to an acceleration of the mean flow further southward. Over the north western Pacific, the storm track and the jet stream maintain their relative positions (Fig. 3.23a), but stormtrack activity is increased.
In the NTRWI experiment, the North Atlantic jet core keeps its intensity but changes from a rather zonal into a more north-eastward orientation. Hence, the North Atlantic jet core tends to coincide roughly with the storm track maximum. This jet shift can at least partially be explained by the increase in poleward eddy flux of zonal momentum over the central North Atlantic. In addition, this is consistent with the stronger loss of eddy kinetic energy to the mean flow over the central North Atlantic (Fig. 3.18f).

3.3 Synthesis of the seasonal ENSO response

In this section, an effort is undertaken to draw a dynamical picture of the atmospheric ENSO response. In order to understand more thoroughly the mean response, eddy-mean-flow-interactions are now studied. Here, only the bandpass range is considered, since one major issue of this thesis is the role of resolution. The hypothesis is that the different responses over the North Atlantic at the two resolutions may arise from the different representations of synoptic-scale variability (2.5-6 days).

a) Streamfunction forcing

We start from the seasonal mean budget for the vertical component of the absolute vorticity, $\zeta = \xi + f$, with ξ denoting the relative vorticity and f the planetary vorticity, as given by Hoskins and Sardeshmukh (1987),

$$\frac{\partial \overline{\zeta}}{\partial t} \equiv 0 = -\nabla \cdot \overline{\vec{v}}\, \overline{\zeta} - \vec{k} \cdot \nabla \times \overline{\omega} \frac{\partial \overline{\vec{v}}}{\partial p} \underbrace{- \nabla(\overline{\vec{v}'\,\zeta'}) - \vec{k} \cdot \nabla \times \overline{\omega' \frac{\partial \vec{v}'}{\partial p}}}_{direct\, transient\, eddy\, forcing} \tag{3.12}$$

The last term of Eq. (3.12) represents the sum of vertical advection and twisting terms. In some studies, it is considered to be very small and therefore negligible. Together with the convergence of the transient eddy vorticity fluxes, $-\nabla(\overline{\vec{v}'\,\zeta'})$, it represents the transient eddy contributions to the seasonal mean vorticity budget. The $-\nabla(\overline{\vec{v}'\,\zeta'})$ term can be re-written by applying the Helmholtz theorem. Accordingly, the horizontal wind $\vec{v}$ is split into its rotational (non-divergent) part, $\vec{v_\psi}$, and its divergent (irrotational) part, $\vec{v_\chi}$.

$$\begin{aligned} \vec{v} &= \vec{v_\psi} + \vec{v_\chi} && (3.13) \\ \text{with } \vec{v_\psi} &= \vec{k} \times \nabla \psi && (3.14) \\ \text{and } \vec{v_\chi} &= \nabla \chi && (3.15) \end{aligned}$$

Here, ψ denotes the horizontal streamfunction and χ the velocity potential. Hence, the forcing of the mean vorticity by the transient eddy vorticity flux convergence can be written in the following way:

$$\begin{aligned} \frac{\partial \overline{\zeta}}{\partial t} \equiv 0 &= \ldots - \nabla(\overline{\vec{v}'\zeta'}) \ldots && (3.16) \\ &= \ldots - \nabla(\overline{\vec{v_\psi}'\zeta'}) - \nabla(\overline{\vec{v_\chi}'\zeta'}) \ldots && (3.17) \end{aligned}$$

This splitting allows the respective contributions from the transient rotational flow and the transient divergent flow to be compared with the total eddy vorticity flux convergence. It has been shown by Hoskins and Sardeshmukh (1987) that neglecting the second term in Eq. (3.17) leads to errors of about 20% in the estimation of the total transient eddy vorticity flux convergence, $-\nabla(\overline{\vec{v}'\zeta'})$. As can be seen from Eq. (3.12), there are also mean flow contributions to the seasonal mean budget of vorticity. This chapter focusses on the forcing provided by the transient eddies to the seasonal mean vorticity budget.

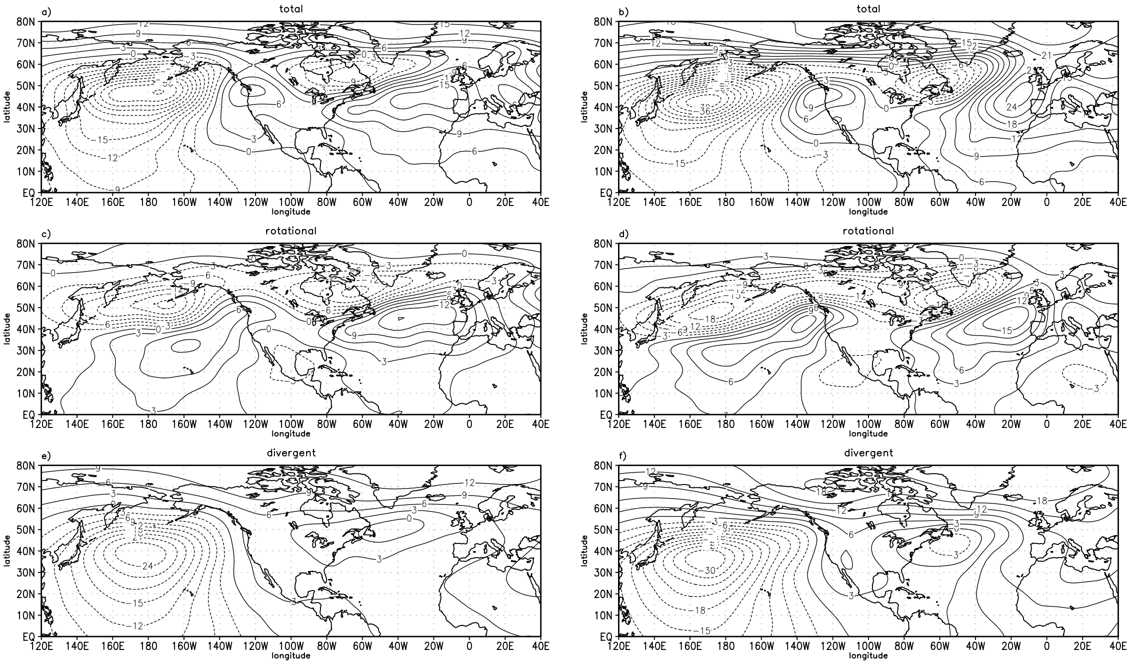

Figure 3.24: *Seasonal (DJF) ensemble mean transient eddy forcing of the mean streamfunction [m^2/s^2] in the bandpass (2.5-6 days) range at 300 hPa as simulated by the CTRLWI (left panels) and CTRLWI42 (right panels) ensembles. In addition to contributions from the total eddy wind field* $-\nabla^{-2}(\nabla(\overline{\vec{v}'\zeta'}))$ *(a,b), contributions from the (c,d) rotational wind field,* $-\nabla^{-2}(\nabla(\overline{\vec{v_\psi}'\zeta'}))$*, and from the (e,f) divergent wind field,* $-\nabla^{-2}(\nabla(\overline{\vec{v_\chi}'\zeta'}))$*, are shown.*

Compared to planetary scales, transient eddy vorticity fluxes tend to exhibit a small-scale structure. It is possible to examine the feedback of the transients onto the mean flow from these fluxes. However, it has been proven to be useful (Hoskins and Sardeshmukh, 1987; Hurrell, 1995) to analyze the eddy-mean flow relationships in terms of the streamfunction, instead of vorticity, in order to emphasize the planetary scales of the eddy forcing. Therefore, based on the relationship $\zeta = \nabla^2\psi$ between vorticity and streamfunction, the inverse Laplacian operator is applied to the terms in Eq. (3.12) to achieve a spatial smoothing of the original fields. Thus, the eddy forcing of the mean streamfunction is analyzed instead of the eddy forcing of the mean vorticity. As in Eq. (3.17), the total eddy forcing of the mean streamfunction can be split into the contributions from the transient rotational and divergent wind components.

$$\frac{\partial\overline{\psi}}{\partial t} \equiv 0 \;=\; \ldots - \nabla^{-2}(\nabla(\overline{\vec{v}'\zeta'}))\ldots \tag{3.18}$$

$$= \; \ldots - \nabla^{-2}(\nabla(\overline{\vec{v_\psi}'\zeta'})) - \nabla^{-2}(\nabla(\overline{\vec{v_\chi}'\zeta'}))\ldots \tag{3.19}$$

One problem discussed by Hurrell (1995) consists in the neglection of the $-\vec{k}\cdot\nabla\times\overline{\omega'\frac{\partial\vec{v}'}{\partial p}}$ term from Eq. (3.12). Neglecting this term is only justified as long as the vorticity equation is considered. On planetary scales, however, Hurrell (1995) found the term to be important and to even offset parts of the streamfunction forcing coming from the tran-

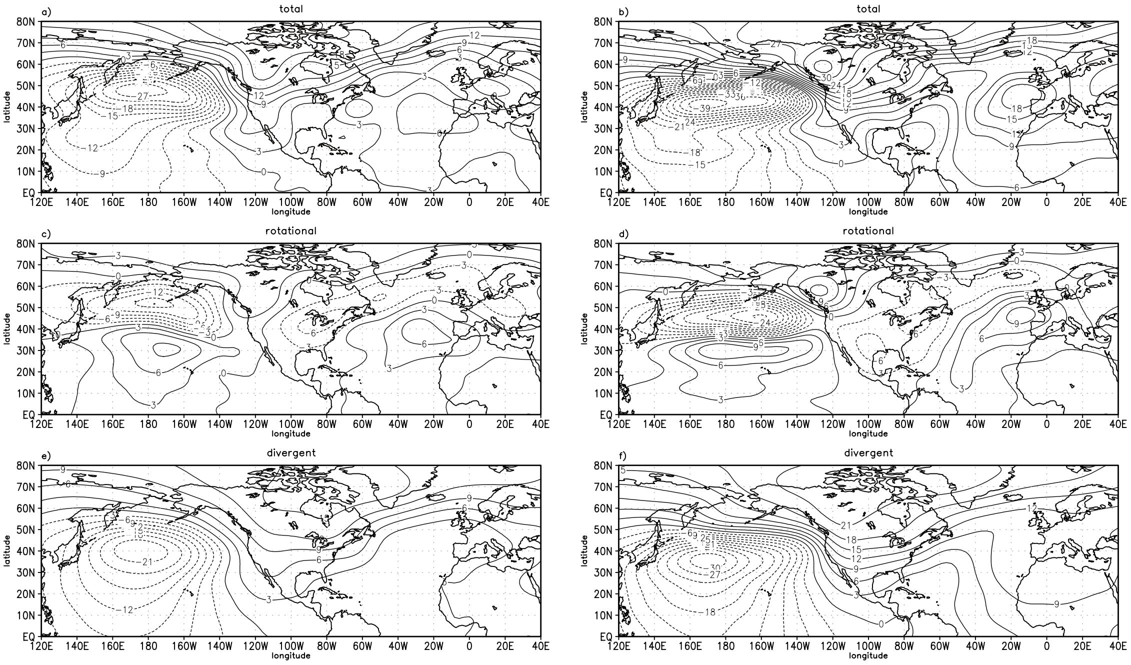

Figure 3.25: *As Fig. 3.24 for the GRWI (left panels) and the GRWI42 (right panels) ensembles.*

sient eddy vorticity flux convergence. Hurrell's (1995) results indicate that on planetary scales, the seasonal mean streamfunction forcing by the eddies is better approximated by the $-\nabla(\overline{\vec{v_\psi}'\zeta'})$ term. This aspect, however, is subject of current investigation.

First, the climatological eddy forcing of the mean streamfunction (EFS hereafter) by the convergence of the transient eddy vorticity fluxes is examined (Eq. 3.18) and split into rotational and divergent parts (Eq. 3.19). The eddy quantities are calculated for each ensemble member and then ensemble-averaged. The seasonal ensemble mean of the EFS terms given in Eq. (3.18) and Eq. (3.19) are shown in Fig. 3.24 for the control ensembles CTRLWI and CTRLWI42. These patterns can be directly compared to the results by Hurrell (1995). Positive (negative) values of the ESF indicate an anticyclonic (cyclonic) forcing of the mean streamfunction by the transient eddies. Over the North Atlantic, the total ESF is dominated by the contributions of the transient eddy rotational wind field. Anticyclonic forcing to the south and cyclonic forcing to the north of the major jet axis and also of the North Atlantic storm track is found both in the total and the rotational eddy vorticity flux convergences (Fig. 3.24 a,c). Over the north western Pacific, however, the cyclonic streamfunction tendency (Fig. 3.24c) is clearly enhanced by the corresponding tendency in the divergent wind component (Fig. 3.24e). Furthermore, the latter largely offsets the cyclonic tendency evident over subtropical latitudes in the rotational contribution, leading to a net large-scale cyclonic tendency of the mean streamfunction over most parts of the North Pacific. Similar climatological patterns are simulated at T42 resolution (Fig. 3.24, right panels) but with much higher amplitudes and a stronger tilt in the zero line of the streamfunction tendency across the North Atlantic compared to the T106 patterns. These numbers indicate that the transient eddies would, if acting alone,

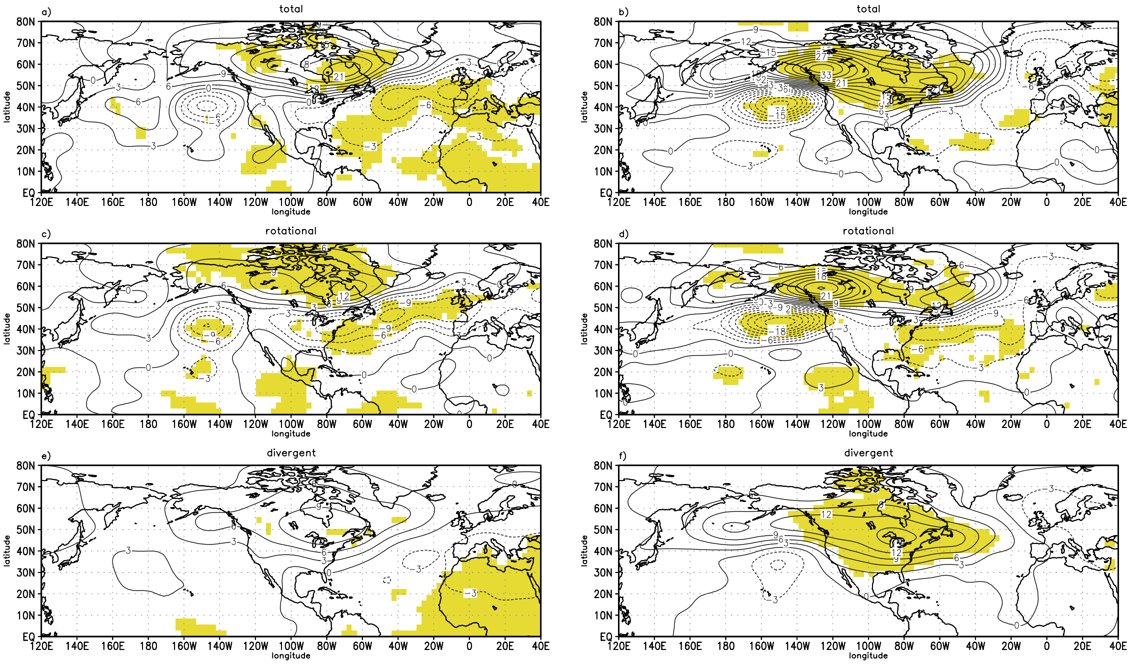

Figure 3.26: *Seasonal (DJF) ensemble mean response of the eddy forcing of the mean streamfunction [m^2/s^2] in the bandpass (2.5-6 days) range at 300 hPa as simulated by the GRWI (left) and GRWI42 (right) ensemble. Results are shown for the total (a,b), rotational (c,d) and divergent (e,f) wind fields. Shading denotes significance at the 95% level according to a Mann-Whitney-Wilcoxon-u-test.*

spin up streamfunction amplitudes of $\approx 5 \cdot 10^6\ m^2/s$ within a few days based on an EFS of 20 m^2/s^2.

The extent to which the the eddy contributions to the seasonal mean streamfunction budget respond to ENSO is now examined. The $-\nabla^{-2}(\nabla(\overline{\vec{v}'\zeta'}))$ terms as calculated for the two global regression experiments (GRWI, GRWI42) are shown in Fig. 3.25. They largely confirm the above findings regarding the climatological patterns shown in Fig. 3.24. The amplitudes of the ESF terms in the T42 experiment are again higher than at T106 resolution. In addition, the contribution of the transient divergent flow simulated in GRWI42 (Fig. 3.25f) is seen to be considerable over the North American continent and over the central North Pacific. To further illustrate the ENSO-related changes, the ensemble mean response as simulated by GRWI and GRWI42 is shown in Fig. 3.26. Here, the significance of the response is estimated with the Mann-Whitney-Wilcoxon u-test (Sachs, 1992), since it cannot be assumed a priori that the different realizations of the EFS within an ensemble follow a normal distribution.
The strongest response is reached in the GRWI42 experiment over the North Pacific and the North American continent. Especially in the GRWI42 transient divergent flow (Fig. 3.26f), a strong response is simulated with a stronger cyclonic tendency over the North American continent. The transient rotational flow also exhibits a substantial response over the North American continent and the eastern North Pacific. In contrast, no signifi-

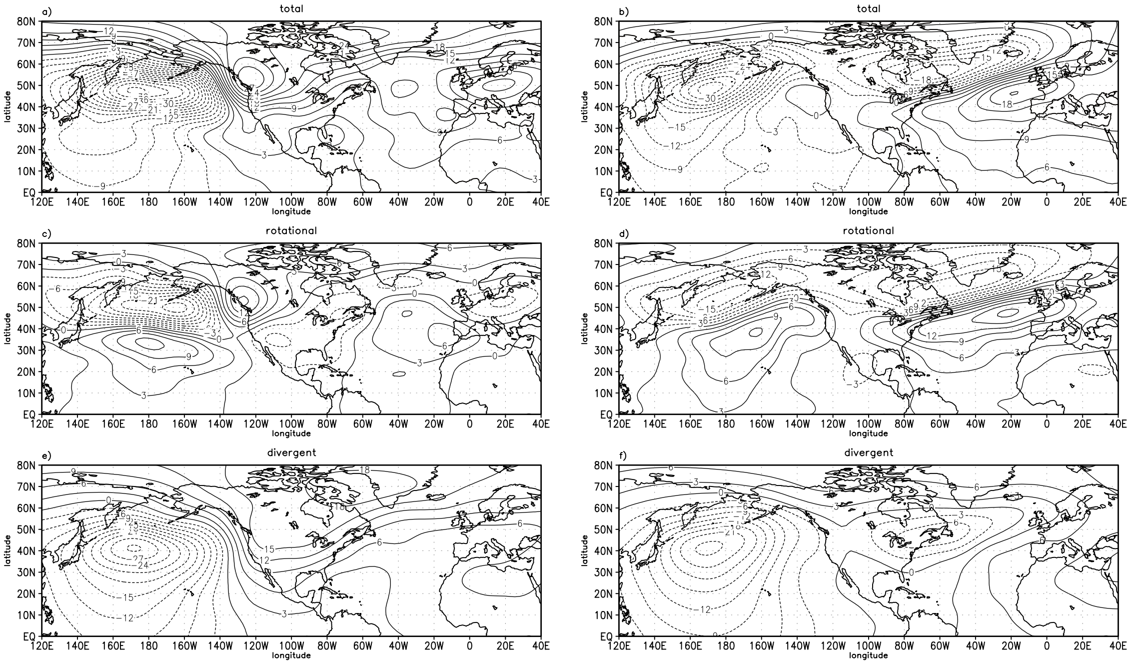

Figure 3.27: *As Fig. 3.24 for the TRWI (left panels) and the NTRWI (right panels) ensemble.*

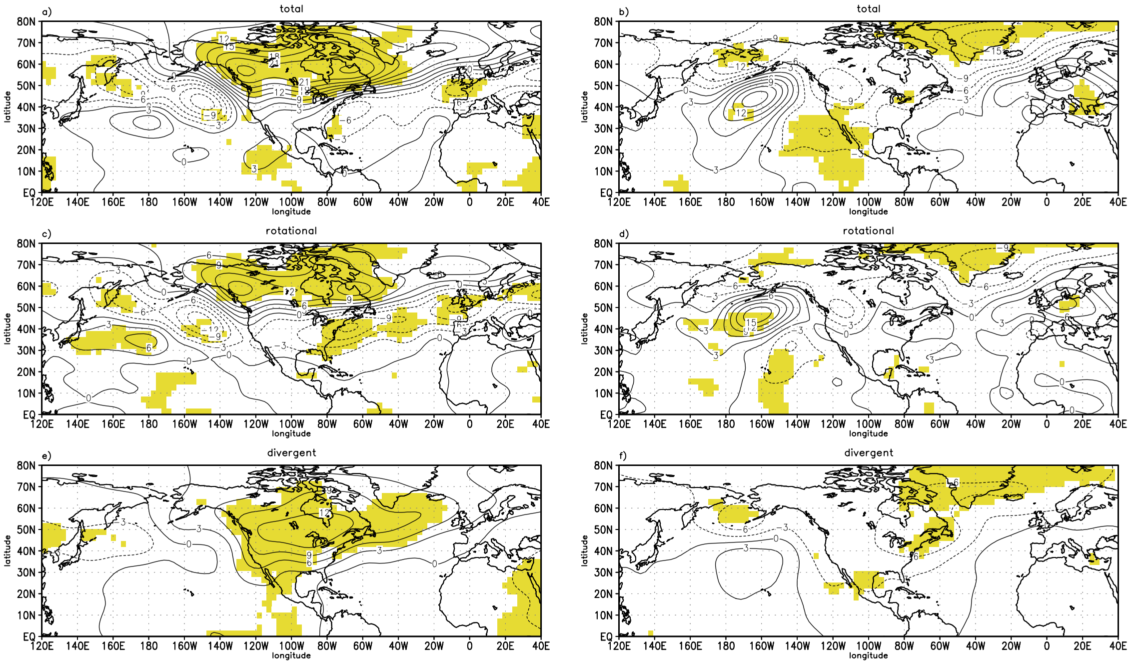

Figure 3.28: *As Fig. 3.26 for the TRWI (left panels) and NTRWI (right panels) ensemble.*

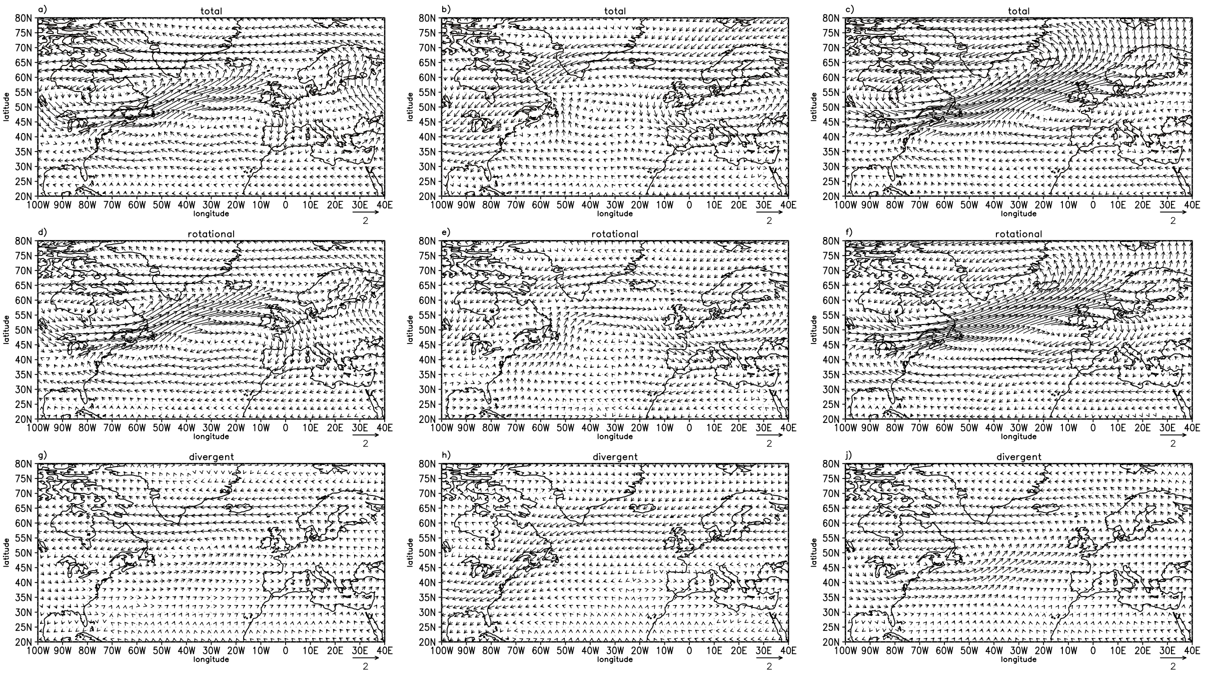

Figure 3.29: *Seasonal (DJF) ensemble mean transient eddy forcing [m/s^2] of the mean rotational flow, $\overline{\vec{v_\psi}}$, in the bandpass (2.5-6 days) range at 300 hPa for the CTRLWI (left panels), TRWI (middle), and NTRWI (right panels) ensemble, according to Eq. (3.21). Results are shown for the total (a-c), rotational (d-f) and divergent (g-j) wind fields.*

cant changes are simulated for the divergent contribution at T106 resolution (Fig. 3.26 c). In the GRWI experiment, the response structure can be approximated by the rotational eddy flow. In addition, the significant response simulated at T106 resolution covers larger areas of the North Atlantic sector compared to the T42 experiment. Thus, the present analysis further confirms that the response behaviour of the transient eddies on synoptic timescales in the North Atlantic/European sector and thus their feedback onto the mean flow (streamfunction) is clearly resolution dependent.

Next, the EFS is investigated with respect to its symmetry according to the sign of the imposed SST forcing. The seasonal ensemble mean EFS patterns as simulated by the TRWI and NTRWI ensembles are shown in Fig. 3.27 and their respective response patterns in Fig. 3.28. The total ESF response simulated by the tropical Pacific regression-only experiment (TRWI) shows significant changes from the eastern North Pacific region extending over the North American continent into the North Atlantic/European sector (Fig. 3.28a). A strong structural similarity between the total and the rotational response north of 40°N is evident. However, the significant cyclonic forcing from the divergent component (Fig. 3.28e) over North America and the North Atlantic partially offsets the anticyclonic forcing south of 50°N. As is evident from Fig. 3.28 (right panels), the significant changes in the streamfunction forcing under La Niña conditions are restricted to the North Pacific region. The NTRWI response generally indicates a subordinate role of the

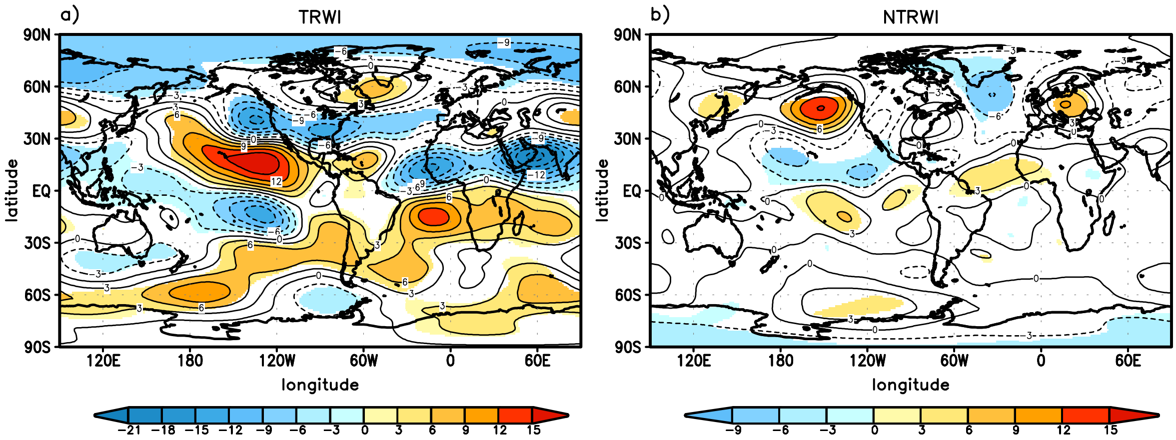

Figure 3.30: *Seasonal (DJF) ensemble mean response of the 300 hPa streamfunction* [$10^6 m^2/s$] *as simulated by the a) TRWI, and b) NTRWI experiment. Zonal averages have been removed. Color denotes significance at the 95% level according to a t-test.*

transient eddies in forcing the seasonal mean ψ300 anomalies. Furthermore, this supports the notion that both the stationary waves and the mean flow itself play a major role in determining the ENSO response over the North Atlantic/European sector.

So far, the eddy forcing onto the mean rotational flow has been considered in terms of the streamfunction forcing. This eddy feedback onto the mean flow can be further interpreted.

$$\left(\frac{\partial\overline{\psi}}{\partial t}\right)_{eddies} = \mathcal{S} \tag{3.20}$$

$$\left(\frac{\partial\overline{\vec{v_\psi}}}{\partial t}\right)_{eddies} = \vec{k}\times\nabla\mathcal{S} = \left(-\frac{\partial\mathcal{S}}{\partial y},\frac{\partial\mathcal{S}}{\partial x}\right) \tag{3.21}$$

Given a term $\mathcal{S}$ contributes to the eddy forcing of the seasonal mean streamfunction and using Eq. (3.14), $\mathcal{S}$ can also be used to determine the forcing of the mean rotational flow, $\overline{\vec{v_\psi}}$ (Eq. 3.21). The vector fields resulting from applying Eq. (3.21) onto the ESF terms shown in the previous figures are presented in Fig. 3.29 for the CTRLWI, TRWI, and NTRWI ensembles for the North Atlantic sector. The resulting vector fields emphasize the eddy forcing onto the mean rotational flow. Again, a distinction is made between the different contributions from the total, rotational and divergent transient flow components. Under climatological conditions (Fig. 3.29, left panels), the eddies induce a westerly forcing onto the mean flow as is known from earlier studies (Palmer and Mansfield, 1986). This forcing is mainly provided by the transient eddy rotational flow (Fig. 3.29d). Under El Niño conditions, the eddy contributions to the forcing of the rotational mean flow change considerably in magnitude and direction, as can be seen from Fig. 3.29 (middle panels). In particular, the rotational component of the eddy forcing is weakened (Fig. 3.29e) over the central North Atlantic which favors a weakened jet stream. Furthermore, the divergent component (Fig. 3.29h) provides an important contribution

			TRWI			**NTRWI**		
		wind field part	**unfilt.**	**bandp.**	**lowp.**	**unfilt.**	**bandp.**	**lowp.**
N.-Hemi.	0°N-90°N	total	0.17	0.29	0.06	0.18	0.27	0.06
		rot.	0.22	0.31	0.15	0.22	0.37	0.12
		div.	-0.03	0.17	-0.13	0.04	0.06	-0.09
Extratrop. Northern Hemisphere	120°E-40°E 20°N-80°N	total	0.49	0.38	0.36	0.19	0.31	-0.00
		rot.	0.46	0.51	0.35	0.25	0.44	0.09
		div.	0.22	0.10	0.20	-0.01	0.06	-0.18
North Pacific	135°E-135°W 20°N-80°N	total	0.33	0.20	0.33	0.23	0.05	0.42
		rot.	0.34	0.33	0.29	0.53	0.43	0.62
		div.	0.12	-0.14	0.24	-0.36	-0.49	-0.21
PNA	180°W-80°W 20°N-80°N	total	0.47	0.16	0.47	0.22	0.32	0.01
		rot.	0.57	0.35	0.54	0.27	0.50	0.11
		div.	0.07	-0.07	0.17	-0.03	-0.02	-0.21
North America	120°W-60°W 20°N-80°N	total	0.74	0.47	0.59	-0.11	0.63	-0.48
		rot.	0.83	0.74	0.66	-0.37	0.57	-0.48
		div.	0.39	0.13	0.27	0.45	0.50	-0.17
North Atlantic/ Europe	80°W-20°E 20°N-80°N	total	0.65	0.80	0.41	0.44	0.47	0.09
		rot.	0.49	0.81	0.38	0.32	0.45	0.02
		div.	0.43	0.48	0.20	0.37	0.35	0.24

Table 3.4: *Pattern correlations between the seasonal ensemble mean response of the eddy streamfunction forcing in the different frequency bands and the seasonal ensemble mean $\psi300$ response.*

to the northeasterly forcing found in the total transient eddy forcing of the mean flow (Fig. 3.29b) over the eastern North American continent and the Labrador Sea. In the La Niña experiment (Fig. 3.29, right panels), a striking similarity to the CTRLWI vector field is simulated, but with larger magnitudes of the vectors. The intense southwesterly forcing across the North Atlantic (Fig. 3.29 c,f) is partially intensified by the divergent component (Fig. 3.29j) which, between 35°N and about 50°N, exhibits larger magnitudes than the eddy rotational forcing component.

The response in the ESF terms under El Niño (La Niña) conditions is now related to the seasonal mean El Niño (La Niña) response of the 300 hPa streamfunction ($\psi300$) itself. The seasonal mean responses of $\psi300$ as simulated by the TRWI and NTRWI ensembles are shown in Fig. 3.30. Using the streamfunction instead of geopotential emphasizes zonal anomalies of the flow (James, 1994). In Fig. 3.30a, the Northern Hemisphere tropical and subtropical Pacific show an anticyclonic streamfunction response, with cyclonic anomalies ($\psi300_{anom} < 0$) to the north and south of it. A significant band of cyclonic anomalies extends across the North Atlantic into Europe. This may be responsible for the weakening of the North Atlantic jet stream near 45°N that has been discussed above (Fig. 3.3). In the La Niña experiment (NTRWI, Fig. 3.30 b), the response is much weaker and exhibits a wavelike structure over the Pacific, with the wave train spanning large parts of the midlatitudes. Note that this figure underlines again the strong deviations from pure

		TRWI			**NTRWI**		
		unfilt.	**bandp.**	**lowp.**	**unfilt.**	**bandp.**	**lowp.**
N. Hemisphere	0°N-90°N	-0.34	-0.33	-0.10	-0.17	-0.25	0.08
extratrop. N.-Hemi.	120°E-40°E 20°N-80°N	-0.40	-0.39	-0.13	-0.19	-0.31	0.11
North Pacific	135°E-135°W 20°N-80°N	-0.49	-0.30	-0.31	-0.16	-0.44	0.02
PNA	180°W-80°W 20°N-80°N	-0.54	-0.42	-0.29	-0.02	-0.31	0.26
North America	120°W-60°W 20°N-80°N	-0.44	-0.48	0.19	-0.05	-0.21	0.21
N. Atlantic/Europe	80°W-20°E 20°N-80°N	-0.32	-0.39	0.01	-0.35	-0.33	-0.05

Table 3.5: *Pattern correlations between the seasonal ensemble mean response of the eddy temperature forcing in the different frequency bands and the seasonal ensemble mean T850 response.*

antisymmetry between El Niño and La Niña conditions.

As stated above, the response of the $-\nabla^{-2}(\nabla(\overline{\vec{v}'\zeta'}))$ terms can be interpreted in such a way that the eddies contribute to the seasonal mean streamfunction response.

Pattern correlations are calculated between the corresponding patterns shown in Fig. 3.28 and Fig. 3.30. Results are given in Table 3.4 for selected regions. For completeness, results from the unfiltered and the lowpass-filtered daily data have been included. Positive pattern correlations indicate that the eddies feed back positively onto the mean flow response. It can be clearly seen from Table 3.4 that the feedback of the eddies is a regionally confined process. When the entire Northern Hemisphere is considered, only small correlations are found. The same holds for the extratropics. Strong correlations are found for the North American continent and the North Atlantic/European sector. This indicates that the transient eddies reinforce the mean flow streamfunction response only in these regions. Furthermore, the contribution of the eddy rotational component generally dominates. While in the TRWI experiment, a clear reinforcement of the mean streamfunction response by the eddies can be found in all frequency bands over North America, the NTRWI correlations are generally lower and in some regions even counteract the streamfunction mean response. In the TRWI experiment, strongest correlations are found in the bandpass range over the North Atlantic/European sector, indicating an important role of the transient eddies in establishing the mean response. In the La Niña experiment, correlations are strongest over the North American continent. Apart from a few exceptions, the overall tendency of the eddy feedback is to reinforce the mean flow anomalies.

b) Temperature forcing

So far, the interaction of mean flow and transient eddies has only been discussed for the upper troposphere, where barotropic processes are dominant. Trenberth and Hurrell (1994), when performing a similar analysis, have shown the transient eddy forcing of the

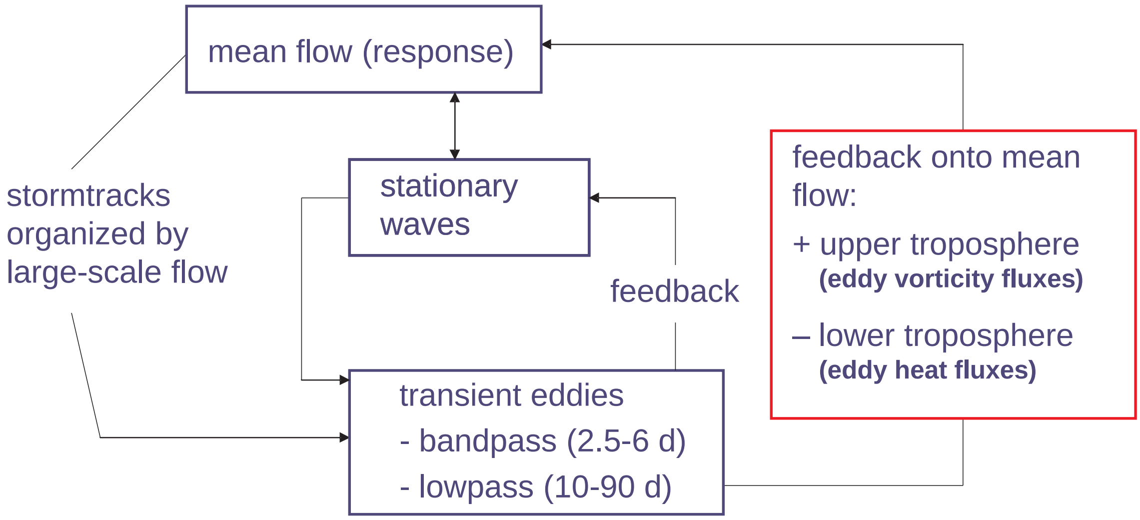

Figure 3.31: *Schematic to illustrate the role of transient eddies in determining the atmospheric ENSO response.*

mean streamfunction at lower tropospheric levels to be much smaller than the baroclinic component. Furthermore, it has been shown from climatological studies (e.g. Blackmon et al., 1977) that transient eddies tend to destroy the mean baroclinicity by weakening the meridional temperature gradient, especially in the beginning of their life cycle. Therefore, it is now examined how this feedback changes under ENSO conditions.

Based on the prognostic temperature equation, the eddy contribution to the seasonal mean temperature budget can be described as follows.

$$\frac{\partial \overline{T}}{\partial t} \equiv 0 = -\overline{\vec{v}} \cdot \nabla \overline{T} - \overline{\omega}\frac{\partial \overline{T}}{\partial p} - \nabla \cdot (\overline{\vec{v}'T'}) - \frac{\partial}{\partial p}\overline{\omega' T'} \tag{3.22}$$

The mean temperature, $\overline{T}$, is influenced by the convergence of the transient eddy heat fluxes, $-\nabla \cdot (\overline{\vec{v}'T'})$, and $\frac{\partial}{\partial p}\overline{\omega' T'}$. The latter term is not considered here. In analogy to the streamfunction analysis, the seasonal mean El Niño (La Niña) response in the eddy temperature forcing, $-\nabla \cdot (\overline{\vec{v}'T'})$, is related to the seasonal mean El Niño (La Niña) temperature response at the 850 hPa level. Results are summarized in Table 3.5. In order to keep the discussion concise, no distinction is made between the different wind field parts of the eddy flow. In most considered domains, the overall tendency of the eddy forcing response opposes the mean temperature response which is consistent with the climatological picture. However, the generally negative pattern correlations are weaker than those in the streamfunction analysis.

c) Summary of the eddy feedback

From all the above findings on the mean flow response, the eddy response and the feedbacks between both, a schematic picture can be derived (Fig. 3.31). This schematic is not intended to represent a simple cause-and-effect chain. It just illustrates that different processes establish the ENSO response.

The mean flow response is always associated with changes in the stationary waves, and these influence the structure and the energetics of transient eddies (see Saltzman, 1963). Cai and Mak (1990) report the mutual dependence of high- and low-frequency components of the circulation. According to their results, planetary waves gain energy from synoptic-scale waves. On the other hand, planetary-scale waves can provide the background for synoptic-scale eddies to develop. In addition, Branstator (1995) has shown that large-scale and low-frequency flow anomalies can organize the storm track anomalies in such a way that a positive feedback of the momentum fluxes onto these large-scale anomalies is induced. This positive feedback of the transient eddies onto the mean flow ENSO response has become evident from our energetic and streamfunction forcing analysis at upper tropospheric levels. On the other hand, the negative feedback of the eddy heat fluxes onto the mean temperature response has also been shown. A complete picture can only be drawn from a fully 3-dimensional analysis in order to separate the different processes from each other. This, however, would require a linearized version of the ECHAM model to render possible experiments in the style of Held et al. (1989) where the relative roles of transient eddy heat and vorticity fluxes are examined.

3.4 ENSO teleconnections and climate change

In the preceding parts of this chapter, several aspects of the ENSO impact on the atmosphere have been discussed, thereby focussing on present climate conditions. However, there exists consensus within large parts of the scientific community that a major climate change has to be expected by the end of this century due to continuing anthropogenic greenhouse gas emissions (Mitchell and Karoly, 2001). In such a greenhouse scenario, both the frequency of the occurrence of El Niño and La Niña events and their amplitudes can be considerably altered (Timmermann et al., 1999). Thus, the question may be raised to which extent ENSO teleconnections are affected by climate change.

3.4.1 Future climate experiments

On the basis of seasonal ensemble experiments, it is examined whether the atmospheric response to ENSO is changed under future climate conditions. These experiments are performed in complete analogy to the present climate experiments listed in Table 2.2. Each ensemble consists of five members and is integrated over 120 days where only the last 90 days are retained (DJF). The ensemble members only differ with respect to their initial conditions.

The major difference to the experiments presented above consists in the underlying climatological SST forcing. The experiments discussed here are forced by climatological SST corresponding to future climate conditions. This “future climatological” SST has been derived from a transient climate change simulation with the coupled ECHAM4(T42)/OPYC3 model (Roeckner et al., 1998). The 240 year-integration covers the period 1860-2100. During the years 1860-1990, the observed annual concentrations of greenhouse gases (CO_2, CH_4, N_2O) and several industrial gases (chlorofluorocarbons, hydrochlorofluorocarbons, etc.) are prescribed. From 1990 onward, concentrations are prescribed according to the IPCC scenario IS92a (IPCC, 1992). More details on this simulation can be found in Roeckner et al. (1998).

The climatological boundary forcing for the “scenario experiments” has been extracted from the ECHAM4/OPYC3 simulation as follows. In the original ECHAM4/OPYC3 simulation, the concentrations for the year 2075 correspond to an effective doubling of CO_2. Therefore, the 20-year period centered at year 2075, i.e. 2065-2084, has been chosen to calculate an average annual cycle of SST (“future climatological SST”). This future climatological SST is prescribed as a lower boundary condition in the scenario control ensemble experiment (CTRLWI_SCEN in Table 3.6). In analogy to the TRWI experiment, an El Niño scenario experiment (TRWI_SCEN) is performed by superimposing the tropical Pacific part of the enhanced regression pattern shown in Fig. 2.3b. The enhanced CO_2, CH_4, and N_2O concentrations of year 2075 are used in these experiments.

As is shown in Fig. 3.32, several quantities respond strongly to the replacement of present

Seasonal ensemble experiments with ECHAM4/T106
under future climate conditions (DJF)

	Experiment	**SST forcing**
present climate	CTRLWI	present climatology
	TRWI	present climatology plus regression pattern in the tropical Pacific
future climate	CTRLWI_SCEN	future climatology
	TRWI_SCEN	future climatology plus regression pattern in the tropical Pacific

Table 3.6: *Future climate seasonal ensemble experiments with ECHAM4/T106. See text for details on the construction of the future climatological SST. To illustrate the analogy to the present-day experiments, they have been included into the table.*

climatological SST by the future climatological SST. Fig. 3.32 illustrates that largest temperature changes are simulated in the Northern Hemisphere (Fig. 3.32 c,d). Associated with the overall warming, the 500 hPa geopotential height (Fig. 3.32e) increases globally, thereby affecting the upper-tropospheric wind field (Fig. 3.32f). Interestingly, the SLP changes in the North Atlantic sector indicating a weakening of the meridional pressure gradient are in clear contrast to earlier findings (Knippertz et al., 2000; May, 2001) of an intensification of the North Atlantic Oscillation. The precipitation changes simulated by CTRLWI_SCEN (Fig. 3.32b) are largely comparable to the results by Voss et al. (2002) (their Fig. 6). They also find, for example, a decrease in precipitation over northeastern South America. Additionally, precipitation increases under future climatological conditions over most parts of the boreal oceans. Substantial temperature increases in the tropical Pacific and associated modifications of the major convective activity over the tropical Pacific are evident from Fig. 3.32 b,d.

3.4.2 ENSO impact under greenhouse conditions

It has been demonstrated in the previous section that considerable changes in the atmosphere are simulated by ECHAM4 in response to greenhouse warming. Since also the tropical Pacific is affected, it is now examined whether the ENSO impact on the atmosphere is altered compared to that discussed in ch. 3.1. An earlier finding in this thesis (ch. 3.1) was the dominant role of the tropical Pacific in determining the ENSO response. Therefore, the future El Niño experiment (TRWI_SCEN) has been performed in analogy to the TRWI experiment.

The atmospheric response is shown in Fig. 3.33. A comparison of Fig. 3.33 to the corresponding TRWI response under present climate conditions (Fig. 3.3 b,f) reveals a striking similarity between the two simulated response patterns. The TRWI_SCEN experiment also exhibits a Southern Oscillation-type structure over the tropical Pacific. Furthermore, the weakening of the meridional pressure gradient over the North Atlantic sector found

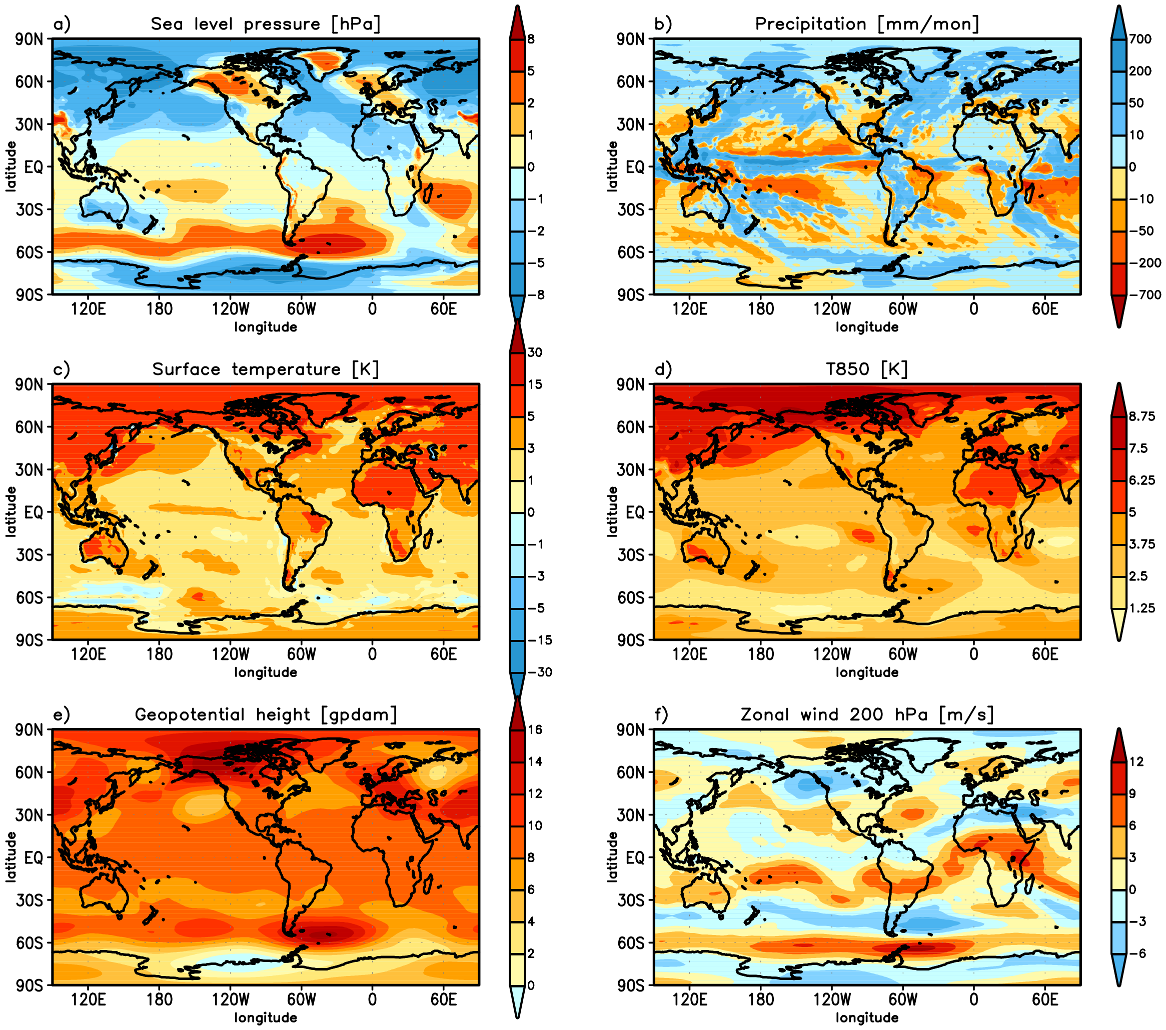

Figure 3.32: *Difference between the seasonal (DJF) ensemble means simulated by the CTRLWI_SCEN and CTRLWI ensembles for a) SLP [hPa], b) precipitation [mm/mon], c) surface temperature [K], d) T850 [K], e) 500 hPa geopotential height [gpdam], and f) 200 hPa zonal wind [m/s]. The colorbars indicate the contour intervals.*

in TRWI (Fig. 3.3f) is also reproduced by the TRWI_SCEN experiment. Over the Indian ocean, a slightly weaker response is simulated by TRWI_SCEN. The overall similarity between the TRWI and TRWI_SCEN responses is also evident in the upper-tropospheric wind field (u200), with the wavelike structure out of the tropical Pacific region. Furthermore, as in TRWI, a significant band of reduced zonal wind spans the North Atlantic.

The TRWI_SCEN response over Europe is displayed in Fig. 3.34. The SLP response simulated over Europe (Fig. 3.34a) largely resembles the responses simulated by the present climate GRWI and TRWI experiments, but the eastward extension into central Europe is less pronounced, with a more meridional orientation of the contour lines. Only small regions exhibit a significant change in the 850 hPa temperature field (Fig. 3.34b),

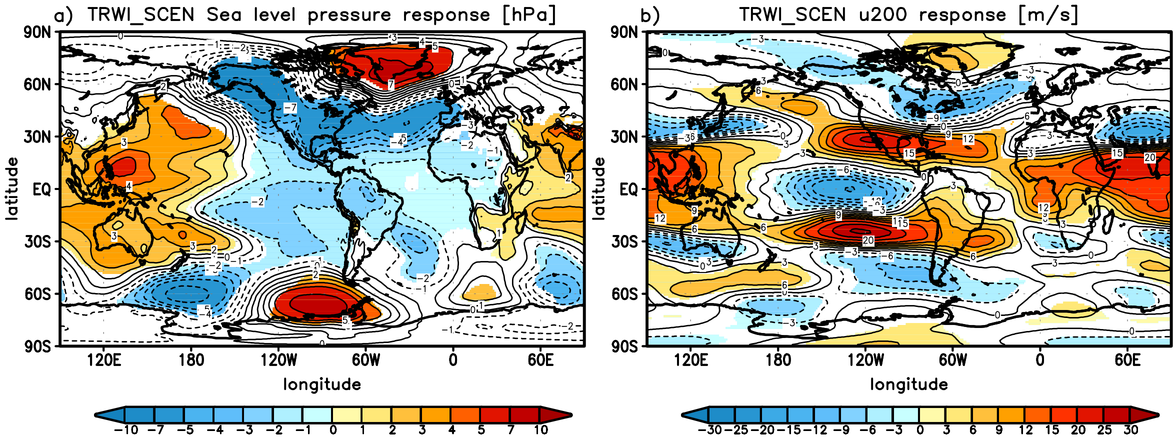

Figure 3.33: *Seasonal (DJF) ensemble mean response in the tropical Pacific regression experiment under future climate conditions (TRWI_SCEN) for a) SLP [hPa] and b) 200 hPa zonal wind [m/s]. Color denotes significance at the 95% level according to a t-test. The colorbar indicates the irregular contour interval.*

but western Europe experiences significant positive precipitation anomalies (Fig. 3.34c). A major modification can be found over the eastern Mediterranean. In this region, no significant precipitation response is simulated by the TRWI_SCEN experiment, while precipitation is significantly decreased in the present climate El Niño experiments.

The eddy response to El Niño with underlying future climatology is also analyzed. Results confirm the overall similarity between the responses simulated by TRWI_SCEN and TRWI. As an example, the synoptic-scale variability changes in response to El Niño. Storm track activity at the 500 hPa level $(\sqrt{\overline{z_{bp}'^2}})$ is weakened over the central North Atlantic (not shown) and bears a close resemblance to the southward shift of the storm track simulated by TRWI (Fig. 3.15a).

To conclude, it can be stated that the ENSO response simulated in the scenario experiments is rather similar to the response under present climate conditions. In particular, it should be emphasized that the significant remote impact on the North Atlantic/European sector appears to be a stable phenomenon despite the differing climatologies.

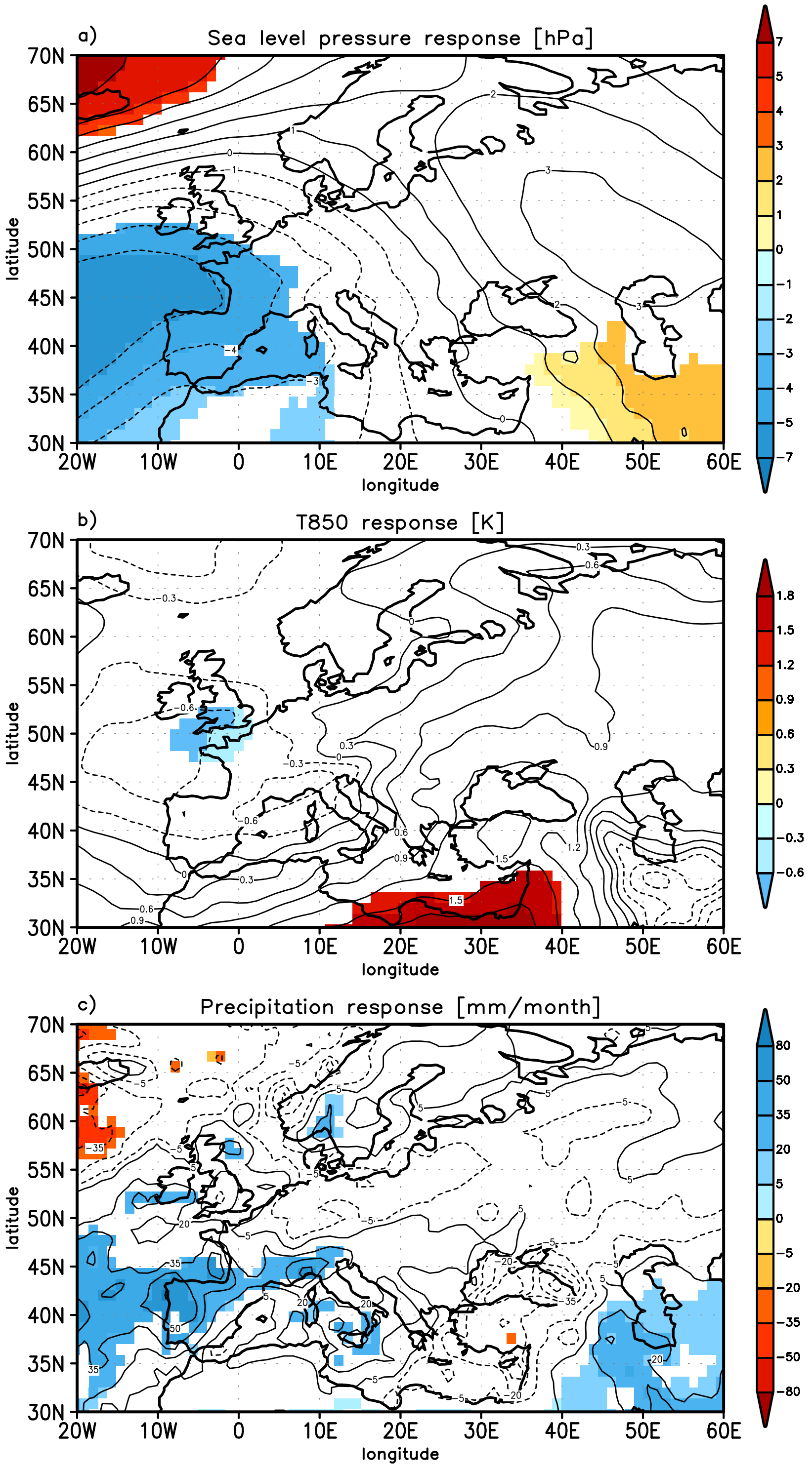

Figure 3.34: *Seasonal (DJF) ensemble mean response over Europe in the tropical Pacific regression experiment under future climate conditions (TRWI_SCEN) for a) SLP [hPa], b) T850 [K], and c) precipitation [mm/mon]. Color denotes significance at the 95% level according to a t-test. The colorbar indicates the irregular contour interval.*

4 ENSO and tropical cyclones

Tropical cyclones are among the most devastating weather phenomena. Being associated with strong winds and heavy precipitation, tropical cyclones like Atlantic hurricanes or typhoons in the Indo-Pacific region can cause substantial economic damages of the order of billions of U.S. dollars. Tropical cyclones can be classified according to their intensity (Table 4.1).

category name	**maximum sustained surface wind speed** v_s	**Saffir-Simpson scale**
tropical storms	$17 \leq v_s \leq 33\ ms^{-1}$	—
hurricanes (typhoons)	$v_s \geq 33\ ms^{-1}$	1-2
major hurricanes (major typhoons)	$v_s \geq 50\ ms^{-1}$	3-5

Table 4.1: *Classification of tropical cyclones according to their intensity as given by the maximum sustained wind speed during a part of their life cycle.*

A fundamental observational study on the characteristics of Atlantic hurricanes has been published by Gray (1979). Most aspects, however, are also valid for tropical cyclones in other geographical regions. A primary criterion for hurricane development is that sea surface temperatures exceed the threshold of 26°C. However, this is not a sufficient condition, as seen in the South Atlantic, where no hurricanes occur. Gray (1979) defined a “seasonal genesis parameter” based on the following physical parameters: a) the Coriolis parameter f (hurricanes can only occur on a rotating earth and in regions with f being large enough to provide the necessary convergence), b) the relative vorticity, c) the inverse of the vertical wind shear (strong vertical shear is detrimental to hurricane development), d) the upper ocean thermal energy, e) the relative humidity in the lower and middle troposphere, and f) the moist static stability. These parameters are chosen since hurricanes only develop in regions with large-scale convergence in the lower troposphere, with moisture convergence being the crucial element.

In a review paper by Emanuel (1991), existing theories on the hurricane development are compared. The inconsistencies of the CISK theory (Conditional Instability of the Second Kind) with observations are demonstrated. A major source of inconsistency is the observation that hurricanes only develop over open oceans in the presence of sea surface temperatures larger than 26°C. Therefore, air-sea interaction is favored as a source of potential energy (Emanuel, 1991) due to the thermodynamic disequilibrium between the atmosphere and the underlying ocean. In this case, the positive feedback leading to the intensification of the cyclone consists in the following. Increased moisture transfer from the ocean leads to saturation of the boundary layer and increased convection. This effect further strengthens the surface winds, thereby reinforcing the evaporation from the ocean. Hurricanes often develop from preexisting large-scale disturbances (e.g. easterly waves). But it is still not well understood why such a development often does not occur in spite of favorable conditions.

The number of tropical cyclones exhibits considerable variations on interannual and even on interdecadal timescales, both in the Atlantic sector and in the western North Pacific. These low-frequency fluctuations have been discussed in several observational (Gray, 1984; Landsea, 2000; Yumoto and Matsuura, 2001) and modelling studies (Wu and Lau, 1992; Vitart and Anderson, 2001; Yumoto et al., 2001). These results suggest an influence of the ENSO phenomenon on Atlantic hurricanes with a reduced (increased) number during an El Niño (La Niña) event. ENSO has also been shown to have an impact on the location of tropical cyclone genesis in the western North Pacific (Matsuura et al., 1999). The stratospheric Quasi-Biennial Oscillation has been suggested as a possible reason for low-frequency variations in tropical cyclone activity (Gray, 1984).

In the present chapter, the general ability of the ECHAM4/T106 model (as described in ch. 2) to simulate tropical storms is investigated based on a 20-year AMIP-type (Atmospheric Model Intercomparison Project) integration covering the years 1979-1998. The observed history of monthly sea surface temperatures taken from the HadISST dataset (Rayner et al., 2002) is prescribed, and the skill of the model in simulating the observed changes in tropical storm activity is investigated. Finally, some comments are made about large-scale circulation anomalies in the light of tropical storm formation.

4.1 Representation of tropical cyclones in ECHAM4

In the present section, the AMIP experiment with the ECHAM4/T106 model forced by observed SST of 1979-1998 is used to evaluate the general ability of the ECHAM4 model to simulate tropical cyclones. First modelling results have been presented by Manabe et al. (1970) from a low-resolution AGCM integration. They showed the ability of their AGCM to simulate tropical cyclones with a structure comparable to observations. Later studies present evidence for the simulation of hurricane-like vortices in high-resolution AGCM experiments. In a T106 simulation with the ECHAM3 AGCM, Bengtsson et al. (1995) were quite successful in reproducing the observed structure, and seasonal and geographical distributions of tropical cyclones. Furthermore, May (2000) investigated the

Check criteria for the detection of tropical storms in T106 datasets			
	Bengtsson et al. (1995)	Walsh (1997)	May (2000)
relative vorticity at 850 hPa	$> 3.5 \cdot 10^{-5} s^{-1}$	$> 3.5 \cdot 10^{-5} s^{-1}$	$> 11 \cdot 10^{-6} s^{-1}$
minim. wind speed at 10 m	$> 15\ ms^{-1}$	$> 14\ ms^{-1}$	$> 14\ ms^{-1}$
minimum surface pressure	within 7 × 7 grid point area around grid point fulfilling vorticity criterion	closed pressure minimum around grid point fulfilling vorticity criterion	closed pressure minimum around grid point fulfilling vorticity criterion
sum of troposph. temp. anomalies (300 hPa, 500 hPa, 700 hPa)	$> 3°$C within 7 × 7 grid point area	$> 2°$C within 5 × 27 grid point area	$> 2°$C within 5 × 27 grid point area
vertical temperature structure	$T_{a,300} > T_{a,850}$	$T_{a,300} > T_{a,850}$	$T_{a,300} > T_{a,850}$
vertical structure of wind field around storm center	$\|v_{850}\| > \|v_{300}\|$	$\|v_{850}\| > \|v_{300}\|$	$\|v_{850}\| > \|v_{300}\|$
minimum duration of event	$\geq$ 1.5 days	—	$\geq$ 1.5 days

Table 4.2: *Tropical storms detection criteria as defined by Bengtsson et al. (1995). These criteria are applied to the output of the 20-year ECHAM4/T106 simulation described in the text. For comparison, criteria as used in other studies are included into the table.*

performance of the ECHAM4 model from time slice experiments focussing on a comparison of tropical cyclone activity under present and future climate conditions.

For the purpose of this study, the objective detection algorithm developed by Bengtsson et al. (1995) is used with the threshold values listed in Table 4.2. The criteria used in the studies by Walsh (1997) and May (2000) have been included into the table. These criteria seek to capture the fundamental properties of tropical cyclones. Compared to the structure and intensity of observed systems, it is necessary to adapt the search criteria to the horizontal resolution of the model. As can be seen from Table 4.2, a simulated vortex has to fulfill several criteria to be classified as a tropical cyclone. A priori, the search is restricted to ocean grid points. At first, the relative vorticity has to exceed the threshold value of $3.5 \cdot 10^{-5} s^{-1}$ at the 850 hPa level. Within an area of 7×7 grid points around this vorticity maximum, a minimum surface pressure and wind speeds of more than 15 ms^{-1} have to be detected. This is clearly a weakened condition compared to the observed maximum tangential wind speeds (see Table 4.1). In order to account for the warm core structure of a tropical cyclone (i.e. $\frac{\partial T}{\partial r} < 0$ with r denoting the radial distance from the center), the sum of tropospheric temperature anomalies at different levels has to exceed 3°C within the 7×7 grid point area. Thus, the substantial temperature decrease of up to 10°C within a distance of 30-200 km from the center found in observed hurricanes is translated into a model criterion. In addition, the temperature anomaly at 300 hPa has to be larger than at the 850 hPa level. Conversely, the mean wind speed at the 850 hPa level has to exceed that at the 300 hPa level. A minimum life-time of 1.5 days is required for the tropical cyclone. As shown in Table 4.2, other studies follow such an approach with slight modifications of single criteria. A less rigorous condition on vorticity, for instance,

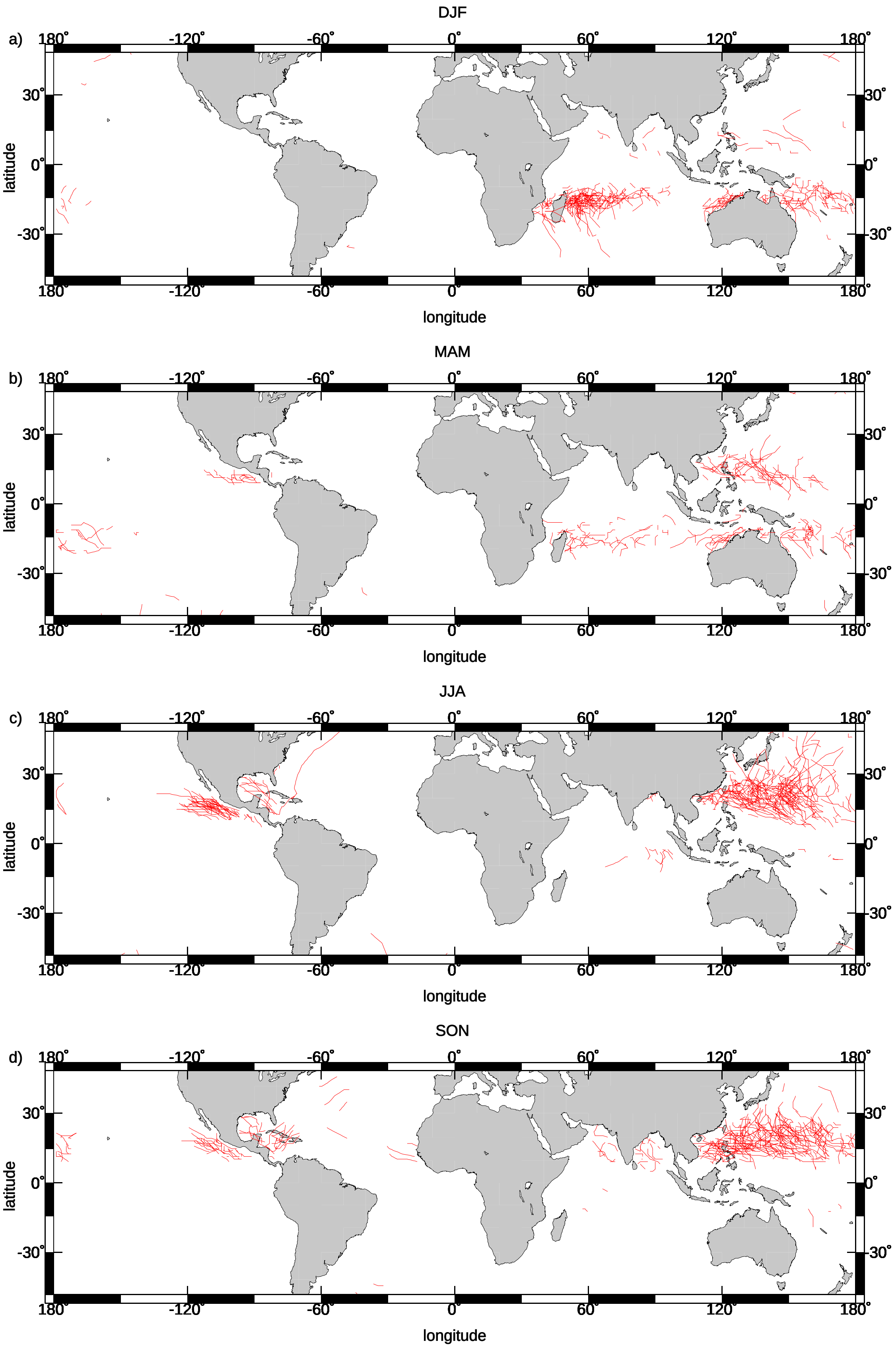

Figure 4.1: *Tropical storm tracks simulated by the 20-year ECHAM4/T106 AMIP run for the different seasons a) Dec.-Feb. b) March-May c) Jun.-Aug. and d) Sept.-Nov.*

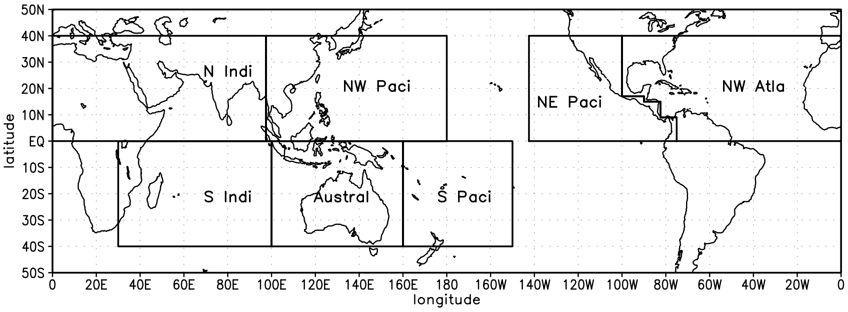

Figure 4.2: *Regions for which the output of the detection algorithm is analyzed.*

is applied in May's (2000) study.
Although T106 represents a rather high horizontal resolution in the context of global climate simulations, it has to be taken into account that even this resolution is not able to capture all of the characteristics of observed tropical cyclones, e.g. the eye of a hurricane. For a correct representation of this feature, even higher resolution of the order of tens of km is needed.

The detection algorithm is applied to the twice-daily model output of the 20-year AMIP-type ECHAM4/T106 run described above. The lowest pressure detected in the entire AMIP run amounts to 921 hPa which is lower than the minimum of 957 hPa found in Bengtsson et al. (1995). The maximum wind speed close to a grid point fulfilling the vorticity criterion amounts to 51.1 ms^{-1} and is thus comparable to the value of 53.1 ms^{-1} in Bengtsson et al. (1995).
The tracks of all tropical storms detected in the AMIP run are shown in Fig. 4.1. A distinction is made between the different seasons (DJF, MAM, JJA, SON) in order to highlight the different timing of peak tropical cyclone activity in different parts of the globe. The overall tendency that major storm activity develops in the summer and fall months of the respective hemisphere is well captured by ECHAM4. During DJF, most cyclones are found in the Southern Indian Ocean and close to eastern Australia. In the Northern Hemisphere, the major cyclone activity is simulated over the North Western Pacific during the JJA and SON seasons. These are also the seasons with major Atlantic and North Eastern Pacific tropical cyclone activity.

Tropical cyclone activity is now analyzed in different regions. Here, Bengtsson et al.'s (1995) definition of the various regions is followed (Fig. 4.2). Results for each model year and the different regions are shown in Table 4.3. It can be clearly seen from Table 4.3 that the ECHAM4 model appears to perform better in the tropical Southern Hemisphere than in the Northern Hemisphere. Compared to the observational results of Gray (1979), only about half of the Northern Hemisphere tropical cyclones are captured by the model. With the exception of the North Western Pacific region, all the Northern Hemisphere regions contribute to this underestimation. Especially in the North Eastern Pacific and the North Atlantic, the number of simulated storms largely falls short of the observed value. The model does not reproduce the finding by Yumoto and Matsuura (2001) that

Simulated tropical storms by year and ocean basin

Year	trop. S.-Hemi.	trop. N.-Hemi.	NE Paci	NW Paci	S Paci	NW Atla	N Indi	S Indi	Austral
1979	8	29	4	18	1	5	2	5	2
1980	17	31	2	24	4	1	3	7	5
1981	17	39	1	33	4	3	0	11	2
1982	19	37	8	25	3	0	2	9	7
1983	19	17	6	8	4	1	2	7	7
1984	27	20	6	14	7	0	0	12	8
1985	10	24	2	19	1	3	0	7	2
1986	14	32	6	23	2	2	0	9	3
1987	10	30	5	19	3	4	2	5	2
1988	15	24	5	16	3	3	0	7	5
1989	21	32	2	24	2	2	4	13	6
1990	21	33	9	29	0	0	2	12	8
1991	18	36	6	25	5	0	5	8	5
1992	15	34	10	19	7	1	1	4	4
1993	15	29	7	12	5	3	5	4	5
1994	16	39	8	26	3	1	2	6	7
1995	15	22	3	18	3	1	0	5	6
1996	19	28	4	21	3	2	1	13	3
1997	9	37	4	26	0	3	2	3	6
1998	14	17	0	13	4	3	1	7	3
Σ	319	590	98	403	64	38	34	154	96
B.*4	536	1124	156	656	80	216	80	256	188
Gray (1979)	24.5	54.6	23.4	26.3	5.9	8.8	6.4	8.4	10.3
$\overline{n}$	16.0	29.5	4.9	20.2	3.2	1.9	1.7	7.7	4.8

Table 4.3: *Number of tropical storms per year in selected regions as detected by applying Bengtsson et al.'s (1995) algorithm to the 20 years of the ECHAM4/T106 AMIP-type simulation. For comparison, the results by Bengtsson et al. (1995) extrapolated to 20 years are included into the table (B.*4). The last two rows show a comparison between the average number of storms in each region as observed (Gray, 1979) and simulated.*

almost one-third of all tropical cyclones develops within the NW Pacific region. The ratio amounts to about 45% in the AMIP integration.

As illustrated by Fig. 4.1 and Table 4.3, the performance of the ECHAM4 model in simulating Atlantic hurricanes has largely deteriorated compared to the former model version (ECHAM3). The results of Bengtsson et al. (1995) were determined from a 5-year model simulation. Their results are multiplied by a factor of 4 for direct comparison with the output of the 20-year AMIP run (B.*4 in Table 4.3). Only about one quarter of the observed average annual number (8.8) of Atlantic tropical storms is simulated by the ECHAM4 model. ECHAM3, on the other hand, captures both, the seasonality and the number of observed tropical storms in the Atlantic. In almost all regions, the numbers simulated by ECHAM3 clearly exceed those simulated by ECHAM4. These findings largely confirm the results of May (2000). The sensitivity of the results to the chosen thresholds was also tested. In contrast to Walsh (1997), however, no strong sensitivity of the number of cyclones to the 10 m wind speed threshold was found. The number of Atlantic tropical cyclones, for example, remained relatively low when the treshold was lowered.

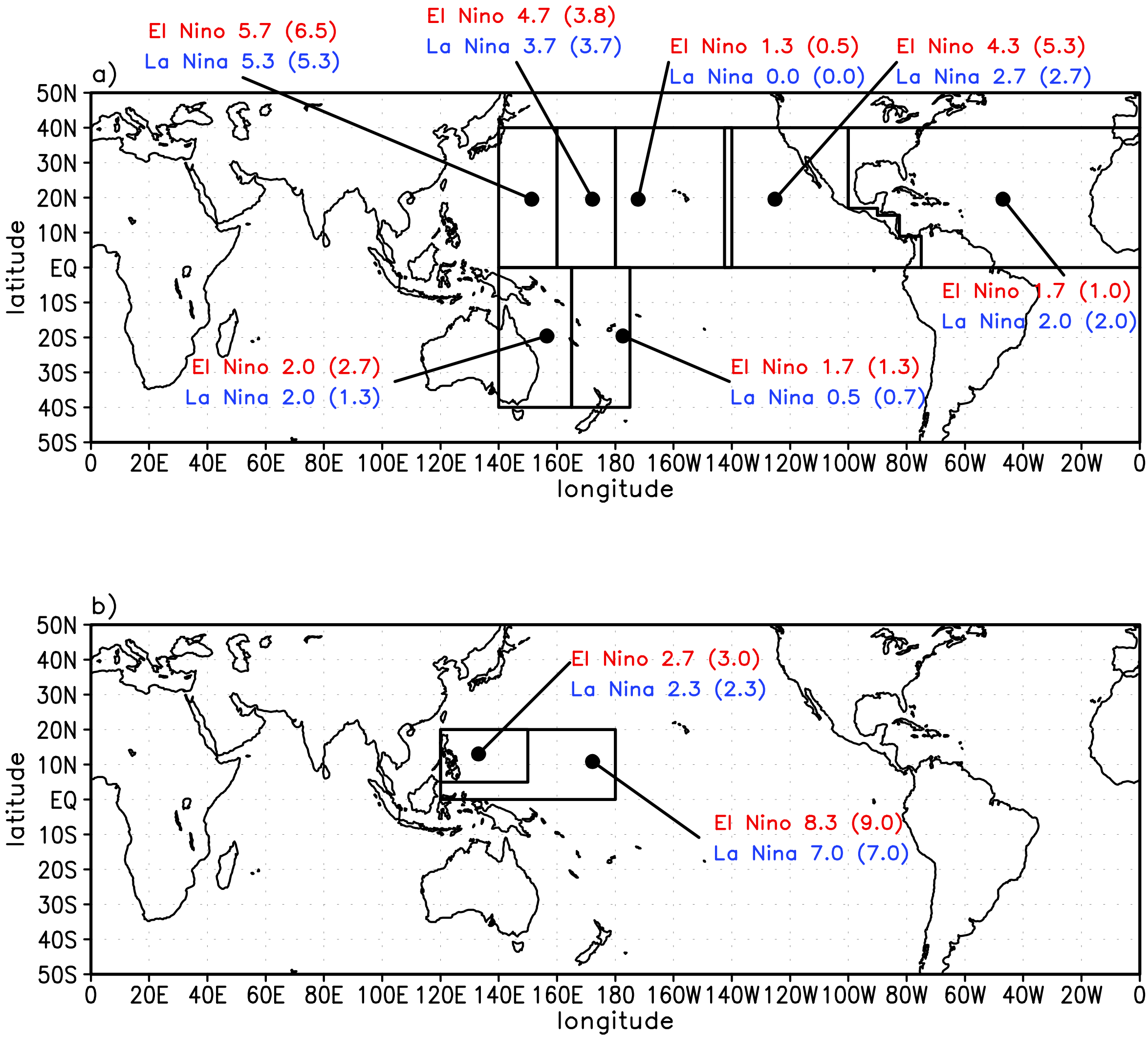

Figure 4.3: *a) Average number of tropical storms identified in the AMIP run for JASO months of El Niño and La Niña years for selected regions (based on 3 El Niño and 3 La Niña events). Numbers in brackets are based on composites excluding the record 1997/98 El Niño. b) As a) for basins defined by Matsuura et al. (1999).*

4.2 ENSO impacts in the tropics

4.2.1 ENSO and tropical storms

Various observational relationships of tropical storms (TS) with ENSO have been reported (Landsea (2000) and references therein; Yumoto et al., 2001). The sign of the correlation, however, largely depends on which part of the ocean basins is considered. In the following, the impact of ENSO on the number of simulated tropical storms in different basins is investigated based on the AMIP run. First, the El Niño and La Niña years have to be identified. In the western North Atlantic and North Pacific regions, the June-October (JASO) months can be considered as the season of main hurricane and typhoon activity. Including November into the analysis does not lead to substantial changes in the results. The Niño3 SST anomaly timeseries is calculated from the JASO months of the HadISST timeseries. This results in a standard deviation (σ) of ± 0.93 in the Niño3 region. Years with JASO Niño3 SSTA exceeding $\sigma = 0.93$ are defined as El Niño years (1982, 1987, and 1997) and years exhibiting a JASO Niño3 SSTA below $\sigma = -0.93$ as La Niña years (1984, 1985, and 1988).

Fig. 4.3 illustrates the results of compositing the number of TS for El Niño and La Niña years. The numbers for the Australian basins shown in Fig. 4.3a are determined from a similar analysis for the Southern Hemisphere storm season.

It is evident that the numbers of TS for El Niño and La Niña events are not substantially different from each other. Over the western North Atlantic, a slight reduction of TS during El Niño years compared to La Niña years is simulated. In all other boxes, slightly larger average numbers of TS are simulated in El Niño years compared to La Niña years. For the western North Pacific box between 160°E and the dateline, the AMIP run reproduces the observed tendency (Landsea, 2000) of a slight increase of the number of TS during El Niño events. The same result is simulated for the central North Pacific (180°-140°W).

It should be noted that the results are dependent on how the composites are determined. When the analysis is repeated but with the record 1997/98 El Niño excluded, the composites consist of the same La Niña seasons as above (1984, 1985, 1988), but four El Niño seasons (1982, 1983, 1987, 1991). The resulting numbers are included in brackets in Fig. 4.3. The lower panel (Fig. 4.3b) shows two boxes defined by Matsuura et al. (1999) for the western North Pacific. Even for the smaller box (5°N-20°N, 120°E-150°E) and the second compositing method, the results by Matsuura et al. (1999) (El Niño: 7.6, La Niña: 8.8 TS events) of slightly reduced TS numbers during El Niño events are not reproduced by the AMIP run. This illustrates the sensitivity of the results to the analyzed model and period.

Furthermore, results are dependent on the precise definition of the respective boxes (e.g. in case of the western North Pacific, Fig. 4.3b). The larger the considered area, the more probable a compensating effect within the box becomes. On interdecadal timescales, Yumoto and Matsuura (2001) have demonstrated differences in the number of TS only within the region 10°-20°N, 130°E-170°E, but not within the region 20°-30°N, 140°E-150°E.

For a comparison of the results with other studies (e.g. Matsuura et al., 1999), it has to be taken into account that the detection thresholds used in their study are quite different from those applied here. As an example, Matsuura et al. (1999) do not have any constraints on the temperature structure at all. There are different opinions about the ENSO impact on western North Pacific TS. While in some studies, a decrease of the number of TS in the western North Pacific is found, other studies do not find a significant correlation between ENSO and the TS activity in the western North Pacific at all (e.g. Lander, 1994). The results of this thesis also do not suggest a substantial difference between El Niño and La Niña years with respect to TS activity. One should keep in mind, however, that the

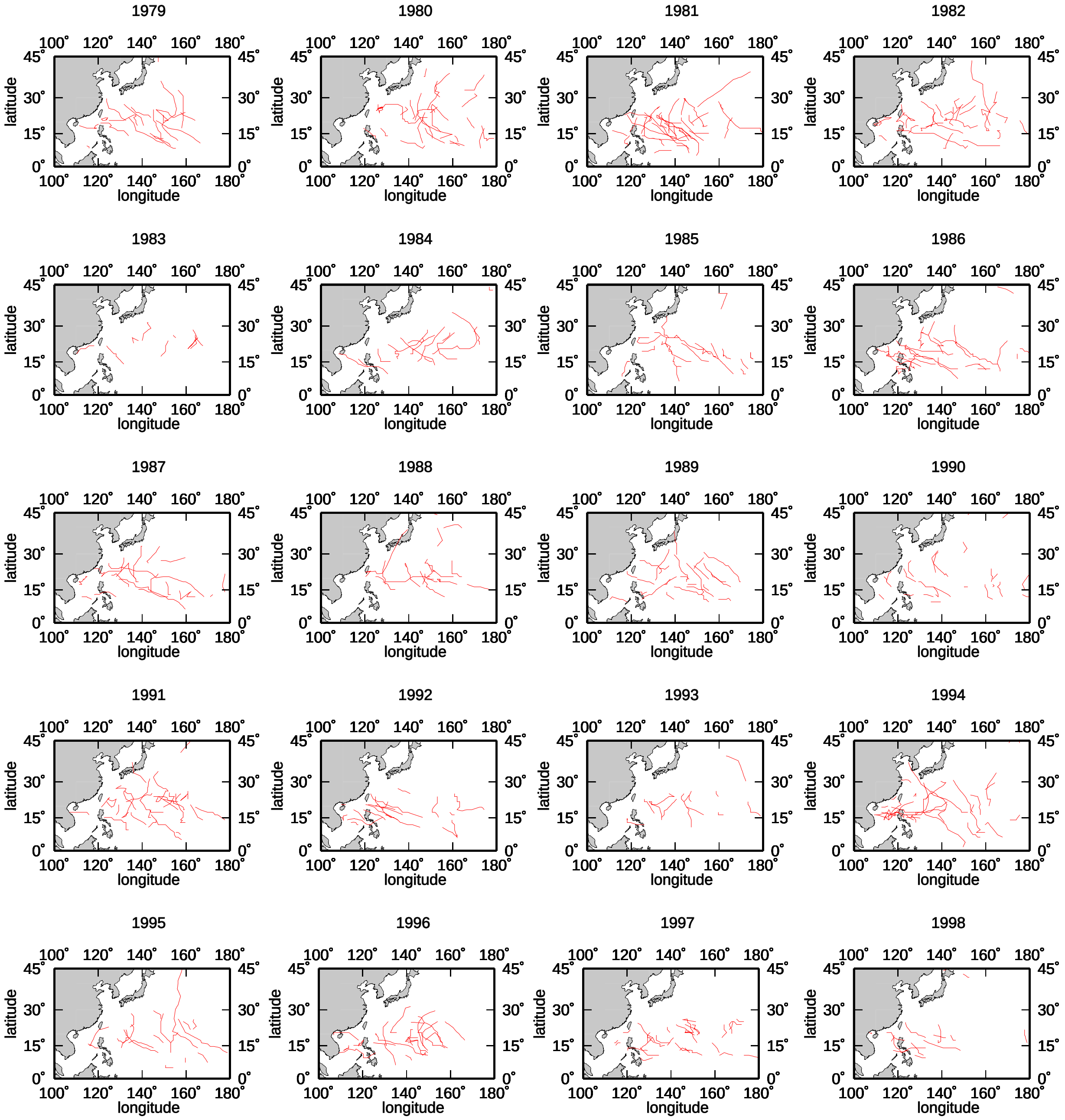

Figure 4.4: *Tropical storm tracks in the western North Pacific (100° E-180°, 0°-45° N) for each JASO season of the 20-year AMIP run. Tracks as determined using the Bengtsson et al. (1995) algorithm.*

model used here suffers from serious systematic errors.

The tracks and the locations of TS genesis are often claimed to be also influenced by ENSO. The simulated tropical storm tracks for the JASO months in the western North Pacific are shown in Fig. 4.4 for all years. In 1983, a year typically considered as an El Niño year but which would have been excluded from the composites, clearly reduced typhoon activity is simulated which is latitudinally confined within 15°N-30°N. The tracks of the preceding El Niño year of 1982, however, bear much more resemblance to the "normal" year of 1980. The regional restriction can also be seen in the years 1997 and 1998, in which almost no TS crosses 25°N. In addition to the latitudinal confinement, some years are characterized by TS activity concentrated in the far western North Pacific basin, i.e. west of 160°E. The years 1979, 1996 and 1998 are examples of such a confinement. These rather strong regional variations, however, cannot be attributed systematically to ENSO-related variations. As stated earlier, other mechanisms like local effects or the influence from the stratosphere have to be considered.

4.2.2 ENSO and large-scale environmental conditions

For a full understanding of the genesis of tropical storms and their interannual behaviour, both local and large-scale effects have to be analyzed. It has been stated in ch. 4.1 that several factors contribute to the genesis of tropical storms. In the present section, an effort is made to shed more light a) on their role with respect to the general ability of ECHAM4 to simulate tropical cyclones, and b) on their role in mediating the ENSO impact.
In the Atlantic basin, one important factor is the vertical shear of the zonal wind. Gray (1984) has shown that vertical shear can be detrimental to hurricane development. In a recent study, Frank and Ritchie (2001) using a mesoscale model further elucidate the details of how increased vertical shear leads to a negative feedback onto the vortex dynamics. Here, the vertical shear is defined as the difference between the zonal winds at the 200 hPa and 850 hPa levels. The tropical 200 hPa zonal winds belong to the critical quantities with respect to the performance of the ECHAM4 model since they exhibit a westerly bias compared to observations (see ch. 2.1). Regarding the substantial underestimation of Atlantic tropical storms within the ECHAM4 model (see ch. 4.1), it is hypothesized that too strong vertical shear might prevent TS development in ECHAM4 simulations. Therefore, the vertical shear as simulated in the AMIP run is compared to ECMWF reanalysis data (Gibson et al., 1999).

The dominant role of the 200 hPa zonal wind in the vertical shear during the early part of the Atlantic TS season (JJA) is evident from Fig. 4.5. The figure contains the Atlantic TS main development region (MDR, ≈ 10°-20°N) identified by Goldenberg and Shapiro (1996). The ECHAM4 model exhibits an upper-tropospheric westerly bias (Fig. 4.5a) in the tropics with respect to the ECMWF wind fields (Fig. 4.5b). Within the MDR, the AMIP and the ECMWF u200 fields even exhibit opposite signs. At the 850 hPa level,

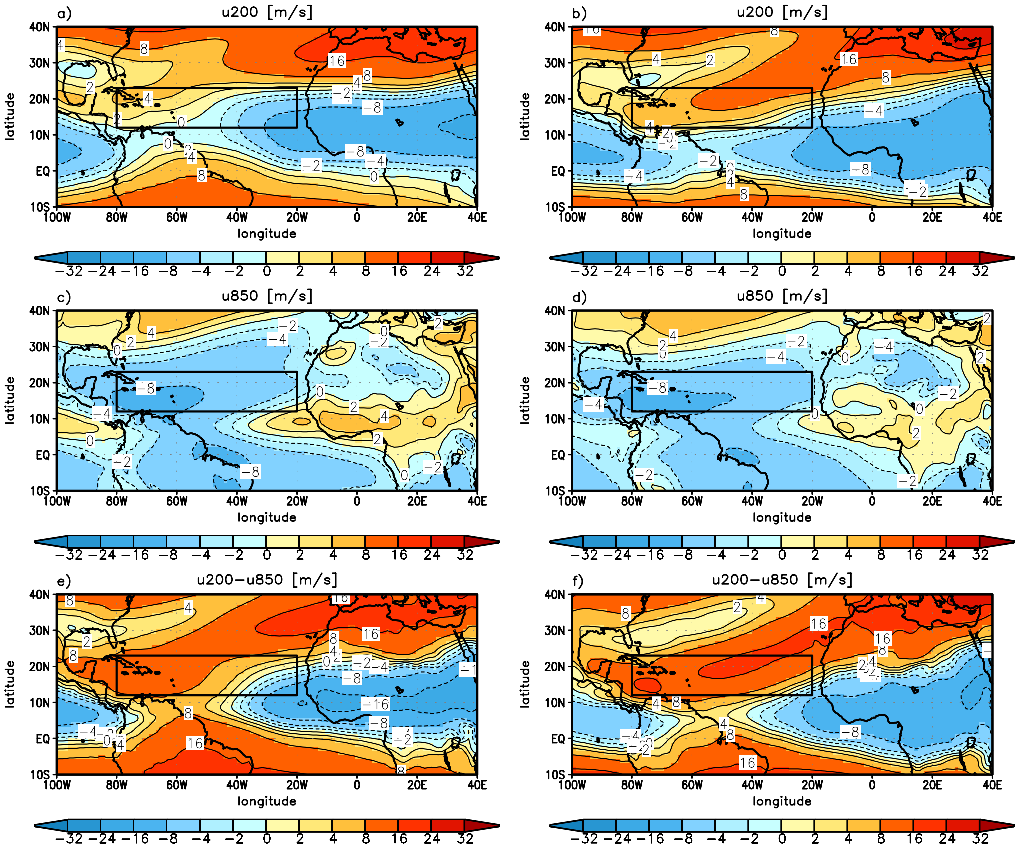

Figure 4.5: *Seasonal (JJA) mean of the 200 hPa zonal wind (a,b), the 850 hPa zonal wind (c,d), and (e,f) the vertical shear of the zonal wind for the AMIP experiment (left panels) and for ECMWF reanalysis data (right panels). The box denotes the Atlantic TS main development region according to Goldenberg and Shapiro (1996). Units are* ms^{-1}. *The colorbars indicate the irregular contour intervals.*

slightly stronger easterlies are simulated in the AMIP experiment for the eastern part of the MDR. This is also evident from the difference plots between the 20-year average seasonal mean of the AMIP run and the corresponding ECMWF seasonal mean of the u200, u850, and the vertical shear fields (Fig. 4.6). A distinction is made between the JJA (Fig. 4.6, left panels) and SON (Fig. 4.6, right panels) seasons. A stronger (weaker) vertical shear is simulated in the ECHAM4 model compared to ECMWF wind fields in the tropics (MDR). It should be noted that also the 850 hPa wind field contributes to these shear errors.

During the second half of the Atlantic TS season (SON), slightly too strong easterlies are simulated by ECHAM4 at the 850 hPa level within the MDR. Together with weaker westerlies at the 200 hPa level, this results in a weaker vertical shear in the ECHAM4 model in the MDR during SON compared to the ECMWF reanalysis. The reverse is true for the tropics during the SON season. In general, ECHAM4 and ECMWF reanalysis exhibit a strong meridional variation in their shears.

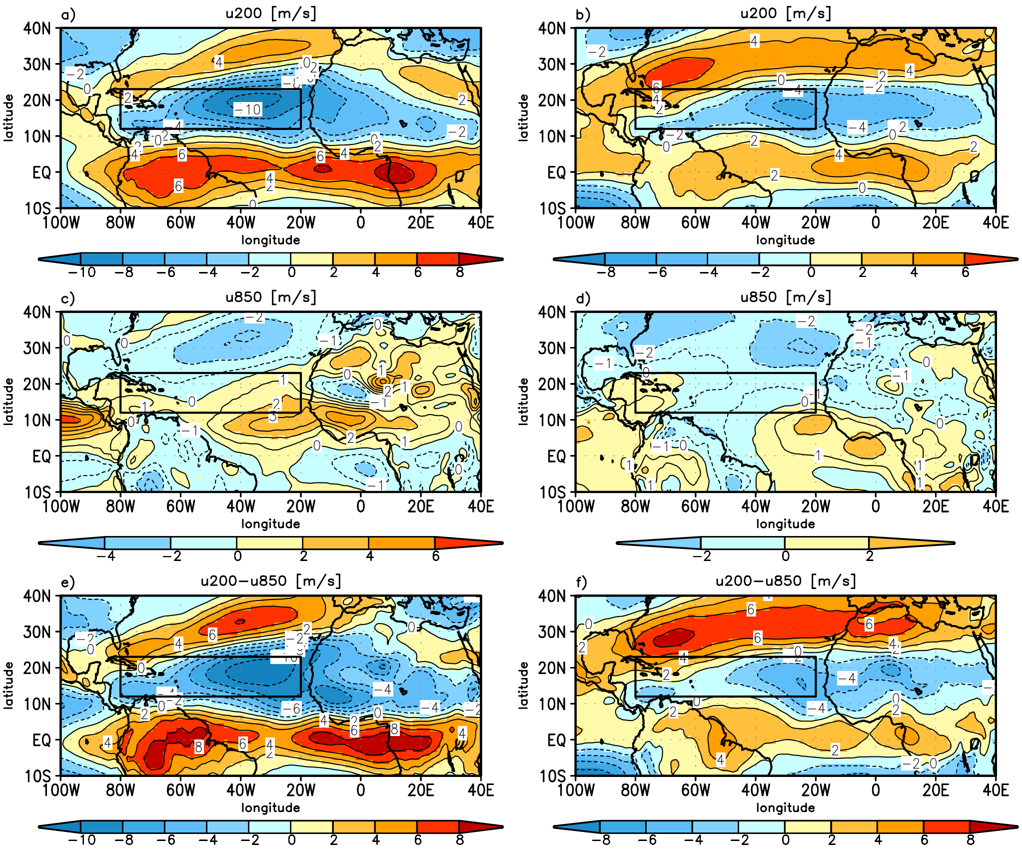

Figure 4.6: *Seasonal mean difference between the AMIP experiment and the ECMWF reanalysis data for the JJA (left panels) and SON (right panels) seasons. (a,b) 200 hPa zonal wind, (c,d) 850 hPa zonal wind, and (e,f) the vertical shear of the zonal wind. Units are ms*$^{-1}$*. The box is defined as in Fig. 4.5.*

Hence, similar discrepancies - although considerably weaker - between ECHAM4 and the ECMWF wind fields exist for the SON season (Fig. 4.6, right panels).
Thus, it can be concluded that the vertical shear simulated by ECHAM4 in the MDR (tropics) is clearly weaker (stronger) than the shear found in the ECMWF reanalysis. This result holds for both JJA and SON seasons. Therefore, the wind shear in the MDR does not seem to be the major reason for the reduced ability of the ECHAM4 model in simulating Atlantic TS. Therefore, other factors and model deficiencies should be taken into account as possible reasons, e.g. the convection scheme. A more detailed analysis, however, has not been performed in this thesis.

For the Atlantic basin, it has been shown by Gray (1984) that the vertical wind shear is considerably strengthened (weakened) during El Niño (La Niña) events, with increased (weakened) vertical shear being detrimental (favorable) to TS development. Therefore, it is investigated whether this observed relationship is captured by the model simulation. For this purpose, seasonal mean anomalies are calculated with respect to the 20-year mean, both from the HadISST in the Niño3 region and the vertical wind shear as simu-

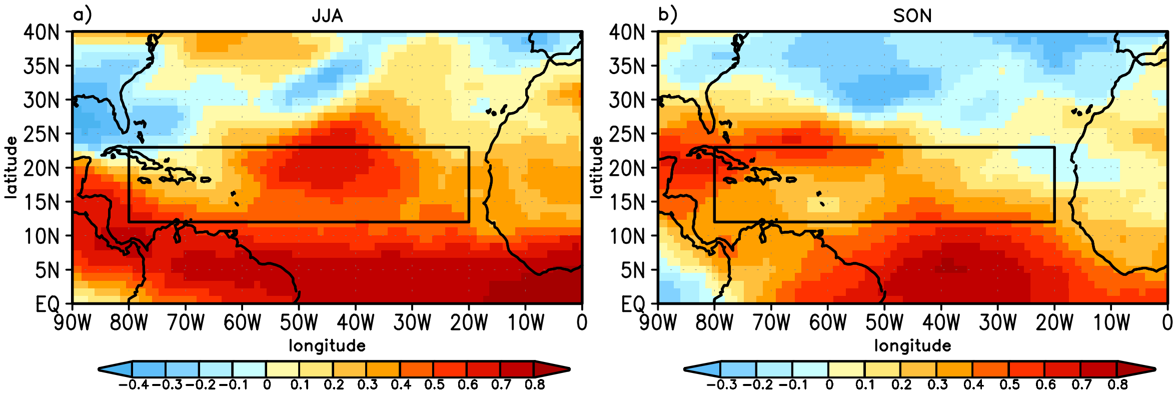

Figure 4.7: *Correlation of the simulated seasonal mean anomalies of the vertical wind shear (difference between u200 and u850) and Niño3 SST for (a) the JJA season, and (b) the SON season. The box denotes the Atlantic main development region (MDR) defined by Goldenberg and Shapiro (1996).*

lated by the AMIP run. Then the seasonal mean JJA (SON) anomalies of the vertical wind shear are correlated with the seasonal mean JJA (SON) anomaly of the HadISST Niño3 timeseries. Highest correlations (r) with eastern tropical Pacific SST (Fig. 4.7) can be found in the tropical belt of 0°-10°N (correlations of $|r| > 0.4$ are significant at the 95% level). This can be understood in terms of a modification of the equatorial Walker circulation. Correlations of up to 0.7 (Fig. 4.7a) are also found within the MDR. These correlations mainly result from a strong relationship between the eastern tropical Pacific SST and the 200 hPa wind field (not shown). Fig. 4.7b closely resembles the results by Goldenberg and Shapiro (1996) who focussed on the months of August, September and October. They also find the Niño3 SST anomalies to be positively correlated with the vertical shear over the tropical Atlantic and the MDR.

Finally, the results have to be put into the context of other studies. ENSO is not the only phenomenon that influences Atlantic hurricane activity. Monsoon rainfall over West Africa also exhibits a strong association to Atlantic hurricanes. In a study by Goldenberg and Shapiro (1996), it has been demonstrated that both ENSO and Sahelian rainfall have an impact on the Atlantic hurricane activity. ENSO-related changes in the wind field were found to be more equatorially confined while Sahelian rainfall was found to have more impact on the conditions within the MDR. Furthermore, Wu and Lau (1992) emphasize that it appears to be difficult to reconcile the results of different studies of the ENSO-Atlantic hurricanes relationship. Results are highly dependent on the ENSO extremes included in composite studies and can be contradictory when different time periods are analyzed.

5 Conclusions and Outlook

5.1 Conclusions

The aim of this thesis was to obtain a better understanding of the atmospheric response to ENSO. An overview of the results based on AGCM simulations forced by prescribed SST is presented. The analysis concentrates on the following aspects:

1. the role of horizontal resolution,
2. the role of tropical Pacific SST,
3. the symmetry of the atmospheric response,
4. the role of synoptic-scale eddies in feeding back onto the mean flow, and
5. the relationship between ENSO and tropical storms.

Most of the experiments have been performed at rather high horizontal resolution (T106), since the representation of topography is more realistic and a wider range of spatial scales can be captured. Although the enhancement of horizontal resolution cannot lead to improvements of the simulated response in every respect, the important role of the high resolution is clearly emphasized from the experimental results. While over the North Pacific, no major resolution dependence of the atmospheric response is found, a different conclusion can be drawn for the North Atlantic/European sector. Only at T106 resolution, the observational ENSO composites of Fraedrich and Müller (1992) can be reproduced successfully. At T42 resolution, no significant response over Europe is simulated. This resolution dependence is mainly attributed to a more eastward extension of the North Atlantic storm track at T106 resolution.

The relative role of the tropical Pacific SST anomalies in exciting midlatitude atmospheric anomalies has been addressed with two experiments (GRWI, TRWI) only differing in the spatial extent of the El Niño-related SST forcing. Evidence is presented that the tropical Pacific plays a key role compared to the other ocean basins. In particular, the impact of the tropical Pacific SST anomalies extends to rather remote regions such as Europe.

With respect to the symmetry of the atmospheric response to El Niño and La Niña forcing, it is shown that the midlatitudinal signal, at least in some regions, is far from exhibiting a simple antisymmetric response, with respect to the sign of the tropical Pacific forcing. For example, the ENSO signal over Europe, although significant, is not found to be exactly antisymmetric. Therefore, I conclude that caution is required when applying linear theory in comparisons between the El Niño and La Niña responses. Finally, the experiments support the study by Hoerling et al. (2001b) stating the existence of a midlatitudinal signal also under La Niña conditions. The results presented in this thesis further demonstrate that the antisymmetry of the atmospheric response should not only be evaluated from zonal averages, since longitudinal differences exist.

When focussing on the symmetry of the eddy response, it appears that the transient eddies play a more important role in the El Niño (TRWI) experiment than in its La Niña counterpart (NTRWI). For example, the response of the major storm track over the North Atlantic is hard to evaluate in the La Niña experiment. Hence, it can be hypothesized that stationary eddies provide the more important contributions to the seasonal mean ENSO response. It is shown, however, that both the stationary and transient eddies respond significantly to ENSO. The responses of both have been shown to be clearly dependent on the resolution and the sign of the tropical forcing. The eddy feedback onto the mean flow is analyzed in terms of the eddy forcing of the mean streamfunction and the mean temperature. Evidence is presented from the high resolution experiments that the transient eddy feedback is positive at upper-tropospheric levels and negative at lower levels.

All these inferences have been drawn from seasonal ECHAM4 ensemble experiments forced by specified SST anomalies. Additionally, a 20-year-AMIP run forced by the observed history of SST for the years 1979-1998 was also conducted. This experiment has been analyzed primarily with a special focus on tropical storms.
It has been demonstrated that the ECHAM4 model exhibits some ability to simulate tropical storms. Especially in the North Atlantic region, the observed number of Atlantic hurricanes, however, is substantially underestimated. Nevertheless, the number and tracks of tropical storms in different ocean basins revealed weak differences between El Niño and La Niña years. In a second step, it has been shown from a comparison between ECHAM4 and ECMWF reanalysis wind data that the inability of ECHAM4 to realistically simulate tropical storms in the Atlantic can partly be attributed to the ECHAM4 bias in the vertical wind shear. Rather, an unexplained interplay of different factors may play a role. ECHAM4 exhibits systematic errors in the tropospheric temperature and zonal wind fields, with an overly pronounced representation of the tropical Walker circulation. But numerical modifications and changes in the parameterizations (new radiation scheme, closure for deep convection based on convective instability instead of moisture convergence) can also influence the model's ability to simulate tropical storms (May, 2000). However, high correlations of the tropical Pacific SST and the vertical wind shear in the Atlantic hurricane development region indicate that the model reproduces the observed large-scale circulation changes (Goldenberg and Shapiro, 1996) reasonably well.

5.2 Outlook

The ensemble size used within this thesis is relatively small. Wehner (2000) claims that larger ensembles may be necessary in view of the high internal atmospheric variability, particularly at high latitudes. Therefore, it would be interesting to test the sensitivity of the atmospheric response to the ensemble size. To some extent, the tropical Pacific regression experiment (TRWI) can be interpreted as extending the ensemble size of the global regression experiment (GRWI), and the tropical Pacific experiment confirms the existence of a significant response over the North Atlantic/European sector. Branković and Gregory (2001) found the necessary ensemble size to be dependent on the season, the atmospheric parameter considered, and the resolution. In this respect, the ensembles presented here could be systematically extended to cover these different aspects. First experiments performed analogously to investigate the atmospheric ENSO response during the boreal spring season are subject of ongoing research.

In order to complete the set of ensemble experiments, another ensemble would be required with an SST forcing complementary to the TRWI anomaly pattern. Thus, the role of SST anomalies outside the tropical Pacific could be determined explicitly. However, the set of experiments presented here suggests a dominant role of the tropical Pacific compared to the SST anomalies elsewhere. Another interesting variation would be to construct the idealized SST forcing from a one-sided regression analysis (Hoerling et al., 2001b) which takes into account the asymmetry between the observed El Niño and La Niña SST anomalies.

It cannot be ruled out that even the SST regression pattern with respect to the Niño3 SST anomaly may depend on the base period. Therefore, it has been questioned by Rimbu et al. (2003) whether a canonical ENSO response exists at all. Raible et al. (2001) show that decadal modulations of the global ENSO teleconnections may exist. One also has to take into account the inter-El Niño (La Niña) variability which, depending on the region, can be large and lead to a corresponding spread in the atmospheric response (Kumar and Hoerling, 1997). Understanding these differences between the observed atmospheric response to a single ENSO extreme event and the picture provided by a composite or an ensemble mean remains a challenging topic for future work.

Within this thesis, AMIP-type experiments were conducted, i.e. uncoupled experiments with prescribed SST. In order to account for the observed atmosphere-ocean interaction, AMIP-type experiments always have to be analyzed in comparison to coupled AOGCM experiments. However, in spite of their shortcomings, AMIP-type experiments can be a useful tool, depending on the respective research focus. This is supported by a study of Barsugli and Battisti (1998) who compared an AMIP-type experiment to a coupled-AGCM-mixed layer ocean experiment (their TOGA and TOGA-ML experiments). They have shown that the successful simulation of midlatitudinal ENSO-related anomalies does not require explicit coupling in midlatitudes.

Although part of this analysis focussed on changes in subseasonal variability (ch. 3.2 and 3.3), the larger part of this thesis dealt with seasonal means. In a next step, it would be interesting to investigate in more detail the time evolution of the atmospheric response on subseasonal timescales. Preliminary results revealed the importance of single months in dominating the seasonal mean response. In a further step, it will be worthwhile to examine the signal propagation out of the tropics on daily timescales (Jin and Hoskins, 1995) and investigate changes in the probability density functions of atmospheric variables in response to ENSO. This could be particularly interesting with respect to the role of horizontal resolution. It has been pointed out earlier (Sardeshmukh et al., 2000) that there may be ENSO-related changes in the probability of extreme values, although the changes in the mean of the distribution are of minor magnitude.

For a more thorough understanding of the dynamical components contributing to the atmospheric ENSO response, a linearized version of ECHAM4 should be developed in order to perform experiments analogous to those of Held et al. (1989) for a clear separation between transient eddy vorticity and heat fluxes. From a dynamical perspective, the mutual dependence and presumably nonlinear interaction between planetary waves and synoptic-scale eddies also needs to be taken into account.

This study emphasizes the role of high horizontal resolution in the simulation of transient eddies and, as a consequence, the atmospheric response to ENSO. It is shown here that part of the extratropical ENSO response can be successfully simulated, if the SSTs are prescribed. The usefulness of such response experiments for real forecasts presupposes that the SST anomalies can be predicted. In practice, however, SST anomalies are only partially predictable on a seasonal basis. Nevertheless, prediction of SST in the tropics has been very successful and therefore, if the response to SST is fully understood, the prediction of extratropical atmospheric anomalies in response to ENSO might be partially conceivable.

A Appendix

Plumb vector

The Plumb vector diagnostic represents a powerful tool to analyze the stationary wave activity flux (Plumb, 1985). It has been developed as an extension to three dimensions from the two-dimensional Eliassen-Palm (EP) flux. In a zonal mean framework, the EP flux describes the poleward flux of temperature and momentum by stationary waves. The divergence of the EP flux can be interpreted as the forcing exerted by stationary eddies on the mean flow. Plumb's (1985) efforts were aimed at developing a three-dimensional picture of the meridional energy transports. For a detailed derivation of the Plumb vector the reader is referred to Plumb (1985). Here, only the mathematical expression for the Plumb vector is given.

$$\vec{F_s} = \frac{1}{2}\, p \begin{pmatrix} \left(\frac{\partial \psi^*}{\partial x}\right)^2 - \psi^* \frac{\partial^2 \psi^*}{\partial x^2} \\ \frac{\partial \psi^*}{\partial x}\frac{\partial \psi^*}{\partial y} - \psi^* \frac{\partial^2 \psi^*}{\partial x \partial y} \\ \frac{f^2}{N^2}\left(\frac{\partial \psi^*}{\partial x}\frac{\partial \psi^*}{\partial z} - \psi^* \frac{\partial^2 \psi^*}{\partial x \partial z}\right) \end{pmatrix} \tag{A.1}$$

where p denotes $pressure/(1000\, hPa)$, ψ^* the zonal anomalies of the horizontal streamfunction, f the Coriolis parameter, and N the buoyancy frequency.

The divergence of $\vec{F_s}$ is zero for stationary and conservative waves. Regions with non-zero divergence may result from one or several of the following sources for the piling-up or export of stationary wave activity: a) orographic forcing, b) forcing due to diabatic heating, and c) forcing by interaction with transient eddies (they feed back onto the mean flow directly or via latent heat release in the storm tracks and thus may themselves contribute to stationary wave excitation).

Eady growth rate

The Eady model (Eady, 1949) was one of the first idealized models to describe the problem of baroclinic instability. The growth rate σ of an Eady wave solution is a function of wavenumber (k, l). The growth rate of the most unstable wave in the Eady model is given by (see also Hoskins and Valdes, 1990)

$$\sigma_{BI} = 0.31\, f \left|\frac{\partial \vec{v}}{\partial z}\right| / \mathcal{N} \tag{A.2}$$

with f denoting the Coriolis parameter, $\vec{v}$ the horizontal wind vector, z the vertical coordinate and $\mathcal{N}$ the Brunt Väisälä frequency. In some studies, σ_{BI} is also termed baroclinicity index. The Eady growth rate is a measure for the atmospheric baroclinicity. It is determined by the vertical wind shear, and, from thermal wind arguments, by the meridional temperature gradient, but also by the static stability of the atmosphere, here expressed by $\mathcal{N}$. Regions exhibiting distinct baroclinicity may give rise to the development of extratropical storm tracks, i.e. of baroclinic transient eddies.

A Taylor series expansion allows to distinguish between σ_{BI} changes due to changes in the vertical shear and due to changes in the Brunt Väisälä frequency (K. Walter (1999), Master Thesis in Meteorology, University of Hamburg, Germany). Thus, the changes of σ_{BI} can be approximately written as follows.

$$\Delta\sigma_{BI,\left|\frac{\partial \vec{v}}{\partial z}\right|} \approx \left.\frac{\partial\, \sigma_{BI}}{\partial \left|\frac{\partial \vec{v}}{\partial z}\right|}\right|_{CTRL} \cdot \Delta \left|\frac{\partial \vec{v}}{\partial z}\right| \tag{A.3}$$

$$\Delta\sigma_{BI,\mathcal{N}} \approx \left.\frac{\partial\, \sigma_{BI}}{\partial \mathcal{N}}\right|_{CTRL} \cdot \Delta\mathcal{N} \tag{A.4}$$

Here X denotes a quantity simulated by both a control and a sensitivity experiment, and the response of X in the sensitivity experiment compared to the control experiment is given bei ΔX.

Midlatitude cyclone tracking analysis

In order to analyze individual midlatitudinal cyclones and their tracks from observations or model simulations, Blender et al. (1997) developed an algorithm which permits an automatic and objective identification of low pressure systems from daily data. A short description of the routine following Blender et al. (1997) will be given.

In a first step, cyclones are identified from local minima of the 1000 hPa geopotential height field, z1000. In the model, this condition has to be fulfilled by an area of 3×3 gridpoints. As a second condition, a positive gradient of the z1000 field has to be present within an area of 1000 x 1000 km^2 around the detected minimum in the z1000 field.

The algorithm not only checks for these conditions but also determines trajectories of individual cyclones from successive timesteps. In the present thesis, the cyclone tracks are also analyzed from the 1000 hPa geopotential height field based on twice-daily data. Before the application of the routine, the unfiltered data of all T106 experiments have been interpolated to T42 resolution. In this context, no ensemble mean has been calculated for the cyclone statistics or tracks, but instead, all simulated cyclones of an ensemble are taken into account.

Eddy kinetic energy equation

As shown by Frisius (1995, Master Thesis in Meteorology, University of Hamburg, Germany), the time mean diagnostic equation of eddy kinetic energy, K_e, can be derived from the quasi-geostrophic momentum equations. Quasi-geostrophy is an adequate approximation to synoptic-scale activity in midlatitudes. The prognostic equation for K_e can be written as (Frisius, Eq. 3.11)

$$\begin{aligned} \frac{\partial K_e}{\partial t} &+ (\overline{u}+u')\frac{\partial K_e}{\partial x} + (\overline{v}+v')\frac{\partial K_e}{\partial y} + u'^2\frac{\partial \overline{u}}{\partial x} + u'v'\frac{\partial \overline{u}}{\partial y} + u'v'\frac{\partial \overline{v}}{\partial x} + v'^2\frac{\partial \overline{v}}{\partial y} \\ &= -u'_a\frac{\partial \varphi'}{\partial x} - v'_a\frac{\partial \varphi'}{\partial y} + u'F'_u + v'F'_v + u'(\frac{\partial \overline{u'^2}}{\partial x} + \frac{\partial \overline{u'v'}}{\partial y}) + v'(\frac{\partial \overline{u'v'}}{\partial x} + \frac{\partial \overline{u'^2}}{\partial y}) \end{aligned} \tag{A.5}$$

with overbars denoting the time mean and primes the deviations therefrom. With the Reynolds averaging rule and taking into account the nondivergence of the geostrophic wind, time averaging leads to the following diagnostic equation for K_e

$$\begin{aligned} \overline{\vec{v}} \cdot \nabla \overline{K_e} + \nabla \cdot \overline{\vec{v}' K'_e} &= -\nabla \cdot \overline{\vec{v_a}'\varphi'} - \frac{\partial \overline{\omega'\varphi'}}{\partial p} - \overline{\omega'\alpha'} + C + dissip. \\ \nabla \cdot \overline{\vec{v}}\, \overline{K_e} + \nabla \cdot \overline{\vec{v}' K'_e} &= -\nabla \cdot \overline{\vec{v_a}'\varphi'} - \frac{\partial \overline{\omega'\varphi'}}{\partial p} - \overline{\omega'\alpha'} + C + dissip. \end{aligned} \tag{A.6}$$

with $\vec{v}$ denoting the geostrophic wind, $\vec{v_a}$ the ageostrophic wind, φ denoting geopotential, α denoting the inverse of density, and ω denoting the vertical wind component in the pressure coordinate system.

• Barotropic production:
Term C in Eq. (A.6) describes the barotropic conversion between transient eddy and mean flow kinetic energy and can be expressed as (Wallace and Lau, 1985)

$$C = -\overline{u'^2}\frac{\partial \overline{u}}{\partial x} - \overline{v'^2}\frac{\partial \overline{v}}{\partial y} - \overline{u'v'}\frac{\partial \overline{u}}{\partial y} - \overline{u'v'}\frac{\partial \overline{v}}{\partial x} \tag{A.7}$$

$$C \approx -\overline{u'^2}\frac{\partial \overline{u}}{\partial x} + \overline{v'^2}\frac{\partial \overline{u}}{\partial x} - \overline{u'v'}\frac{\partial \overline{u}}{\partial y} \tag{A.8}$$

$$
\begin{aligned}
C &\approx (\overline{v'^2 - u'^2}, -\overline{u'v'}) \cdot \nabla\overline{u} && \text{(A.9)} \\
C &\approx \vec{E} \cdot \nabla\overline{u} && \text{(A.10)}
\end{aligned}
$$

The approximation of C by the dot product of the Hoskins et al. (1983) E-vector and the gradient of the zonal wind, $\nabla\overline{u}$, is justified due to the fact that $\partial\overline{v}/\partial x \ll \partial\overline{u}/\partial y$.

- Baroclinic production:

According to Frisius (1995), the first three terms on the r.h.s. of Eq. (A.6) combined represent the baroclinic production of transient eddy kinetic energy and can be expressed differently as

$$
-\nabla \cdot \overline{\vec{v_a}'\varphi'} - \frac{\partial\overline{\omega'\varphi'}}{\partial p} - \overline{\omega'\alpha'} = f(\overline{u'v'_a} - \overline{v'u'_a}) \qquad \text{(A.11)}
$$

with f denoting the Coriolis parameter. The baroclinic production reaches maximum in the case where the ageostrophic wind flows at a 90° angle to the isobars. The first term on the left of Eq. (A.11) represents the divergence of the ageostrophic geopotential flux. The baroclinic production includes the conversion of transient eddy potential energy into transient eddy kinetic energy ($-\overline{\omega'\alpha'}$).

Bibliography

Barsugli, J. J., and D. S. Battisti, 1998: The Basic Effects of Atmosphere-Ocean Thermal Coupling on Midlatitude Variability, *J. Atm. Sci.*, **55**, No. 4, 477-493

Bengtsson, L., M. Botzet, and M. Esch, 1995: Hurricane-type vortices in a general circulation model, *Tellus*, **47A**, 175-196

Bengtsson, L., K. Arpe, E. Roeckner, and U. Schulzweida, 1996: Climate predictability experiments with a general circulation model, *Climate Dynamics*, **12**, 261-278

Bjerknes, J., 1969: Atmospheric Teleconnections from the Equatorial Pacific, *Mon. Wea. Rev.*, **97**, No. 5, 163-172

Blackmon, M. L., 1976: A climatological spectral study of the 500 mb geopotential height of the northern hemisphere, *J. Atm. Sci.*, **33**, No. 8, 1607-1623

Blackmon, M. L., J. M. Wallace, N. C. Lau, and S. L. Mullen, 1977: An observational study of the northern hemisphere wintertime circulation, *J. Atm. Sci.*, **34**, 1040-1053

Blender, R., K. Fraedrich, and F. Lunkeit, 1997: Identification of cyclone-track regimes in the North Atlantic, *Quart. J. R. Met. Soc.*, **123**, 727-741

Branković, C., and D. Gregory, 2001: Impact of horizontal resolution on seasonal integrations, *Climate Dynamics*, **18**, 123-143

Branstator, G., 1995: Organization of Storm Track Anomalies by Recurring Low-Frequency Circulation Anomalies, *J. Atm. Sci.*, **52**, No. 2, 207-226

Cai, M., and M. Mak, 1990: Symbiotic Relation between Planetary and Synoptic-Scale Waves, *J. Atm. Sci.*, **47**, No. 24, 2953-2968

Chang, E. K. M., and I. Orlanski, 1993: On the Dynamics of a Storm Track, *J. Atm. Sciences*, **50**, No. 7, 999-1015

Chang, E. K. M., S. Lee, and K. L. Swanson, 2002: Storm Track Dynamics, *J. Climate*, **15**, No. 16, 2163-2183

Déqué, M., and J. P. Piedelievre, 1995: High resolution climate simulation over Europe, *Clim. Dyn.*, **11**, 321-339

DeWeaver, E., and S. Nigam, 2002: Linearity in ENSO's Atmospheric Response, *J. Climate*, **15**, No. 17, 2446-2461

Eady, E. T., 1949: Long waves and cyclone waves, *Tellus*, **1**, 33-52

Emanuel, K. A., 1991: The theory of hurricanes, *Ann. Rev. Fluid. Mech.*, **23**, 179-196

Ferranti, L., F. Molteni, and T. N. Palmer, 1994: Impact of localized tropical and extratropical SST anomalies in ensembles of seasonal GCM integrations, *Quart. J. Roy. Met. Soc.*, **120**, 1613-1645

Fraedrich, K., 1994: An ENSO impact on Europe?, *Tellus*, **46A**, 541-552

Fraedrich, K., and K. Müller, 1992: Climate Anomalies in Europe Associated With ENSO Extremes, *Int. J. Climatology*, **12**, 25-31

Frank, W. M., and E. A. Ritchie, 2001: Effects of Vertical Wind Shear on the Intensity and Structure of Numerically Simulated Hurricanes, *J. Climate*, **129**, 2249-2269

Gibson, J. P., P. Kallberg, S. Uppala, A. Hernandez, A. Nomura, and E. Serrano, 1997: ECMWF Re-Analysis Project Report Series - 1. ERA-15 Description, Version 2, *ECMWF Technical Report*, ECMWF, Reading, UK

Gill, A. E., 1980: Some simple solutions for heat-induced tropical circulation, *Quart. J. Roy. Met. Soc.*, **106**, 447-462

Goldenberg, S. B., and L. J. Shapiro, 1996: Physical Mechanisms for the Association of El Niño and West African Rainfall with Atlantic Major Hurricane Activity, *J. Climate*, **9**, No. 6, 1169-1187

Graham, N. E., T. P. Barnett, R. Wilde, M. Ponater, and S. Schubert, 1994: On the Roles of Tropical and Midlatitude SSTs in Forcing Interannual to Interdecadal Variability in the Winter Northern Hemisphere Circulation, *J. Climate*, **7**, 1416-1441

Gray, W. M., 1979: Hurricanes: their formation, structure and likely role in the tropical circulation, In: D. B. Shaw (Ed.), *Meteorology over the tropical oceans*, Roy. Met. Soc., 155-218

Gray, W. M., 1984: Atlantic Seasonal Hurricane Frequency, Part I: El Niño and 30 mb Quasi-Biennial Oscillation Influences, *Mon. Wea. Rev.*, **112**, 1649-1668

Greatbatch, R. J., 2000: The North Atlantic Oscillation, *Stochastic Environmental Research and Risk Assessment*, **14**, 213-242

Grötzner, A., M. Latif, and D. Dommenget, 2000: Atmospheric response to sea surface temperature anomalies during El Niño 1997/98 as simulated by ECHAM4, *Quart. J. Roy. Met. Soc.*, **126**, 2175-2198

Hagemann, S., 2002: Validierung des Niederschlags in globalen Klimamodellen, In: K. Stephan, H. Bormann und B. Diekkrüger (Eds.): *5. Workshop zur hydrologischen Modellierung - Möglichkeiten und Grenzen für den Einsatz hydrologischer Modelle in Politik, Wirtschaft und Klimafolgenforschung*, 115-127, University Press, Kassel

Halpert, M. S., and C. F. Ropelewski, 1992: Surface Temperature Patterns Associated with the Southern Oscillation, *J. Climate*, **5**, 577-593

Hamilton, K., 1988: A Detailed Examination of the Extratropical Response to Tropical El Niño/Southern Oscillation Events, *J. Climatol.*, **8**, 67-86

Haurwitz, B., 1940: The motion of atmospheric disturbances on the spherical earth, *J. Marine Res.*, **3**, 254-267

Held, I. M., S. W. Lyons, and S. Nigam, 1989: Transients and the Extratropical Response to El Niño, *J. Atm. Sci.*, **46**, No. 1, 163-174

Hoerling, M. P., J. W. Hurrell, and T. Xu, 2001a: Tropical Origins for Recent North Atlantic Climate Change, *Science*, **292**, 90-92

Hoerling, M. P., A. Kumar, and T. Xu, 2001b: Robustness of the Nonlinear Climate Response to ENSO's Extreme Phases, *J. Climate*, **14**, 1277-1293

Hoskins, B. J., and D. J. Karoly, 1981: The steady linear response of a spherical atmosphere to thermal and orographic forcing, *J. Atm. Sci.*, **38**, No. 6, 1179-1196

Hoskins, B. J., and P. D. Sardeshmukh, 1987: Transient Eddies and the Seasonal Mean Rotational Flow, *J. Atm. Sci.*, **44**, No. 2, 328-338

Hoskins, B. J., and P. J. Valdes, 1990: On the Existence of Storm-Tracks, *J. Atm. Sci.*, **47**, No. 15, 1854-1864

Hoskins, B. J., I. J. James, and G. H. White, 1983: The Shape, Propagation and Mean-Flow Interaction of Large-Scale Weather Systems, *J. Atm. Sci.*, **40**, No. 7, 1595-1612

Hurrell, J. W., 1995: Transient Eddy Forcing of the Rotational Flow during Northern Winter, *J. Atm. Sci.*, **52**, No. 12, 2286-2301

Hurrell, J. W., and H. van Loon, 1997: Decadal variations in climate associated with the North Atlantic Oscillation, *Climatic Change*, **36**, 301-326

Intergovernmental Panel on Climate Change (IPCC), 1992: Climate Change 1992: the supplemetary Report to the IPCC Scientific Assessment. Houghton, J. T., B. A Callendar, and S. K. Varney (Eds.), Cambridge, England, Cambridge University Press

James, I. N., 1994: Introduction to Circulating Atmospheres, Cambridge, England, Cambridge University Press

Jin, F.-F., and B. J. Hoskins, 1995: The Direct Response to Tropical Heating in a Baroclinic Atmosphere, *J. Atm. Sci.*, **52**, No. 3, 307-319

Kalnay, E., M. Kanamitsu, R. Kistler, W. Collins, D. Deaven, L. Gandin, M. Iredell, S. Saha, G. White, J. Woollen, Y. Zhu, A. Leetma, B. Reynolds, M. Chelliah, W. Ebisuzaki, W. Higgins, J. Janowiak, K. C. Mo, C. Ropelewski, J. Wang, R. Jenne, and D. Joseph, 1996: The NCEP/NCAR 40-Year Reanalysis Project, *Bull. Amer. Met. Soc.*, **77**, No. 3, 437-471

Kang, I.-S., K. Jin, K.-M. Lau, J. Shukla, V. Krishnamurthy, S. D. Schubert, D. E. Waliser, W. F. Stern, V. Satyan, A. Kitoh, G. A. Meehl, M. Kanamitsu, V. YA. Galin, Akimasa Sumi, G. Wu, Y. Liu, and J.-K. Kim, 2002: Intercomparison of Atmospheric GCM Simulated Anomalies Associated with the 1997/98 El Niño, *J. Climate*, **15**, 2791-2805

Knippertz, P., U. Ulbrich, and P. Speth, 2000: Changing cyclones and surface wind speeds over the North Atlantic and Europe in a transient GHG experiment, *Clim. Research*, **15**, 109-122

Kumar, A., and M. P. Hoerling, 1997: Interpretation and Implications of the Observed Inter-El Niño Variability, *J. Climate*, **10**, No. 1, 83-91

Kumar, K. K., B. Rajagopalan, and M. A. Cane, 1999: On the Weakening Relationship Between the Indian Monsoon and ENSO, *Science*, **284**, 2156-2159

Lander, M. A., 1994: An Exploratory Analysis of the Relationship between Tropical Storm Formation in the Western North Pacific and ENSO, *Mon. Wea. Rev.*, **122**, No. 4, 636-651

Landsea, C. W., 2000: El Niño-Southern Oscillation and the seasonal predictability of tropical cyclones, In: H. F. Diaz and V. Markgraf (Eds.), *El Niño: Impacts of Multiscale Variability on Natural Ecosystems and Society*, Academic Press, pp. 127-168

Landsea, C. W., and W. M. Gray, 1992: The Strong Association between Western Sahelian Monsoon rainfall and Intense Atlantic Hurricanes, *J. Climate*, **5**, No. 5, 435-453

Latif, M., D. Anderson, T. Barnett, M. Cane, R. Kleeman, A. Leetma, J. O'Brien, A. Rosati, and E. Schneider, 1998: A review of the predictability and prediction of ENSO, *J. Geophys. Research***103**, No. C7, 14,375-14,393

Lau, N.-C., 1979: The Structure and Energetics of Transient Disturbances in the Northern Hemisphere Wintertime Circulation, *J. Atm. Sci.*, **36**, 982-995

Lau, N.-C., and M. J. Nath, 1990: A general circulation model study of the atmospheric response to extratropical SST anomalies observed in 1950-79, *J. Climate*, **3**, 965-989

Lau, N.-C., and M. J. Nath, 1994: A Modeling Study of the Relative Roles of Tropical and Extratropical SST Anomalies in the Variability of the Global Atmosphere-Ocean System, *J. Climate*, **7**, 1184-1207

Manabe, S., J. L. Holloway, and H. M. Stone, 1970: Tropical circulation in a time-integration of a global model of the atmosphere, *J. Atm. Sci.*, **27**, No. 4, 580-613

Mariotti, A., N. Zeng, and K.-M. Lau, 2002: Euro-Mediterranean rainfall and ENSO - a seasonally varying relationship, *Geophys. Res. Lett.*, **29**, No. 12, 10.1029/2001GL01428

Matsuura, T., M. Yumoto, S. Iizuka, and R. Kawamura, 1999: Typhoon and ENSO simulation using a high-resolution coupled GCM, *Geophys. Res. Lett.*, **26**, No. 12, 1755-1758

May, W., 2000: A time-slice experiment with the ECHAM4 A-GCM at high resolution: The simulation of tropical storms for the present-day and of their change for the future climate, *Danish Meteorological Institute, Copenhagen, Scientific Report*, **00-5**, 54 pages

May, W., 2001: Impact of horizontal resolution on the simulation of seasonal climate in the Atlantic/European area for present and future times, *Climate Research*, **16**, 203-223

Merkel, U., and M. Latif, 2002: A High Resolution AGCM Study of the El Niño Impact on the North Atlantic/European Sector, *Geophysical Research Letters*, **29**, No. 9, 10.1029/2001GL013726

Mitchell, J. F. B., and D. J. Karoly, 2001: Detection of climate change and attribution of causes. In: Houghton, J. T., Ding, Y., Griggs, D. J., Noguer, M., van der Linden, P. J., Dai, X., Maskell, K., Johnson, C. A. (Eds.): Climate Change 2001: The scientific basis, Cambridge University Press, Cambridge, pp. 695-738

Neelin, J. D., D. S. Battisti, A. C. Hirst, F.-F. Jin, Y. Wakata, T. Yamagata, and S. E. Zebiak, 1998: ENSO theory, *J. Geophys. Res.*, **103**, 14261-14290

Orlanski, I., and J. Katzfey, 1991: The Life Cycle of a Cyclone Wave in the Southern Hemisphere. Part I: Eddy Energy Budget, *J. Atm. Sci.*, **48**, No. 17, 1972-1998

Palmer, T. N., D. A. Mansfield, 1986: A study of wintertime circulation anomalies during past El Niño events using a high resolution general circulation model. I: Influence of model climatology, *Quart. J. Roy. Met. Soc.*, **112**, 613-638

Palmer, T. N., and Z. Sun, 1985: A modelling and observational study of the relationship between sea surface temperature in the north-west Atlantic and the atmospheric general circulation, *Quart. J. Roy. Met. Soc.*, **111**, 947-975

Plumb, R. A., 1985: On the Three-Dimensional Propagation of Stationary Waves, *J. Atm. Sci.*, **42**, No. 3, 217-229

Pozo-Vázquez, D., M. J. Esteban-Parra, F. S. Rodrigo, and Y. Castro-Díez, 2001: The Association between ENSO and Winter Atmospheric Circulation and Temperature in the North Atlantic Region, *J. Climate*, **14**, 3408-3420

Raible, C., U. Luksch, K. Fraedrich, and R. Voss, 2001: North Atlantic decadal regimes in a coupled GCM simulation, *Clim. Dyn.*, **18**, 321-330

Rasmusson, E. M., and T. H. Carpenter, 1982: Variations in tropical sea surface temperature and surface wind fields associated with the Southern Oscillation/El Niño, *Mon. Wea. Rev.*, **110**, 354-384

Rayner, N. A., D. E. Parker, E. B. Horton, C. K. Folland, L. V. Alexander, D. P. Rowell, E. C. Kent, and A. Kaplan, 2002: Global Analyses of SST, Sea Ice and Night Marine Air Temperature Since the Late Ninteenth Century, *J. Geophys. Res.*, accepted

Reynolds, R. W., and T. M. Smith, 1994: Improved global sea surface temperature analyses using optimal interpolation, *J. Climate*, **7**, 929-948

Rimbu, N., G. Lohmann, T. Felis, and J. Pätzold, 2003: Shift in ENSO Teleconnections Recorded by a Northern Red Sea coral, *J. Climate*, **16**, No. 9, 1414-1422

Roeckner, E., K. Arpe, L. Bengtsson, M. Christoph, M. Claussen, L. Dümenil, M. Esch, M. Giorgetta, U. Schlese, and U. Schulzweida, 1996: The atmospheric general circulation model ECHAM-4: Model description and simulation of present-day climate, *Report No. 218, Available from Max-Planck-Institut für Meteorologie, Hamburg, Germany*, 90 pages

Roeckner, E., L. Bengtsson, J. Feichter, J. Lelieveld, and H. Rodhe, 1998: Transient climate change simulations with a coupled atmosphere-ocean GCM including the tropospheric sulfur cycle, *Report No. 266, Available from Max-Planck-Institut für Meteorologie, Hamburg, Germany*, 48 pages

Sachs, L., 1992: Angewandte Statistik, Heidelberg, Germany, Springer Verlag

Sardeshmukh, P. D., G. P. Compo, and C. Penland, 2000: Changes of Probability Associated with El Niño, *J. Climate*, **13**, No. 24, 4268-4286

Stendel, M., and E. Roeckner, 1998: Impacts of horizontal resolution on simulated climate statistics in ECHAM4, *Report No. 253, Available from Max-Planck-Institut für Meteorologie, Hamburg, Germany*, 57 pages

Straus, D. M., and J. Shukla, 1997: Variations of Midlatitude Transient Dynamics Associated with ENSO, *J. Atm. Sci.*, **54**, No. 7, 777-790

Timmermann, A., J. Oberhuber, A. Bacher, M. Esch, M. Latif, and E. Roeckner, 1999: Increased El Niño frequency in a climate model forced by future greenhouse warming, *Nature*, **398**, 694-697

Trenberth, K. E., 1991: Storm tracks in the Southern Hemisphere, *J. Atm. Sci.*, **48**, 2159-2178

Trenberth, K. E., and J. W. Hurrell, 1994: Decadal atmosphere-ocean variations in the Pacific, *Clim. Dyn.*, **9**, 303-319

Trenberth, K. E., G. W. Branstator, D. Karoly, A. Kumar, N.-C. Lau, and C. F. Ropelewski, 1998: Progress during TOGA in understanding and modelling global teleconnections associated with tropical sea surface temperatures, *J. Geophys. Res.*, **103**, 14291-14324

Tribbia, J. J., 1991: The rudimentary theory of atmospheric teleconnections associated with ENSO, In: Glantz, M. H., Katz, R. W. and N. Nicholls (eds.), *Teleconnections Linking Worldwide Climate Anomalies*, Cambridge, England, Cambridge University Press, 1991, pp. 285-308

van Loon, H., and J. Williams, 1980: The association between latitudinal temperature gradient and eddy transport. Part II: Relationships between sensible heat transport by stationary waves and wind, pressure, and temperature in winter, *Mon. Wea. Rev.*, **108**, 604-614

van Loon, H., and J. C. Rogers, 1981: The Southern Oscillation. Part II: Associations with Changes in the Middle Troposphere in the Northern Winter, *Mon. Wea. Rev.*, **109**, 1163-1168

van Oldenborgh, G. J., G. Burgers, and A. Klein-Tank, 2000: On the El Niño teleconnection to spring precipitation in Europe, *Int. J. Climatol.*, **20**, No. 5, 565-574

Vitart, F., and J. L. Anderson, 2001: Sensitivity of Atlantic Tropical Storm Frequency to ENSO and Interdecadal Variability of SSTs in an Ensemble of AGCM Integrations, *J. Climate*, **14**, 533-545

Voss, R., W. May, and E. Roeckner, 2002: Enhanced resolution modelling study on anthropogenic climate change: Changes in extremes of the hydrological cycle, *Int. J. Climatol.*, **22**, 755-777

Walker, G. T., 1923: Correlation in seasonal variations of weather, VIII: A preliminary study of world weather, *Mem. Indian Meteorol. Dep.*, **24**, No. 4, 75-131

Wallace, J. M., and N.-C. Lau, 1985: On the role of barotropic energy conversions in the general circulation, *Advances in Geophysics*, **28**, Part A, 33-74

Walsh, K., 1997: Objective Detection of Tropical Cyclones in High-Resolution Analyses, *Mon. Wea. Rev.*, **125**, No. 8, 1767-1779

Wehner, M. F., 2000: A method to aid in the determination of the sampling size of AGCM ensemble simulations, *Clim. Dyn.*, **16**, 321-331

Wu, G., and N.-C. Lau, 1992: A GCM Simulation of the Relationship between Tropical-Storm Formation and ENSO, *Mon. Wea. Rev.*, **120**, No. 6, 958-977

Xie, P., and P. A. Arkin, 1997: Global Precipitation: A 17-Year Monthly Analysis Based on Gauge Observations, Satellite Estimates, and Numerical Model Outputs, *Bull. Am. Met. Soc.*, **78**, No. 11, 2539-2558

Yumoto, M., and T. Matsuura, 2001: Interdecadal Variability of Tropical Cyclone Activity in the Western North Pacific, *J. Met. Soc. Japan*, **79**, No. 1, 23-35

Yumoto, M., T. Matsuura, R. Kawamura, and S. Iizuka, 2001: Western North Pacific Tropical Cyclones and ENSO in NIED CGCM, *Report of the National Research Institute for Earth Science and Disaster Prevention*, No. 61, 14 pages

Acronyms

AGCM	Atmospheric General Circulation Model
AOGCM	Atmosphere-Ocean Coupled General Circulation Model
AMIP	Atmosphere Model Intercomparison Project
BCP	Baroclinic production
BTP	Barotropic production
CMAP	CPC Merged Analysis of Precipitation
CAWI	Global Case Study Winter 1997/98 (T06)
CAWI42	Global Case Study Winter 1997/98 (T42)
CPC	Climate Prediction Center
CTRLWI	Control Winter Experiment (T106)
CTRLWI42	Control Winter Experiment (T42)
DJF	December-January-February
ECHAM	Eureopean Center Hamburg Model
ECMWF	European Center for Medium Range Weather Forecasts
ENSO	El Niño/Southern Oscillation
ERA	ECMWF Reanalysis Project
IPCC	International Panel on Climate Change
JJA	June-July-August
GRWI	Global Regression Winter Experiment (T106)
GRWI42	Global Regression Winter Experiment (T42)
MAM	March-April-May
NAO	North Atlantic Oscillation
NCEP	National Center for Environmental Prediction
NTRWI	Negative Tropical Regression Winter Experiment (T106)
PNA	Pacific/North America
SLP	Sea Level Pressure
SOI	Southern Oscillation Index
SON	September-October-November
SST	Sea Surface Temperature
TRWI	Tropical Regression Winter Experiment (T106)
TS	Tropical Storms

Acknowledgements

First of all, I would like to express my gratitude to my supervisor, Prof. Dr. Mojib Latif, for giving me the opportunity to accomplish this Ph.D. at the Max-Planck-Institut für Meteorologie, for his advice, encouragement, and his continuous support. Furthermore, I am very grateful to Prof. Dr. Klaus Fraedrich for examining this dissertation. I would also like to thank Prof. Dr. Wilfried Zahel, Dr. Ute Luksch and Dr. Axel Timmermann for their participation in the examining board.

I wish to thank all my colleagues for the stimulating and pleasant atmosphere at the Max-Planck-Institut für Meteorologie. Especially, I would like to thank the present and former members of Prof. Dr. Mojib Latif's working group for the good collaboration and their critical comments. Furthermore, I am very grateful to Dr. Fei-Fei Jin, Dr. Jim Hurrell, Dr. Erich Roeckner, and Dr. Axel Timmermann for stimulating discussions, their valuable suggestions and scientific advice.

This study has benefitted from many discussions with the present and former colleagues from the Department of Theoretical Meteorology at the University of Hamburg. Especially, I would like to thank Dr. Ute Luksch, Dr. Richard Blender, Simon Blessing, Dr. Frank Lunkeit, Dr. Christian Franzke and Katrin Walter for fruitful discussions and their support.
I also wish to thank Dr. Anselm Grötzner for his helpful suggestions at the beginning of my Ph.D. and Monika Esch and Uli Schlese for their help in setting up the experiments. I greatly appreciate the invaluable technical help by Norbert Noreiks, Uwe Schulzweida and the whole team of the MPI Central IT Services.

I would like to thank all my colleagues who carefully read and contributed to improve an earlier version of this manuscript, especially Dr. Noel Keenlyside, Jürgen Bader, Michael Botzet, and Holger Pohlmann. I also thank Michael Botzet for his advice regarding the tropical storm analysis.

For the quiet and friendly atmosphere in our office, for fruitful scientific discussions and technical advice, I am very grateful to my colleagues Dr. Dietmar Dommenget and Dr. Marko Scholze.

Apologizing that I do not provide a detailed list of names, I would like to thank all my friends and colleagues who encouraged and supported me especially in the final stages of my work.

Last but not least, I thank Renke, my parents and my brother for their never ending patience, encouragement, and support throughout all the highs and lows accompanying (not only) a Ph.D. thesis in meteorology.

MPI-Examensarbeit-Referenz:

Examensarbeit Nr. 1-79 bei Bedarf bitte Anfragen:
MPI für Meteorologie, Abtlg.: PR, Bundesstr. 55, 20146 Hamburg

Examensarbeit Nr. 80 November 2000	**Vertikalmessungen der Aerosolextinktion und des Ozons mit einem UV-Raman-Lidar** Volker Matthias
Examensarbeit Nr. 81 Dezember 2000	**Photochemical Smog in Berlin-Brandenburg: An Investigation with the Atmosphere-Chemistry Model GESIMA** Susanne E. Bauer
Examensarbeit Nr. 82 Juli 2001	**Komponenten des Wasserkreislaufs in Zyklonen aus Satellitendaten – Niederschlagsfallstudien-** Klepp Christian-Philipp
Examensarbeit Nr. 83 Juli 2001	**Aggregate models of climate change: development and applications** Kurt Georg Hooss
Examensarbeit Nr. 84 Februar 2002	**Ein Heterodyn-DIAL System für die simultane Messung von Wasserdampf und Vertikalwind: Aufbau und Erprobung** Stefan Lehmann
Examensarbeit Nr. 85 April 2002	**Der Wasser- und Energiehaushalt der arktischen Atmosphäre** Tido Semmler
Examensarbeit Nr. 86 April 2002	**Auswirkungen der Assimilation von Meereshöhen-Daten auf Analysen und Vorhersagen von El Niño** Sigrid Schöttle
Examensarbeit Nr. 87 Juni 2002	**Atmospheric Processes in a young Biomass Burning Plume - Radiation and Chemistry** Jörg Trentmann
Examensarbeit Nr. 88 August 2002	**Model Studies of the Tropical 30 to 60 Days Oscillation** **S**tefan Liess
Examensarbeit Nr. 89 Dezember 2002	**Influence of Sub-Grid Scale Variability of Clouds on the Solar Radiative Transfer Computations in the ECHAM5 Climate Model** Georg Bäuml
Examensarbeit Nr.90 Mai 2003	**Model studies on the response of the terrestrial carbon cycle to climate change and variability** Marko Scholze
Examensarbeit Nr.91 Juni 2003	**Integrated Assessment of Climate Change Using Structural Dynamic Models** Volker Barth

MPI-Examensarbeit-Referenz:

Examensarbeit Nr. 1-79 bei Bedarf bitte Anfragen:
MPI für Meteorologie, Abtlg.: PR, Bundesstr. 55, 20146 Hamburg

Examensarbeit Nr.92 Juli 2003	**Simulations of Indonesian Rainfall with a Hierarchy of Climate Models** Edvin Aldrian

ISSN 0938 - 5177